Dissertation zur Erlangung des Doktorgrades
der Fakultät für Chemie und Pharmazie
der Ludwig–Maximilians–Universität München

Ultrafast dynamics in single nanostructures investigated by pulse shaping microscopy

von
Richard Ciesielski
aus
Freiberg (Sachsen)
2016

Dissertation zur Erlangung des Doktorgrades
der Fakultät für Chemie und Pharmazie
der Ludwig–Maximilians–Universität München

Ultrafast dynamics in single nanostructures investigated by pulse shaping microscopy

von
Richard Ciesielski
aus
Freiberg (Sachsen)
2016

Erklärung

Diese Dissertation wurde im Sinne von §7 der Promotionsordnung vom 28. November 2011 von Herrn Prof. Dr. Achim Hartschuh betreut.

Eidesstattliche Versicherung

Diese Dissertation wurde eigenständig und ohne unerlaubte Hilfe erarbeitet.

München, den 6. Juni 2016

.....
(Richard Ciesielski)

Dissertation eingereicht am: 10.06.2016
Erstgutachter: Prof. Dr. Achim Hartschuh
Zweitgutachter: Prof. Dr. Markus Lippitz
Mündliche Prüfung am: 14.07.2016

Abstract

Optical microscopy has developed from a mere tool of imaging to a multi-functional system able to image and manipulate the properties of matter. Usually, there is more information available than just scattering, absorption and transmission of a specimen. In particular, the dynamics of excited systems can reveal much about the underlying physical processes. The key technique used throughout this work is optical pulse shaping of femtosecond laser pulses combined with confocal microscopy. First, this thesis reviews several methods of pulse phase measurements and presents recent improvements in the field from our group. On the basis of the achieved accuracy and controllability, studies on single layer graphene, plasmonic particles and single-walled carbon nanotubes are presented.

During the course of this work, a setup was developed and built that is able to provide and control bandwidth limited, 15 fs laser pulses in the focus of a microscope objective. A challenge in combining pulse shaping with microscopy is to compensate for the large amount of phase distortions caused by the optics. For this purpose, the method of "multiphoton intrapulse interference phase scans" (MIIPS) was implemented and improved.

The linear band structure of graphene is the reason for a very strong third order optical nonlinearity, causing a broad and strong spectrum of four-wave mixing. It is shown experimentally that the third-order non-linear susceptibility is spectrally homogeneous and does not come with an intrinsic phase. Its value is determined to be $\chi^{(3)} = 4.3 \times 10^{-6}$ esu at a central photon energy of 1.55 eV. Due to the spectral homogeneity, graphene is shown to be an excellent reference material for phase measurements. Femtosecond excitation of graphene additionally creates a non-equilibrium distribution of electrons and holes in the conduction and valence band respectively. As a consequence, various scattering processes lead to a broadband light emission, the non-linear photoluminescence. An experimental proof of the theoretically predicted regimes of coherent and incoherent non-linear photoluminescence is given. It is further shown that by tailoring the excitation pulses, the charge carrier dynamics and the photoluminescence can be controlled to a certain extent.

The inherent phase response of resonant plasmonic nanostructures influences the temporal shape of ultrashort laser pulses in the nearfield of the nanostructures. The commonly employed method of phase retrieval by the second harmonic generation of the particles themselves is critically reviewed. The model system of gold nanorods is used to identify a possible phase contribution of the second harmonic generation. This is achieved by a systematic comparison of the second harmonic signal with the near-degenerate four-wave mixing signal of the same particles.

It is shown that two-pulse correlation measurements of (5,4) single-walled carbon nanotubes under resonant conditions probe coherent oscillations of phonon wave-packets. Statistical evaluation proves that the nanotubes show an initial expansion of their diameter under impulsive excitation.

Kurzzusammenfassung

Optische Mikroskopie hat sich von einer bloßen Abbildungsmethode hin zu einem multifunktionalen System entwickelt, das in der Lage ist, Materialeigenschaften darzustellen und zu beeinflussen. Im Allgemeinen sind mehr Informationen verfügbar, als Streuung, Absorption und Transmission. Insbesondere kann die Dynamik angeregter Systeme viel über die zugrunde liegenden physikalischen Prozesse verraten. Die Schlüsseltechnologie dieser Arbeit ist optische Pulsformung, kombiniert mit konfokaler Mikroskopie. Zunächst werden verschiedene Methoden zur Phasenbestimmung kurzer Laserpulse beschrieben, sowie neuere Weiterentwicklungen aus unserer Arbeitsgruppe vorgestellt. Basierend auf der so erreichten Genauigkeit und Kontrollierbarkeit werden Untersuchungen an einzelnen Schichten von Graphen, an plasmonischen Nanoteilchen, sowie an einwandigen Kohlenstoffnanoröhren vorgestellt.

Während dieser Arbeit wurde ein Versuchsaufbau entwickelt und aufgebaut, der die Erzeugung und Kontrolle von bandbreitenbegrenzten, 15 fs langen Laserpulsen im Fokus eines Mikroskopobjektivs ermöglicht. Die zentrale Herausforderung bei der Kombination von Pulsformung mit konfokaler Mikroskopie liegt in der Kompensation der großen Phasenstörungen, die durch die optischen Elemente hervorgerufen werden. Zu diesem Zweck wurde ein Verfahren namens MIIPS verwendet und erweitert.

Die lineare Bandstruktur von Graphen erzeugt unter anderem eine sehr starke optische Nichtlinearität dritter Ordnung, die die Ursache für ein breitbandiges und intensives Vierwellenmischspektrum ist. Im Experiment wird gezeigt, dass die nichtlineare Suszeptibilität dritter Ordnung spektral homogen und dispersionslos ist. Bei einer Energie von 1.55 eV wird ihr Wert zu $\chi^{(3)} = 4.3 \times 10^{-6}$ esu bestimmt. Wegen der spektralen Homogenität kann gezeigt werden, dass Graphen eine exzellente Referenzprobe für die Phasenbestimmung ist. Die optische Anregung mit Femtosekundenpulsen erzeugt zusätzlich eine Nichtgleichgewichtsverteilung von Elektronen und Löchern im Leitungs- und Valenzband. In Folge dessen führen zahlreiche Streuprozesse zur breitbandigen, nichtlinearen Photolumineszenz. Es wird ein experimenteller Beweis der Existenz der theoretisch vorhergesagten Regime kohärenter und inkohärenter Photolumineszenz erbracht. Weiterhin wird gezeigt, dass die Ladungsträgerdynamik und die Photolumineszenz in gewissen Grenzen durch eine gezielte Anpassung der anregenden Lichtpulse gesteuert werden können.

Die resonanten, plasmonischen Nanostrukturen immanente Phasenantwort beeinflusst die zeitliche Form ultrakurzer Laserpulse im Nahfeld solcher Nanostrukturen. Die üblicherweise verwendete, auf der Erzeugung der optischen zweiten Harmonischen gründende Methode zur Phasenbestimmung wird kritisch hinterfragt. Anhand des Modellsystems von Goldnanostäbchen werden mögliche Phasenantworten der zweiten Harmonischen untersucht. Dies wird durch den systematischen Vergleich des Signals der zweiten Harmonischen mit dem aus der Vierwellenmischung stammenden Signal erreicht.

Es wird demonstriert, dass kohärente Schwingungen von Phononenwellenpacketen mittels Doppelpulsanregungen an einwandigen (5,4) Kohlenstoffnanoröhren gemessen werden können. In der statistischen Auswertung zeigt sich, dass sich der Durchmesser der Nanoröhren bei impulsiver Anregung zunächst ausdehnt.

Contents

List of Symbols and Abbreviations

All symbols and abbreviations are introduced in the main text at their first use. Double entries of symbols (e.g. "c") become clear from the context they are used in. Bold faced symbols in the text refer to vectorial quantities, for example the electric field: $\boldsymbol{E} = (E_x, E_y, E_z)^T$.

α	scaling parameter, $1/\text{fs}^2$
ε_0	vacuum permittivity, $8.854\cdots \times 10^{-12}\,\text{F/m}$
Γ_1	decay rate, 1/fs
Γ_2	dephasing rate, 1/fs
λ	wavelength, nm
μ	chemical potential, eV
$\rho_k^{e/h}$	charge carrier population (electrons/holes)
$\phi(\omega)$, $\varphi(\omega)$	spectral phase, rad
ϕ', ϕ'', $\phi^{(n)}$	derivatives of the spectral phase with respect to angular frequency
$\chi^{(n)}$	susceptibility of order n
$\sigma^{(3)}_{xxxx}(\omega,\omega,\omega)$ ..	third order conductivity
ω	angular frequency, rad/fs
$\Omega_R^{(0)}$	Rabi frequency, coupling strength, 1/fs
a,b,c	MIIPS parameters
c	speed of light, 300 nm/fs
c	chirp, fs^2
$E(t)$	time domain electric field, V/m
$E(\omega)$	frequency domain electric field, V/m/Hz
$\lvert E_{11}\rangle$	first excited state of a carbon nanotube
$\lvert GS\rangle$	ground state
f	fitness
f_{SWCNT}	oscillator strength of a carbon nanotube
F	force, N
g	number of pixel groups
$\hbar$	Planck's constant, 4.136 eVfs
$I(t)$	time domain intensity, W/m^2
$I(\omega)$	spectral intensity, $\text{W/m}^2/\text{Hz}^2$

n	refractive index
p	microscopic polarization
S	Bloch vector
t	time, fs
T_1	decay time, fs
T_2^*	pure dephasing time, fs
v_t	phase change speed, rad/iteration
V	Fermi velocity of electrons in graphene, 10^6 m/s
1D	one dimensional
2D	two dimensional
AC	auto-correlation
APD	avalanche photodiode
AS	anti Stokes
ATEP	aqueous two-phase extraction
BEM	boundary element method
BBO	beta-barium borate
BK7	borosilicate glass
CEP	carrier envelope phase
CoMoCAT	cobalt molibdenum catalyst
CVD	chemical vapour deposition
bwl	bandwidth limited
DFT	discrete fourier transform
DOC	sodium deoxycholate
$Fe_2(IO_3)_3$	iron(III)-iodate
FROG	frequency resolved optical gating
FTIR	Fourier transform infrared spectroscopy
FTO	fluorine tin oxide
FWHM	full width at half maximum
G-MIIPS	gated multiphoton intrapulse interference phase scan
GA	genetic algorithm
GDD	group delay disperion, fs^2
GVD	group velocity disperion, fs^2/mm
KDP	monopotassium phosphate
$LiNbO_3$	lithium niobate
MIIPS	multiphoton intrapulse interference phase scan
MLG	multilayer graphene
NA	numerical aperture
ND-FWM	near-degenerate four-wave mixing
NIR	near-infrared, $\lambda > 800$ nm
NL	non-linear
NLPL	non-linear photoluminescence
PL	photoluminescence

PLE	photoluminescence excitation spectrum
PMMA	poly(methyl methacrylate)
PRISM	phase resolved interferometric spectral modulation
RBM	radial breathing mode
RWA	rotating wave approximation
SCOP	strongly coupled optical phonon
SDS	sodium dodecylsulfate
SH	second harmonic
SHG	second harmonic generation
SiO_2	silicon dioxide
SLG	single layer graphene
SWCNT	single-walled carbon nanotube
TBP	time-bandwidth product
TEM	transmission electron microscope
THG	third harmonic generation
Ti:Sa	Titanium Sapphire laser
TLS	two-level system
TMOS	tetramethylorthosilicate
TO	third order, fs^3
TOD	third order dispersion, fs^3/mm
TPC	two-pulse correlation
TTM	two temperature model
UV	ultra-violett light, $\lambda < 400\,nm$

Chapter 1

Introduction

Since the early days of microscopy in the 16^{th} and 17^{th} century, when scientists like Galileo Galilei were working on devices capable of magnifying biological species and crystals, much progress has been made. The first challenges were to get glass types with reproducible quality, to manufacture magnifying glasses and to achieve a steady illumination. Once these issues became more tractable, the design and production of better lenses came into focus, because it was realized that spheric and chromatic aberrations severely restrict the scope of microscope applications if not counteracted. In the late 19^{th} century, the first oil immersion objectives were built to extend the numerical aperture beyond 1. At that step, technical progress had brought microscopy to the fundamental physical diffraction limit, which was circumvented in the 1980s by means of optical nearfield microscopy [1, 2].

Optical investigation of nanostructures requires a high spatial resolution on the one hand. On the other hand, a high temporal resolution is often also wanted. This is due to the fact that most physical processes become faster if the size of the device or object is reduced and because quantum effects start to become important with decreasing dimensions. Examples are: coherent dynamics of molecules, plasmonics, charge carrier dynamics in semiconductors or quantum dots which all occur on timescales down to few femtoseconds. The advent of broadband laser systems has hereby provided a valuable tool to enter the femtosecond time regime, which principally cannot be covered by conventional electronic measurement techniques. Optical methods are thus the only way we can presently obtain information on these timescales, however their temporal resolution is restricted to the excitation of a specimen, the signal detection is orders of magnitude slower. The task to provide laser pulses shorter than 150 fs on a nanometer spatial area can nowadays be compared to the situation of microscopy in the early 20^{th} century. Getting to the optical resolution limit is today mainly a question of buying the correct equipment, but was highly nontrivial back then. While femtosecond laser systems, pulse shapers and compressors can be bought from stock, installing and using them is still challenging. There are two main reasons for this; one lying in the difficulty of setup alignment, and the other in the dispersion control. Controlling length and temporal shape of a laser pulse by manipulating the spectral phase can only be accurate, if the phase distortions, present in the system, are known in the first place. There are companies, developing fully integrated systems

for this purpose, but these still cannot provide a usability as good as e.g. commercial fluorescence microscopes have become with respect to spatial resolution. Once these technical difficulties are mastered, the ability to control phase and amplitude of the pulses in a small excitation volume opens up a variety of possible measurements. A method that circumvents the bandwidth limit in a fashion similar to the nearfield techniques breaking the diffraction limit is still completely unknown.

The first programmable spatial light modulators that enabled control over the pulse shape by applying an arbitrary phase profile were realized in the 1990s by Weiner et al. [3], followed by other groups that extended the method to phase and amplitude shaping [4] or made use of these capabilities in pulse compression techniques [5, 6]. In 1999 the Nobel prize in chemistry was awarded to Ahmed H. Zewail for his work in femtochemistry, a field that was expected to largely benefit from femtosecond pulse control. Without any doubt, there have been important experimental improvements in this direction [7, 8, 9], but after more than 15 years of progress the hope of a major breakthrough in femtochemistry based on femtosecond pulse control is somewhat muted. It was realized that one important missing link was spatial control of the samples in order to address single molecules and nanostructures, which first of all can be achieved by microscopy techniques. The challenge of delivering bandwidth limited femtosecond laser pulses in the focus of a microscope objective is mainly a technical issue [10]; however it has also benefited from recent developments in phase characterization techniques [11, 12]. Beyond conventional confocal microscopy, it is possible to combine femtosecond pulse control with super-resolution microscopy, aided by strong nearfield enhancement factors of metal scanning probes [13, 14, 15] or localized antennae [16, 17, 18, 19]. These configurations have been shown to work and to be valuable tools, but they come with the challenge of having to describe the sample-probe interaction in addition to the light-matter interaction of the specimen. Other recent developments go in the direction of femtosecond control of nanoobjects in the context of conventional confocal microscopy, where the samples are typically diluted such that they are individualized inside the focus volume of smaller than $1\,\mu m^3$. Measurements have been performed on individual plasmonic particles [20] or single molecules [21] with a focus on the optical detection of electronic properties and dynamics on femtosecond timescales.

Graphene is a single sheet of the graphite structure, only one layer of carbon atoms thick that has attracted much attention of the community. In 2010, Andre Geim and Konstantin Novoselov were awarded with the Nobel price in physics for their pioneering work on the new material. The structure of graphene consists of sp^2 hybridized carbon hexagons that are arranged in a honeycomb lattice [22, 23]. Therefore, two types of carbon atom configurations exist inside the layer, whose only difference is their spatial orientation. This also reflects in reciprocal space, where two sub-lattices exist. The band structure resulting from the crystal structure shows an interesting feature at the K and K' point; here the energy momentum-relation becomes linear, meeting the Fermi level at the K points. What seems to be a relatively simple system with respect to light-matter interactions at first glance, shows rich photophysics upon closer examination [23, 24, 25, 26, 27, 28, 29], enabling a large number of applications [30, 31, 32, 33]. It has already been shown that the dynamics of excited charge carriers happen on ultrafast timescales, with electron

mobilities far superior to conventional semiconductors [23, 26]. Due to these and other properties, graphene is believed to be a very promising candidate for applications in opto-electronics. Origin and properties of the femtosecond dynamics of the charge carriers are thus of particular interest to the community.

Single-walled carbon nanotubes are thin structures of sp^2 hybridized carbon atoms that can be imagined as rolled up sheets of graphene [34]. Their electronic properties depend on the number of carbon atoms per circumference and the precise orientation of the carbon grid, dividing them into groups of metallic and semiconducting nanotubes [35, 34]. The electronic density of states shows pronounced peaks that are due to van Hove singularities and form the set of main energy levels. The lowest resulting level transition in semiconducting nanotubes, the E_{11} transition, causes the creation of tightly bound exitons upon optical excitation [36]. Singe walled carbon nanotubes are more than an order of magnitude thinner than the state of the art in transistor size of modern, silicon based chip technology. Therefore they are a potential link to the miniaturization of electronics and moreover, could be used for quantum information technology in the future. Very recently, it has been shown that the photoluminescence of semiconducting carbon nanotubes can be used as single photon source even at room temperature [37], which is an essential property for quantum electronics. Our research interest was devoted to the dynamics and controllability of the E_{11} optical resonance of such nanotubes, focussing on the coherent excitation of phonon wave-packets.

Metallic nanoparticles show resonances, tunable by their geometry, in the visible to near-infrared spectral range [38, 39]. Even though their physics can often very accurately be described by multipole expansions, the field of research is ever active and vivid, due to their intriguing properties for nanooptics [40, 41]. Enhancement of optical fields, localization and near-to-farfield conversion of fluorescence signals define a range of properties that makes them interesting for a large amount of optics applications ranging from basic research, over quantum information, scanning probe techniques, and sensing to optical lithography and solar cells. With femtosecond pulse shaping microscopy, it is possible to address the question of the temporal field profile in the nearfields of such structures and investigate the basic physical mechanisms of non-linear processes inside them.

1.1 Outline of the thesis

This thesis is structured in four main chapters, covering the technique of pulse shaping microscopy, the non-linear optical response of graphene, the influence of the spectral phase on non-linear light emission in plasmonic particles, and the RBM phonon dynamics of (5,4) single-walled carbon nanotubes.

Chapter 2 introduces the concept of optical pulse shaping microscopy. The aim is to achieve a high degree of control of the optical fields at the spatial resolution of the system with simultaneous femtosecond temporal resolution, corresponding to the bandwidth limit of the laser. The basics of femtosecond laser pulses are therefore explained with a

special focus on the spectral phase and the possibility to manipulate it by a spatial light modulator (SLM). The second part of the chapter is devoted to the challenge of retrieving the spectral phase of the laser by the help of non-linear optical signals. Since the topic is evolving quickly and is still relatively new, an overview of phase retrieval methods is given, as far as they are used in the remainder of this work. The main method used here is called "Multiphoton intrapulse interference phase scans" (MIIPS), which is based on the detection of the second harmonic spectrum of a reference material while applying a known test phase to the laser. Three variations and improvements of the original protocol are presented which were developed and used in our group in the last years.

Chapter 3 is centered around non-linear optical experiments, performed on exfoliated single layer graphene, which aim at a better understanding of the non-linear optical properties of graphene and possible applications. The third order nonlinearity of graphene, which leads to a broad and strong four-wave mixing signal, is found to be spectrally homogeneous in amplitude and phase, implying that the process is happening instantaneously on the available timescale of 15 fs. This result is then successfully applied to measure the spectral phase of a laser pulse, using four-wave mixing of graphene as a reference process. Apart from the third order nonlinearity, a large number of excited charge carriers is produced upon pulsed excitation of graphene, resulting in the emission of a broadband non-linear photoluminescence spectrum. The dynamics of these charge carriers can be probed and manipulated by using tailored pulse pairs, created by the pulse shaper. A coherent and an incoherent contribution to the non-linear photoluminescence are experimentally identified and a successive change in electronic and phononic temperature are used to model the incoherent part by means of a two-temperature model.

Chapter 4 presents a discussion on spectral phase retrieval of single plasmonic nanoparticles by second harmonic based methods. The resulting phase profiles are compared to similar data, retrieved by near-degenerate four-wave mixing. The observed differences are finally applied to non-linear imaging where they are used as a contrast mechanism.

In chapter 5, a study on the coherent dynamics of phonon wave-packets in (5,4) single-walled carbon nanotubes at room temperature is presented. With an oscillation period of 90 fs, this is happens in a regime where the laser pulses can be seen as impulsive excitation.

Chapter 2

Pulse shaping microscopy: Principles and implementation

The following chapter describes the principles of femtosecond pulse shaping in combination with confocal microscopy. In sect. 2.1, the focus lies on the introduction of basic concepts as far as they are needed for the present work. Emphasis is placed on the manipulation of the spectral phase and amplitude of a laser pulse by a spatial light modulator. Based on this, sect. 2.2 is detailing the setup implementation in use. Sect. 2.3 covers the subject of phase retrieval, using the spatial light modulator and the detection of non-linear light emission by reference samples. Concepts of existing methods are reviewed and the improvements done here are presented. All techniques were implemented and tested at the pulse shaping setup in order to compare them and to derive statements about their accuracy.

2.1 Principles of femtosecond pulse shaping microscopy

2.1.1 Femtosecond laser pulses

Mode-locked lasers have enabled measurements in the femtosecond regime for about 30 years [42]. The first Titanium Sapphire laser, which is nowadays the most commonly used ultrafast laser system, was presented in 1986 [43]. A femtosecond laser pulse is characterized by a broad spectrum $I(\omega) \propto |E(\omega)|^2$ with a stable phase function $\varphi(\omega)$ of the electric field $E(\omega)$. This is achieved by so-called "mode locking", which ensures that the different spectral modes have a constant relative phase for the whole spectrum [38]. That way, the broad spectrum is concentrated in the time domain to short pulses, whose temporal profile in return strongly depends on the phase profile. The shortest, bandwidth limited (bwl), laser pulse is achieved by a completely flat phase profile, which means that the first derivative with respect to the angular frequency ω is spectrally constant:

$$\frac{d\varphi(\omega)}{d\omega} = const. \tag{2.1}$$

This condition leaves two parameters of the phase undetermined. The first is a linear phase function, which is equivalent to a temporal shift by τ: $E(\omega) \cdot e^{i\omega\tau}$, and the second is a constant phase ϕ, which changes the carrier envelope phase (CEP): $E(\omega) \cdot e^{i\phi}$. Already a second-order polynomial phase function (often called "chirp") will stretch a laser pulse in the time domain. The local second-order phase, which is called group delay dispersion (GDD), is defined as:

$$GDD(\omega) = \frac{d^2\varphi(\omega)}{d\omega^2}. \tag{2.2}$$

In most cases, the GDD contains all information about the pulse shape. The only exceptions are pulse shapes, where the phase curvature is locally not defined, for example at sudden phase steps [44], or phase kinks (e.g. for a V-shaped phase profile, see sect. 2.1.3). Even though both cases would rarely occur, they demonstrate that the GDD in the most general case does not contain the full information on the laser pulse. If these special problems can be excluded, knowing the local GDD over the full spectrum is equivalent to knowing the laser pulse in the time domain.

Optical detectors are sensitive to light intensity, but not to electric fields, which means that they never measure the phase of a pulse. The problem of phase measurement is often solved by the usage of non-linear light emission processes, whose efficiency depends on the light intensity in a power law fashion (see sects. 2.3, 3.2). Since the temporal profile of the light intensity depends on the phase, the output of these processes reflects the pulse shape. As the temporal pulse shape is not influenced by the zero and first polynomial order of the spectral phase, it is also impossible to measure them this way, so the carrier envelope phase and the precise arrival time at the sample remain unknown. This fact is the second reason why the GDD is often used to characterize ultrashort pulses instead of the spectral phase.

Time and frequency domain are connected by the Fourier transform, as demonstrated by the example of the electric field amplitude E:

$$\begin{aligned} E(\omega) &= \mathcal{FT}\left[E(t)\right] = \frac{1}{\sqrt{2\pi}} \int_{-\infty}^{\infty} E(t) \cdot e^{i\omega t}\, dt, \\ E(t) &= \mathcal{FT}^{-1}\left[E(\omega)\right] = \frac{1}{\sqrt{2\pi}} \int_{-\infty}^{\infty} E(\omega) \cdot e^{-i\omega t}\, d\omega. \end{aligned} \tag{2.3}$$

This relation allows for a switch between a description in the time domain (TD) and one in the frequency domain (FD) and to calculate quantities as the pulse length Δt, or the pulse width $\Delta\omega$. The spectral shape thereby determines the so called time-bandwidth product (TBP), which is given by:

$$\Delta t \cdot \Delta\omega \geq TBP. \tag{2.4}$$

The equality holds for the bandwidth limited case in which the minimum pulse length Δt is reached by a flat phase profile. The number of the time-bandwidth product depends in

part on the way, the pulse width and pulse length are defined, which is typically done by the full-width-at-half-maximum of the intensity trace. Simple pulses without a complex shape, where temporal and spectral amplitudes are varying smoothly, have the smallest TBP. Fig. 2.1 presents the case of a laser pulse as used in the present experiments (c.f. sect. 2.2) with its calculated time domain signal. A constant GDD of 250 fs^2, such as introduced by a 5 mm thick lens, obviously broadens the pulse in the time domain. The FWHM of the bandwidth limited pulse is 21.8 fs, whereas the chirped pulse has a FWHM of 25.2 fs and the spectral width amounts to 0.21 rad/fs, resulting in a time bandwidth product of: $TBP = 4.58$ rad. Apparently the spectral width in this is case not what one would naively guess (0.26 rad/fs or 100 nm from the steep edges) and also the difference in temporal width of the bandwidth limited and the distorted pulse is smaller than estimated optically from the graph. This discrepancy highlights a difficulty in the usage of these numbers, namely that their relative magnitude depends on the actual pulse shape and is not a universal quantity. For example in case of a Gaussian laser pulse, whose temporal shape looks almost exactly like the present laser pulse (only missing smaller side bands), the time bandwidth product is $TBP = 0.44$ rad, though it is an order of magnitude smaller than the value of the laser pulses used here, which are in fact not much shorter.

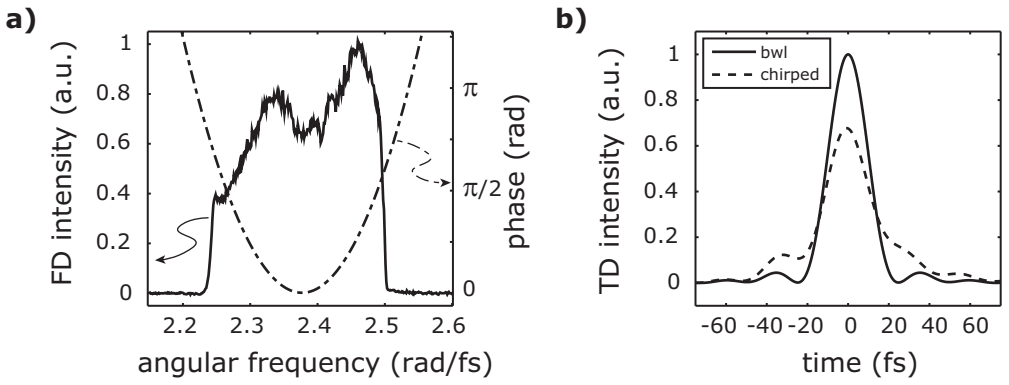

Figure 2.1: (a) Spectrum of the laser and a phase profile of a constant GDD of 250 fs^2. (b) Calculated intensity of the bandwidth limited, flat phase (bold) and chirped laser pulse (dashed) in the time domain.

2.1.2 Optical pulse shapers

The main idea of an optical pulse shaper is to manipulate the spectrum of a coherent, broadband laser pulse in amplitude and phase in order to gain control over the temporal shape [45, 46, 47]. The working principle of a device, based on a liquid crystal light modulator [48][1], is shown in fig. 2.2a. Due to its structure, it is also called a "spatial light modulator". Inside the shaper, the pulse is first split into its spectral components by a

[1]Instead of liquid crystal light modulators, a variety of other devices such as acoustooptic modulators or micro-mirror arrays exist, serving the same purpose [46].

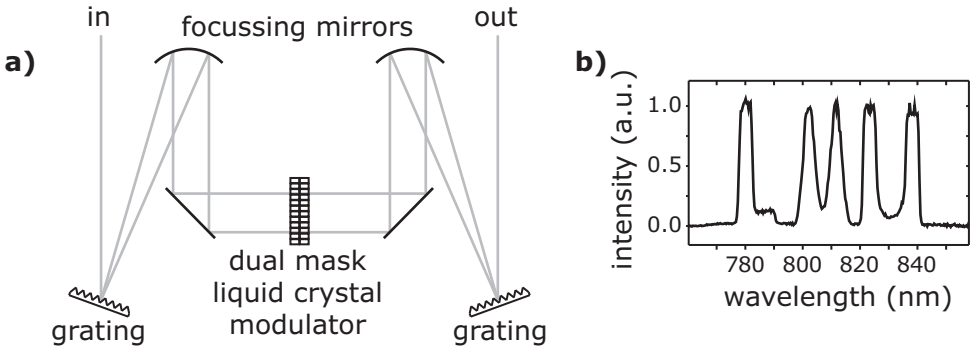

Figure 2.2: (a) Schematic of a pulse shaper based on the 4f layout. The frequency components of the incoming laser pulses are separated in the Fourier plane, where a dual mask liquid crystal modulator is placed, allowing for phase and amplitude manipulation. After this, the beam is reconstructed in an identical beam path. (b) Demonstration of operation by amplitude shaping the letters "LMU" to the laser spectrum.

grating and then focussed by a cylindrical mirror. The liquid crystal light modulator is placed in the Fourier plane, where all spectral components are neatly separated. It consists of an array of liquid crystal cells, which allow for a modification of the refractive index of every spectral component, changing the spectral phase accordingly [48]. The device used throughout this work is a double cell array which also enables an attenuation of the spectral amplitude [3, 49, 48]. Behind the Fourier plane, the pulse is reconstructed by another cylindrical mirror and a grating, making the device a 4f design. Instead of the depicted, stretched design with two focusing mirrors and two gratings, a mirror can be placed behind the liquid crystal device such that the beam is reconstructed in the same beam path as where it was split up (back-folded). Installing a slight vertical angle through the beam path allows for picking up the laser beam later on by a mirror, which is the scheme that was realized in the present setup. With such a spatial light modulator, arbitrary phase and amplitude shapes can be imposed on the laser spectrum. The capability of amplitude shaping is demonstrated in fig. 2.2b, where a special amplitude mask forms the initials of the Ludwig-Maximilians-University "LMU" within the spectrum, visualized by a spectrometer behind the pulse shaper. Phase shaping cannot be demonstrated as easily but it evinces the same flexibility and accuracy as in amplitude shaping.

All pixels of a pulse shaper cover a discrete spectral region, in the present case approximately 1 nm per pixel. The result is that only step-wise phase or amplitude masks can be applied to the shaper. In case of amplitude pulse shaping, this is not a big restriction but for phase shaping it matters, because the pulse shape is mainly determined by the second derivative of the phase, the group delay dispersion. Strictly speaking, the GDD is undefined in such a pixel array because of the stepwise constant phase profile. Unlike the infinite time and frequency domain of the Fourier transform of eq. 2.3, the Fourier

transform now has to be written as a discrete and finite sum:

$$E(t) = \frac{1}{\sqrt{2\pi}} \sum_{k=1}^{N} E(\omega_k) \cdot e^{\varphi_k} \cdot e^{-i\omega_k t} \; \Delta\omega, \tag{2.5}$$

where ω_k are the (mean) frequencies of the N pixels. Assuming an equal spectral spread with $\Delta\omega$ being the width of the pixels, the frequencies are given by:

$$\omega_k = \omega_{min} + (k-1) \cdot \Delta\omega \quad (k \in 1, 2, \ldots, N). \tag{2.6}$$

An implicit assumption that has been made here is that the spectral resolution of the pulse shaper is only determined by the pixel size. A more detailed model would include the finite size of the laser beam on the LCM array which leads to cross-talk between the pixels [50]. The result of the finite sized integrals is that there is no longer a single laser pulse but a train of sub-pulses, repeating with the period of $2\pi/\Delta\omega$, which amounts to about 2 ps for a laser spectrum at 800 nm central wavelength. These sampling replicas of the pulse are usually at least an order of magnitude weaker than the "original" pulse, but in some cases one has to be aware that they exist [50]. The phase φ_k of eq. 2.5 is the phase, applied by the pulse shaper at the frequency of ω_k. In the situation of an applied, stepwise constant phase profile as presented here, the most notable consequence is that the temporal pulse profile is determined by the *discrete* phases φ_k and not by the GDD.

It is, on the other hand, perfectly possible to calculate the correct (stepwise constant) phase profile for the pulse shaper by double integration if the GDD is given:

$$\varphi_k = \left\langle \int_0^{\omega} \int_0^{\omega'} GDD(\omega'') \;\; d\omega'' d\omega' \right\rangle_{\omega_k, \Delta\omega}. \tag{2.7}$$

The brackets $< \cdots >_{\omega_k, \Delta\omega}$ stand for the average value around ω_k in an interval of $\Delta\omega$, thus covering the spectral range of pixel k. Since this is possible, it makes sense to treat the spectral phase and its derivatives in the following as if they resulted from the spectrally and temporally infinite integral of eq. 2.3.

At a frequency spacing of $\Delta\omega$ between the single pixels, there is an ultimate limit of the first-order phase that can effectively be applied to the shaper. The phase profile applied to the liquid crystal modulator is always modulus 2π because there is no difference between a spectral phase of φ and of $(\varphi + 2\pi)$. This also means, that for two neighboring pixels k and $k+1$ a phase difference of π is indistinguishable from $-\pi$ or more generally any phase difference $\Delta\varphi = \varphi_{k+1} - \varphi_k \geq \pi$ from its counterpart $\Delta\tilde{\varphi} = 2\pi - \Delta\varphi$. Therefore, a maximum pixel-to-pixel phase change of $\Delta\varphi < \pi$ has to be guaranteed under all circumstances, setting a limit to the maximum permissible local first derivative of the phase:

$$\varphi'_{max} = \max\left(\frac{\varphi_{k+1} - \varphi_k}{\Delta\omega}\right) < \frac{\pi}{\Delta\omega}. \tag{2.8}$$

This criterion is to be understood as a hard one; it sets the outer limits of validity for eq. 2.7. For example in case of a second-order polynomial phase (chirp) $\phi(\omega) = c/2 \cdot (\omega - \omega_0)^2$, and

in case of 100 illuminated pixels and a laser bandwidth of 100 nm centered at 800 nm, the limit is given by $c_{max} = 6800\,\mathrm{fs}^2$. Larger values of a constant chirp cannot be realized with a pulse shaper of the given specifications.

For practical reasons it is not advisable to make full use of this range at all times because other effects, such as a reduced spectral resolution at the pulse shaper or the spectral dispersion of the device itself will further decrease the usable sector. As another technical note, there is a small inter-pixel region not covered by the liquid crystal cells. Its size amounts to about 2 % of the total pixel size, causing periodic artifacts as known from the discrete pixelation of the phase in the shaper. These artifacts would typically not be visible, because their bandwidth is much smaller than the spectral bandwidth (=pixel size) of the shaper itself.

2.1.3 Phase and amplitude masks for pulse shaping

In the following, phase and amplitude masks are presented that were used in order to achieve special pulse shapes in the time domain throughout this work. A phase mask $\phi(\omega)$ and an amplitude mask $M(\omega)$ are applied to the original spectrum according to the following relation:

$$E(\omega) \overset{\text{pulse shaper}}{\longmapsto} M(\omega) \cdot E(\omega) \cdot e^{i\phi(\omega)}, \tag{2.9}$$

so the above mentioned effects of replica pulses and pulse shaper artifacts are completely ignored here. Mathematical proof for the different cases is straightforward and can be found in the literature [38, 44, 46]. It is important to note that in the experiment, an amplitude mask can only be applied to the *intensity*. Therefore, all parts of an amplitude mask with negative sign need a corresponding phase change of π in the phase mask, for instance in case of the sinusoidal amplitude masks.

Linear phase: A linear phase of:

$$\phi(\omega) = \tau \cdot (\omega - \omega_0) \tag{2.10}$$

translates the laser pulse by the time τ without changing its temporal shape.

Polynomial phase: A polynomial phase of:

$$\phi(\omega) = \sum_{n=2}^{m} a_n \cdot (\omega - \omega_0)^n / n! \tag{2.11}$$

stretches a bandwidth limited laser pulse in time. Here the carrier frequency of the pulse in the time domain is no longer constant but changes with time, which is called "chirp". In case of a completely unknown phase profile, a scan over the orders $n = 2$ and $n = 3$ can give a rough pulse correction phase (c.f. sect. 2.3.2). A phase with $n = 2$ is called *linear*

chirp, while a phase with $n = 3$ is called *quadratic* chirp, because in the time domain, the carrier frequency changes with time either as a linear or as a quadratic function.

Sinusoidal phase: A sinusoidal phase of:

$$\phi(\omega) = a \cdot \cos(b \cdot (\omega - \omega_0) - c) \tag{2.12}$$

creates pulse trains [44], spaced by the time b. The phase amplitude a determines the size of the subsequent pulses, which are weighted by the Bessel function of first kind: $E_n \propto J_n(a) \cdot e^{in\pi/2}$. This phase mask is most often used for MIIPS (see sect. 2.3.3).

V-shape phase: The spectrum is divided into two parts with different linear phase profiles:

$$\phi(\omega) = \begin{cases} -\tau_1 \cdot (\omega - \omega_0) & \omega < \omega_c, \\ \tau_2 \cdot (\omega - \omega_0) & \omega \geq \omega_c. \end{cases} \tag{2.13}$$

The result is, that the spectral parts $\omega < \omega_c$ get delayed by $-\tau_1$ and the spectral parts $\omega \geq \omega_c$ get delayed by τ_2, resulting in two different laser pulses with different central frequencies, that have a relative delay of $\tau_2 + \tau_1$ to each other.

Sinusoidal amplitude: A sinusoidal amplitude mask of:

$$M(\omega) = \cos(\tau/2 \cdot \omega) \tag{2.14}$$

subdivides the laser pulse into two identical copies, delayed by the time τ. There is no additional phase shift between the two copies of the pulse, which means that scanning τ will result in an interferometric autocorrelation scan with the characteristic interference fringe pattern.

Two-pulse correlation: A sinusoidal amplitude mask of:

$$M(\omega) = \cos(\tau/2 \cdot (\omega - \omega_0) - \Delta\varphi_{CEP}/2) \tag{2.15}$$

subdivides the pulse into two identical copies, delayed by the time τ but with a shared carrier envelope phase (CEP). This is achieved by centering the amplitude mask around the central laser frequency ω_0, see also sect. B.3 in the appendix. Additionally, a CEP difference $\Delta\varphi_{CEP}$ can be set. Scanning the delay τ results in an intensity autocorrelation scan, where the two pulses have a CEP difference of $\Delta\varphi_{CEP}$. This is the amplitude mask, used in chpt. 5 and sect. 3.3.3.

2.1.4 Focussed broadband laser pulses

All pulse compression methods presented in the following sections would typically disregard the actual spatial shape of a laser pulse. The electro-magnetic light fields are studied in a point-like fashion as it might be valid for the wave front of a plane wave, interacting with a small, sub-wavelength sized sample. The validity of this commonly shared prerequisite is discussed in the following example of a focussed laser beam, whose field distribution differs widely from a plane wave.

First of all, focusing a broadband laser pulse in a microscope requires a chromatically corrected objective lens. The lens used here is a "Nikon CFI S-Fluor 100x" oil immersion objective with a numerical aperture of NA = 1.3. The focussing quality of the system in the near-infrared spectral range was tested by comparing the reflected images of the laser at the glass-air interface of a coverslide in slight defocus for different wavelengths, which were selected by setting bandpass filters with the amplitude shaping functionality of the pulse shaper (see fig. 2.3). Comparison to a theoretical image (see appendix B.2

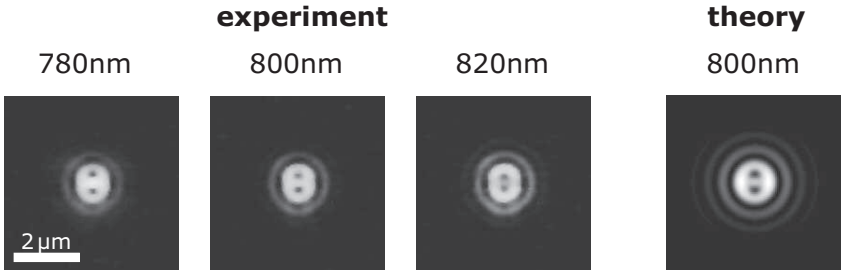

Figure 2.3: Images of the laser beam, reflected at a glass coverslide in slight defocus for three different excitation wavelengths in the near-infrared, compared to a theory image at 800 nm.

and 51) shows only minor deviations in the intensity distribution that can be explained by different transmittivities for parallel and perpendicular polarized light at the beam splitter inside the microscope, which have not been included in the calculation. Importantly, only the size of the reflection pattern slightly changes with wavelength, as was expected from theory [51]. Apart from that, all images are strictly symmetrical in x and y direction for all wavelengths. It is therefore concluded that the focussing properties of the system meet the requirements of a homogeneous pulse without spatial chirp or other distortions.

For a theoretical description of focussed laser fields, the analytical expressions given in chpt. 3.6 of 52 are used, which are based on spherical waves and not on the paraxial approximation of Gaussian beams (see sect. B.1 in the appendix for the formulas). Fig. 2.4a shows the x-component of the electric field at 800 nm wavelength in the focus of a NA 1.3 objective with a refractive index of $n = 1.518$ and a filling factor of 1, where for the sake of simplicity, only the situation without interfaces is considered. Fig. 2.4b gives the intensity in the same spatial region in a logarithmic plot and spectrally integrated over the actual laser spectrum (c.f. fig. 2.6b). The calculated focus region has a lateral size of about 320 nm (FWHM) and extends about 1570 nm on the optical axis. The fields in this region are very

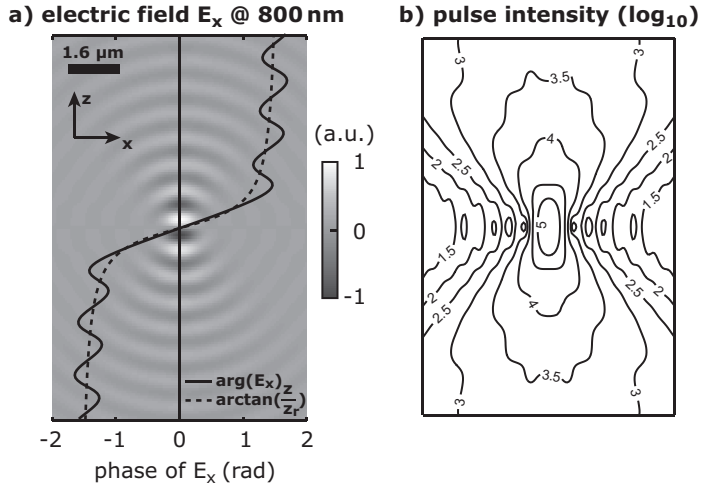

Figure 2.4: (a) Real part of the electric field's x component of a strongly focussed laser beam. Overlaid is its phase through the center of the image (solid line), which is compared to the Gouy phase, based on a Gaussian beam (dashed line). (b) Spectrally integrated intensity profile for the same focus, based on the laser spectrum (log-10 scale).

homogeneous and directly in the center, all components except the x-component vanish (not shown). In the center of the focus, a beam undergoes a phase shift, caused by the reversal of the image at the center of inversion, referred to as the Gouy phase shift [53]. As can be seen in fig 2.4a, the electric field does experience such a phase shift of π in the center. Further away from the center, the phase oscillates as a consequence of the description by spherical waves, first shown by Linfoot in 1956 [54]. The known Gouy phase anomaly, based on Gaussian beams, on the other hand does not show these oscillations and can be calculated as follows [52]:

$$\phi_{Gouy} = \arctan\left(\frac{z}{z_r}\right), \tag{2.16}$$

where z is the coordinate along the optical axis and z_r is the Rayleigh length of the focus. This formula is only valid in the paraxial approximation of Gaussian laser beams, but the comparison with the strict calculation shows, that it can still serve as an average phase in case of a strongly focussed beam and even coincides with it in the center of the focus (see solid and dashed lines in fig. 2.4a). The Rayleigh length itself is a function of wavelength and therefore the Gouy phase in the focus is a function of wavelength, too. For a Gaussian beam it reads:

$$z_r = \frac{\pi w_0^2}{\lambda}, \tag{2.17}$$

with w_0 representing the beam diameter in the focus, whose size is limited by the wave-

length used[2]: $w_0 = \lambda \cdot \xi$. In the focus, the Gouy phase becomes:

$$\phi_{Gouy}(\omega) \approx \frac{z}{z_r} = \frac{z \cdot n \cdot \omega}{2\pi^2 c \cdot \xi^2} \propto \omega. \tag{2.18}$$

Since it is a linear function of the angular frequency inside the focus, it does not influence the pulse shape, a result that has also been verified experimentally [55].

Another aspect of strongly focussed femtosecond laser pulses was highlighted by Pawłowska et al. [10], namely that the amount of glass passed by a laser beam depends on the optical path inside the objective. Therefore, the spectral phase distortions collected can vary, depending on the focus position. The differences in an area of the size of the focus are comparably small, about 1 fs change of the arrival time of the pulse in their case.

To summarize these points, first a very high quality of the focus is achieved for the pulsed laser, as demonstrated by the focus reflection and the comparison with the theoretical expectation. Second, the resulting fields are concentrated in a small volume where the laser is mainly x-polarized and the electric field and phase are spatially and spectrally homogeneous. In this situation, it is justified to talk about a well defined spatial and temporal pulse profile. When referred to the temporal profile of a laser pulse in the following chapters, what is meant is the temporal shape inside the "pointlike" excitation volume of the focus. Whenever objects or changes smaller than around 400 nm are investigated, this has to be considered because the theoretical description possibly has to move to a nonlocal scheme.

2.2 Implementation of the experimental setup

The setup used for most measurements throughout this work consists of an excitation unit, preparing the femtosecond laser pulses, a microscopy unit, and a detection unit. A schematic is presented in fig. 2.5 and will in the following be explained in detail by following the beam path from the laser output to the detector unit.

The laser source is a commercial Titanium Sapphire (Ti:Sa) pulsed laser named "Venteon pulse:one" by the company "Venteon femtosecond laser technologies" (now "Laser Quantum"). It has an output power of about 420 mW, a repetition rate of 80 MHz, and its spectrum, shown in fig. 2.6, covers the range of 650 nm to 950 nm. Shortly behind the laser output, a spatial filter is installed to produce a clean, Gaussian beam shape. The spatial filter consists of an achromatic lens pair and a pinhole, mounted on an x-y positioning post. The collimation of the laser beam is controlled via the position of the second lens along the optical axis. Behind the spatial filter, the spectrum is cut by a longpass 750 nm and a shortpass 850 nm which restricts the spectrum to a bandwidth of 100 nm in total, also increasing the bandwidth limit of the pulse from 5.7 fs to about 15 fs. In the remainder of this work, sometimes a pulse length of 20 fs is given. This is due to the fact that for some experimental configurations, the laser spectrum was further cut or changed in the optical beam path. The full laser bandwidth cannot be compressed in the focus of

[2]If the beam is perfectly focussed, the Abbe limit determines the beam size: $w_0 = 0.61 \cdot \lambda / NA$.

the microscope due to technical restrictions[3]. A prism compressor adds a large amount of negative GDD to the pulse in the following, providing a rough compensation of the large amount of GDD introduced by the optical elements in the beam path. The device is based on a special design, using a single prism only, which experiences four beam passes [56], while the operating principle is the same as for conventional prism compressors. Inside the prism compressor, smaller beam distortions are unavoidable, so a second spatial filter is installed behind it to recreate the Gaussian beam profile. The beam then enters the central unit of the setup: the pulse shaper, whose working principle is described in sect. 2.1.2. The liquid crystal modulator in use is a product of "Cambridge Research & Instrumentation, Inc. (CRi)" (now produced by "Meadowlark Optics, Inc."). It features a double mask scheme, enabling phase and amplitude pulse shaping at the same time. There are 128 pixels with a pitch of 100 µm, spaced by 2 µm. The phase resolution of the device is given by $\Delta\phi \approx 0.01\,\mathrm{rad}$, depending slightly on the used wavelength. The laser polarization is fixed by a broadband polarizer in front of the device. After a third spatial filter, the laser is lead into a confocal microscope, which is equipped with an x-y piezo-scanning stage and an NA 1.3 oil immersion objective. In the focus of the objective the beam has a power of about 0.75 mW which leads to an approximated pulse energy of about 10 pJ. The samples are placed on 150 µm thick coverslides of BK7 glass. A broadband beam splitter leads the signal to the detection unit, consisting of optical filters, an avalanche photodiode (APD) and a spectrometer. For the detection of second harmonic light, there is a second beam path installed, whose lenses are made of fused silica exclusively, which in contrast to BK7 or SF10 is transparent even below 400 nm. The pulse shaper, the scanning stage and the detectors are all controlled by the same computer. Since the software for pulse shaper and signal detection was self-written during this work, it allows for flexible measurement schemes, as will be shown in the next sections.

In all optical units that are passed before entering the microscope, it is essential to control the spatial mode of the laser pulse. The mode can be seen as a superposition of Gaussian laser modes of different wavelengths and they all have to overlap as good as possible. A spatial misalignment of the spectral components is called "spatial chirp" and can originate from the prism compressor or the pulse shaper. By help of the three spatial filters, the laser mode is preserved through the entire beam line.

[3]The resulting phase of the laser in the focus is mainly a third-order polynomial function (see sect. 2.3). The phase, applied to the pulse shaper, gets "wrapped" at multiples of 2π, which, as a consequence of the third-order polynomial, happens more often at the sides of the spectrum than in the middle. A larger bandwidth therefore requires either a larger number of shaper pixels for higher resolution or an additional pre-compression unit, reducing the third order phase distortions.

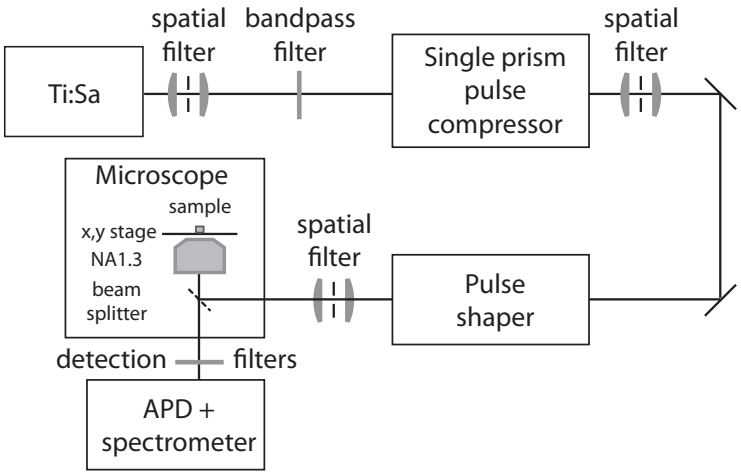

Figure 2.5: Schematic of the femtosecond pulse shaping setup. For details, see main text.

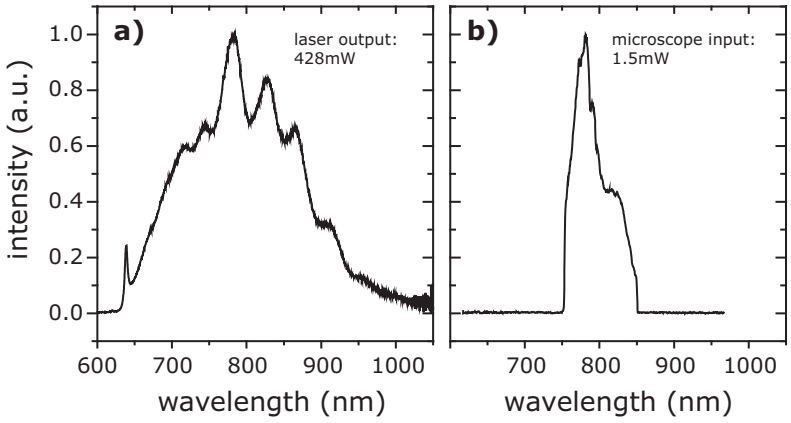

Figure 2.6: Spectrum of the "Venteon pulse:one" Ti:Sa laser at the output (a) and in front of the microscope (b).

2.3 Measurement of phase profiles with high accuracy using an optical pulse shaper

On their way through optical elements and even air, femtosecond laser pulses experience substantial phase distortions. The velocity of light is different for every wavelength with a general trend towards lower velocity for longer wavelengths, called normal dispersion. Therefore after passing a dispersive element, the high energy parts of the pulse will arrive prior to the low energy parts, resulting in a stretched temporal profile. In the optical regime and for typical types of glass, the most important phase distortions can be classified in terms of their second and third polynomial orders, summarized in tab. 2.1 for a number of common materials. A high numerical aperture objective consists of several centimeters of

Material	n	GVD (fs^2/mm)	TOD (fs^3/mm)
Air	1.0003	0.0212	0.0087
BK7	1.511	44.65	32.10
SF10	1.711	156.52	102.52
Fused Silica	1.453	36.16	27.47
LakL21	1.633	61.40	41.42

Table 2.1: Refractive index n, group velocity dispersion (GVD), and third order dispersion (TOD) for optical glasses at a wavelength of 800 nm. [57]

glass. The actual types, lengths and shapes of the lenses inside are not known, so let us assume an objective lens, consisting of 3 cm of BK7 glass as well as of 3 cm of SF10 glass. At a wavelength of 800 nm, the GDD according to tab. 2.1 would then amount to about 6000 fs^2, implying that the temporal width of a Gaussian pulse with a FWHM of 20 fs gets stretched to about 830 fs. As the pulse length increases, the peak intensity decreases to 2.4 % of its original value.

There are three main problems, related to unintentionally stretched pulses. First, the temporal resolution is obviously lost, and furthermore the exact temporal shape remains unknown. Second, non-linear processes will be orders of magnitude weaker than for the shortest pulse. And third, for the case of pulse shapers, if the temporal shape in the focus is unknown, it does not make sense to put a phase to the laser pulse, because it would add up with the unknown, setup related phase. In this case, no experiment can be carried out, because the actual effect of the imposed phase is unclear.

Coarse pulse compression can be achieved using prism compressors, grating compressors, combined prism-grating compressors [56, 58], or negatively chirped dielectric mirrors [59]. These devices add a defined amount of negative GDD and TO to the spectrum, which will eventually compensate with the phase distortions introduced by the setup and create a recompressed laser pulse. Prism and grating compressors can in principle be scaled up in order to account for larger quantities of glass, such as lenses, filters or even optical fibers. They are also flexible with respect to the amount of negative GDD added since one can tune it with the position and angle of the prisms or gratings. Negatively chirped

mirrors can compensate 175 fs^2 per reflection at 800 nm [60] which requires dozens of reflections in case of heavy phase distortions. Bandwidth limited laser pulses can often not be reached with these methods because of higher order phase distortions. For fine-tuning of the spectral phase, optical pulse shapers are used which provide freedom to add arbitrary phase profiles in order to reach the bandwidth limit. A key element is the precise measurement of the phase distortions present in the setup. The remainder of this chapter reviews methods to retrieve the spectral phase of a laser pulse in the presence of phase distortions as they occur inside the focus of high NA microscope objectives by the use of second harmonic (SH) light emission from nanocrystals. The final goal is to have bandwidth limited laser pulses in the focus which can be further modulated by the pulse shaper.

The methods in use can be separated into two types; those which try to maximize the total SH signal recorded by a photodetector (sect. 2.3.2) and those which make use of the spectral shape of the SH to find the phase in a deterministic way (sect. 2.3.3 and 2.3.4). These techniques have the potential to measure the spectral phase of nanoparticles too as long as they provide a non-linear feedback signal. Data interpretation will be more difficult in this case (c.f. chpt. 4).

All methods reviewed in the following sections were implemented to the setup in the course of this work and all the data presented was recorded at the setup in order to compare the different methods of phase retrieval. The benchmark used here is a comparison to the GDD or phase profile, measured by "Multiphoton intrapulse interference phase scans" (MIIPS), described in sect. 2.3.3. Apart from the reviewed methods of phase retrieval, a number of other popular algorithms exists. For completeness, two important methods are listed: "Frequency Resolved Optical Gating" (FROG) [61] and "Spectral Phase Interferometry for Direct Electric-Field Reconstruction" (SPIDER) [62].

2.3.1 Instantaneous non-linear processes

Measurements of the light intensity are generally insensitive to the spectral phase since the intensity is the absolute square of the field. Non-linear light emission processes on the other hand, depend on the temporal shape of the excitation light field, and can therefore be used to gain information about the spectral phase [38]. The shortest possible laser pulse will create the highest signal, because the probability of multiple photons, arriving at the sample at the same time, is maximized. In the case of microscopy, the signal is created only in the small volume of the focus of the microscope objective, so phase matching conditions as in the bulk do not play a role. The notion that the shortest pulse implies the highest non-linear signal has an important underlying assumption: the non-linear process is required to be instantaneous, because any temporal delay of the response would lead to an additional spectral phase [63]. If there is a spectral phase associated to the non-linear process, the maximum signal is not given by the flat-phase pulse anymore. This holds for the linear susceptibility which mediates the local field at the sample, as well as for the non-linear susceptibility which is responsible for the non-linear light emission. Furthermore we require a homogeneous spectral response that shall not highlight or suppress any part of the spectrum.

Second harmonic generation (SHG) is the most commonly used non-linear process for phase measurements in optics. In a crystal, the microscopic condition for generating second harmonic light is that the optically active parts are not centrosymmetric [63]. That way, an anharmonic oscillator is formed which has contributions of odd orders, such as the second harmonic which connects two input fields to a single output field. The potential of centrosymmetric materials on the other hand possesses contributions of even orders, allowing for instance for third-order processes with a total of four fields involved. Beta-barium borate (BBO), mono-potassium phosphate (KDP), or iron(III)-iodate ($Fe_2(IO_3)_3$) are typical non-centrosymmetric materials, used in the laboratory for SHG. For practical reasons, $Fe_2(IO_3)_3$ nanocrystals were used in all cases presented here. They showed a higher SH yield than KDP samples and were much less hydrophobic than BBO samples.

Third order processes are rarely used for pulse characterization in ultrafast optics, yet there are a few examples where third harmonic generation of glass surfaces [64], or gold and $LiNbO_3$ bulk samples was used [65]. In chapter 3.2 graphene's near-degenerate four-wave mixing signal is presented as a promising candidate for pulse characterization, based on a third order optical process.

2.3.2 Algorithms based on the total emitted non-linear intensity

The task of compressing a laser pulse can be approached by solving the problem of maximizing the total and instantaneous non-linear signal of a reference sample. In such a case, the incoming laser intensity is $I_{in}(t)$, and the integrated non-linear signal is given by [63]:

$$I_{NL}^{total} \propto \int I_{in}(t)^n \, dt, \tag{2.19}$$

with $n > 1$ being the nonlinearity coefficient. The signal itself can be detected by an appropriate photodetector without substantial dispersion over the used spectral range. Using an optical pulse shaper, the mathematical maximization problem is to find the phase profile $\phi(\omega)$, that produces the highest possible signal I_{NL}^{total} at the detector when applied to the incoming spectrum[4]:

$$\max_{\phi(\omega)} \left(\int I_{in}(t)^n \, dt \right). \tag{2.20}$$

Possible pulse shaper artifacts and the spectral resolution set a technical limit to the accuracy that can here be achieved (c.f. sect. 2.1.2). As a side note, it is often the case that the central spectral regions of the laser pulse cause the major part of the total non-linear signal compared to the weaker parts at the sides of the laser pulse. This means that the retrieved phase of these spectral parts is less accurate than the phase around the central frequency due to a smaller signal-to-noise ratio.

[4]The time dependent incoming intensity $I_{in}(t)$ calculates from the Fourier transform of the incoming spectrum according to: $E_{in}(t) = \mathcal{FT}[E_{in}(w)]$ with $E_{in}(\omega) = E_0(\omega) \cdot \exp(i\phi(\omega))$ and $I_{in}(t) \propto |E_{in}(t)|^2$.

Polynomial phase scans

The spectral phase is usually a smooth function, which implies that it can be expanded into a polynomial series with a certain degree of accuracy. The first polynomial order and the offset (zeroth-order) do not play a role for the pulse shape and therefore do not influence the non-linear feedback signal. Using a pulse shaper, it is feasible to scan the linear and quadratic chirp, resulting in a 2D map which typically has one pronounced maximum. Fig. 2.7 shows a map of the second harmonic intensity versus second and third

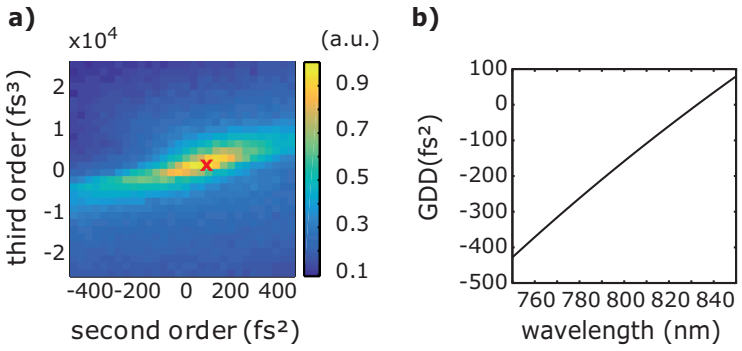

Figure 2.7: (a) 2D chirp scan of the total emitted SH intensity. The red "x" marks the maximum, indicating the polynomial phase of the laser pulse (93.5 fs^2, 1717 fs^3). (b) GDD, retrieved by the 2D chirp scan.

order polynomial phase of a slightly distorted laser pulse. The phase correction can be directly taken from the maximum of the graph, corresponding to the negative of the pulses phase distortion. If the laser spectrum is not too broad (e.g. $\lesssim$ 50 nm in the case of a Ti:Sa laser), the method is able to recover most of the phase distortions from optical glasses, because they are mainly of second and third order.

Genetic algorithms (GA)

Genetic algorithms are a subset of evolutionary algorithms, first proposed by Alan Turing in 1950 [66], that can be used to solve non-linear optimization problems. A main characteristic is that they work without derivatives, and can therefore also be applied to noisy data. In ultrafast optics, evolutionary algorithms for phase retrieval using programmable pulse shapers have been used for almost twenty years [5, 67]. They use the second harmonic generation of a test sample as feedback signal which has to be maximized, but in general the method is not limited to it[5].

For pulse shaping purposes, the algorithm is implemented as follows: the pulse shaper has a finite resolution ($N = 128$ pixels for the used device), which means that the phase optimization problem has N free parameters. These phases ϕ_n can possess values in between $\phi_n \geq 0$ and $\phi_n \leq 2\pi$. The algorithm starts by creating a random set of "genomes" ϕ_n. For

[5]See sect. 3.2 for an example of application of a third order process based genetic algorithm.

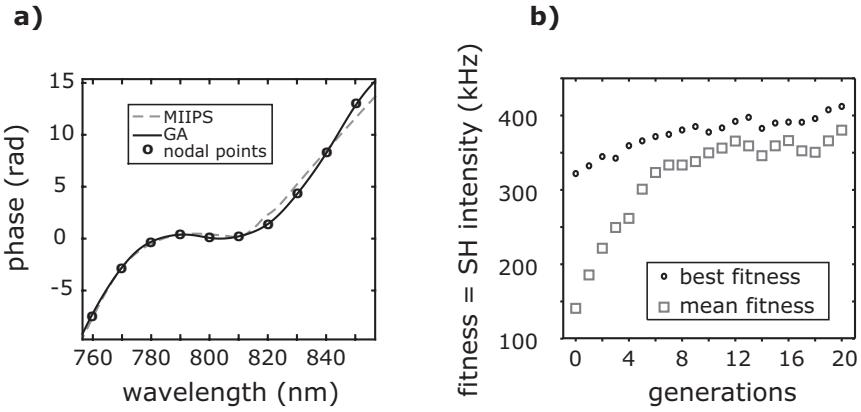

Figure 2.8: (a) Result of a phase retrieval, using the second harmonic based genetic algorithm in comparison to the result from converged MIIPS iterations (see sect. 2.3.3). (b) The convergence plot of the method over 20 generations á 25 genomes and a total of 500 single measurements.

every genome, a fitness $f(\phi_n)$ is determined, which is the non-linear signal intensity from the measurement. Next, the part of the set of genomes with the lowest fitness is sorted out and the remaining free spots are filled with individuals of a new generation (children) which are created out of crossings of old genomes (parents) and random parts (mutations). This is the part which mimics the genome evolution and is responsible for the name of the algorithm. The children get a fitness value by measuring their non-linear signal intensity and the process starts again by disposing the individuals with the lowest fitness.

Genetic algorithms are generally easy to use but difficult to understand in detail, as their behavior is probabilistic. Depending on the starting population and the settings for mutations and crossing of genomes, the number of iterations to reach a maximum can be subject of strong variations. For more complex problems, there is no benchmark of the algorithm telling, if the final solution is the best solution. The main parameters of the current implementation are: the available phase space ϕ_n, the crossover ratio of parents, and the number of generations. In the present case, the phase space is reduced to a finite number of nodal points over the spectrum, typically 9, where the missing in-between values for the shaper are generated by cubic interpolation. The idea behind this is that very sharp phase features are not very likely to occur, but the limitation to fewer free parameters greatly reduces the measurement time. Moreover, not the phase but the GDD on the nodal points is modified, since the first and zeroth-order phase do not contribute to the temporal shape of the laser pulse. There are two advantages in this approach with respect to a version where the phase is directly varied. First, the resulting phase profile is relatively smooth and second, the GDD, which is the real measurement quantity, is directly accessible.

Fig. 2.8 presents an example of a successfully converged genetic algorithm based phase characterization. The deviations from the reference method, multiphoton intrapulse interference phase scan (MIIPS, see sect. 2.3.3), are small.

Phase Resolved Interferometric Spectral Modulation (PRISM)

"Phase resolved interferometric spectral modulation" (PRISM) [68] is a deterministic method to measure the phase profile by a non-linear feedback signal. The main idea is that the phase ϕ_n^t of each shaper pixel n is varied over many single measurements t with a characteristic speed v_n. The trace that is recorded this way looks erratic at first glance, but the signal of an individual pixel can be demodulated by Fourier transform. From the phase of the demodulated signal, the phase of the corresponding pixel for an optimized non-linear signal can be deduced. Since Wu et al. [68] did not present a very detailed description of the method in their original publication, the results of the implementation and application of PRISM, obtained in the course of this work, are presented in the following. Investigations about the accuracy of PRISM with respect to noise represent new findings. Chpt. 4 presents a study on the application of PRISM on plasmonic nanoparticles, using different non-linear feedback signals.

The method, as it was implemented here, works as follows: the pulse shaper's N pixels are divided into g groups of equal size, where the composition of the groups does not play a role. The number of contained pixels is N/g, which has to be a natural number. Now one starts with the first subset of pixels, whose N/g pixels are assigned to a phase progression rate v_n such that the phase at every pixel n and point in time t is given by:

$$v_n = \frac{\pi}{2} + \frac{ng}{N} \cdot \frac{\pi}{2} \qquad n = 0, 1, \ldots (N/g - 1), \tag{2.21}$$

$$\phi_n^t = v_n \cdot t \qquad t = 0, 1, ...(N-1), \tag{2.22}$$

at a total of N time steps. This choice ensures that the phase of every pixel returns to its original value at the end of the cycle: $\phi_n^N = \phi_n^0$. The non-linear signal intensities I_t of every time step t are recorded with the corresponding pixel phase profiles ϕ_n^t applied to the shaper, while the phase of those pixels which are not part of the first subset, remains unchanged. After this, a discrete Fourier transform (DFT) of I_t is performed:

$$\tilde{I}_n = \sum_{t=0}^{N-1} e^{iv_n t} \cdot I_t. \tag{2.23}$$

It is possible to show that the demanded correction phase of pixel n is given by the argument of the complex, Fourier transformed signal:

$$\varphi_n = \arg(\tilde{I}_n). \tag{2.24}$$

The special choice of v_n requires $g \mod 4 = 0$, because the arguments of the exponential function in eq. 2.23 would otherwise be repetitive within one measurement cycle. Once the correction phase for the first group of pixels is done, the procedure is repeated with the other subsets of pixels, yielding a phase profile for the full spectral range of the pulse shaper. Knowledge of which wavelength passes through which pixel is not required here but completes the overall picture as it makes available the full phase information.

Due to various reasons, PRISM should be iterated up to 3 times in order to achieve sufficiently accurate phase reconstruction [68]. Fig. 2.9 demonstrates the application of the algorithm at the example of a 32 pixel pulse shaper[6]. The result compares very well to

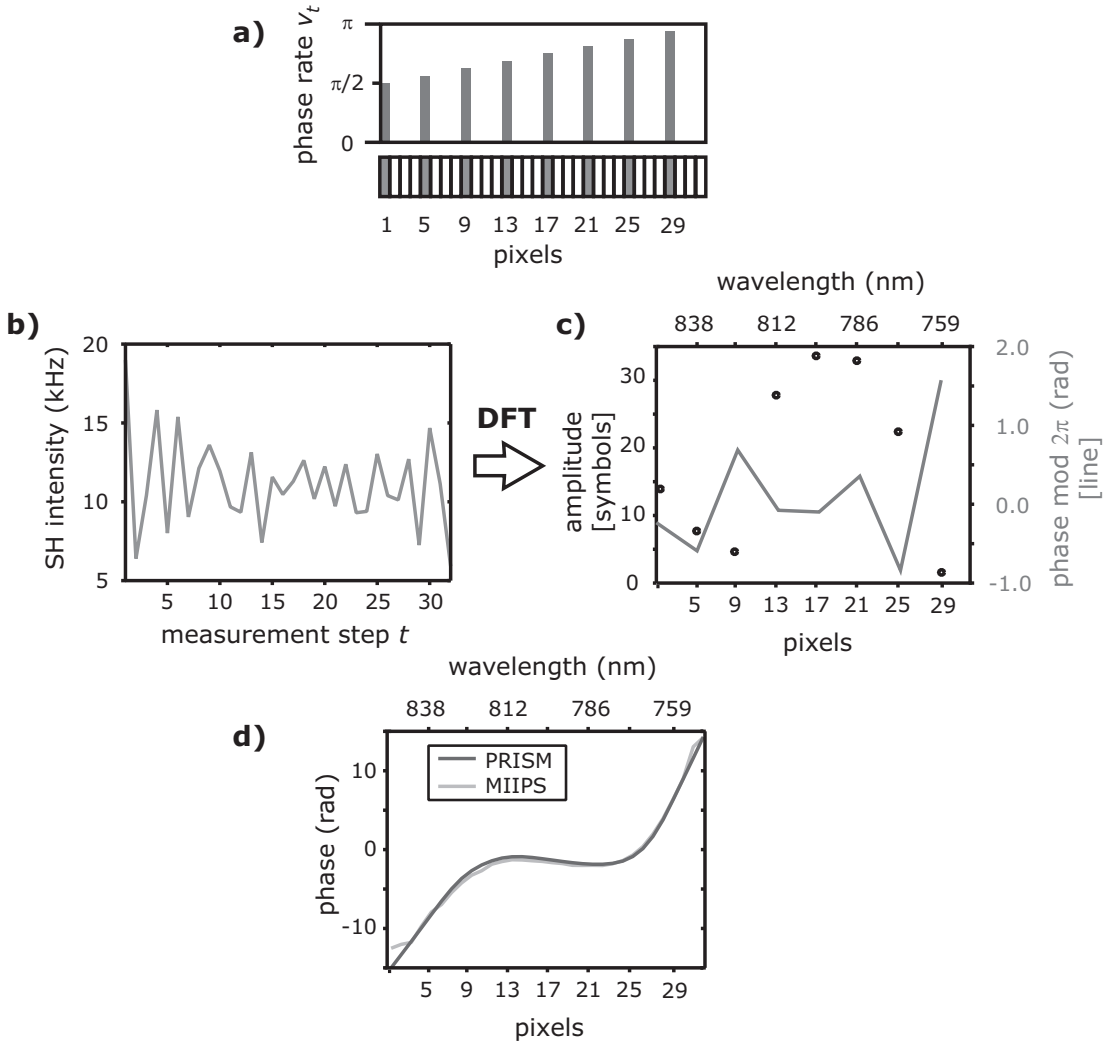

Figure 2.9: Working principle of PRISM at the example of a 32 pixel pulse shaper, divided into 4 groups. (a) Rate of phase progression v_n for the pixels of group no. 1. (b) Measured data of the pulse in the focus of an NA 1.3 objective. (c) Discrete Fourier transform (DFT) of a) gives the phase for each modulated pixel (solid line). (d) PRISM phase after 3 iterations in comparison to a fully converged MIIPS measurement (8 iterations).

the reference measurement, done by MIIPS. Different than other methods presented here, PRISM aims to find the phase of a pulse and not the GDD. Of course, the zeroth and first polynomial order of the phase are inaccessible to PRISM as well. But cases exist, in which the phase profile is well defined, but the GDD is not. Examples are sudden phase

[6]The available 128 pixel pulse shaper was used here but 4 pixels were pooled to a virtual single one.

steps or kinks[7] in the phase, which have undefined second-order phase profiles. As these situations are borderline cases that do not appear in typical scenarios, they are not a real problem for established methods such as MIIPS. With the pulse shaper it is nevertheless possible to introduce such a phase distortion intentionally to verify whether it is possible to retrieve the correct phase profile or not. Indeed, PRISM is able to resolve the phase step (see fig. 2.10) and therefore to recover the original pulse shape.

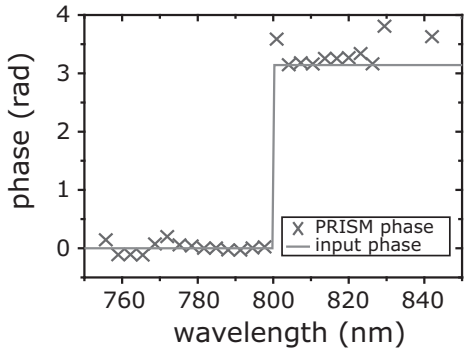

Figure 2.10: Demonstration of the phase retrieval of a π-step in the phase profile, intentionally introduced by the pulse shaper. Measurement was performed on SH of $Fe_2(IO_3)_3$ nanocrystals with $N = 32$, $g = 4$, using 5 iterations.

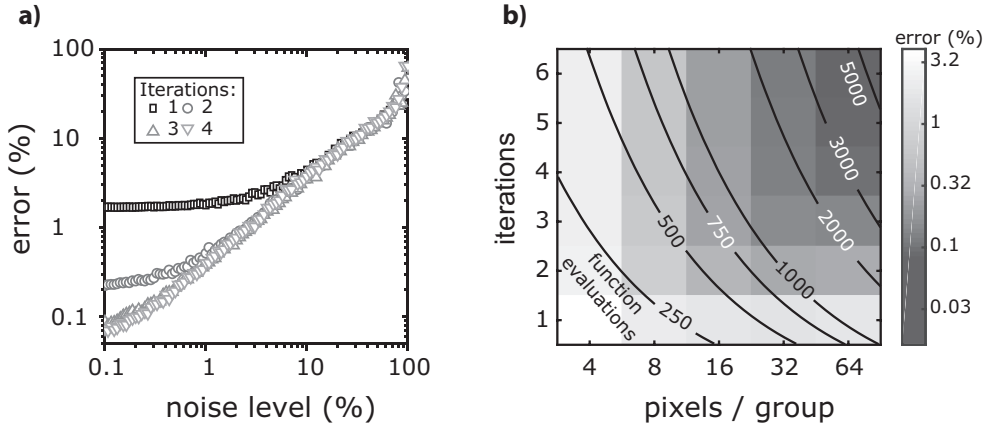

Figure 2.11: Accuracy and convergence behavior of PRISM (simulations). (a) Error of the retrieved phase in dependence of the overall noise level of the measurement ($N = 32$, $g = 4$). (b) Error in dependence of iteration number and pixels per group (w.o. noise). Lines indicate the total number of measurement points.

Since PRISM takes only a few measurements per pixel to measure the phase, it is fast on one hand, but sensitive to experimental noise on the other hand: the total accuracy of the measurements is directly limited by the error bar of the measured intensity. Increasing

[7] A kink in the phase profile appears for example in the V-shaped phase, see sect. 2.1.3.

the number of iterations only makes sense if the signal-to-noise ratio is excellent, i.e. better than 1 % for more than two iterations. Fig. 2.11 puts together results of simulations of the PRISM method, where the available parameters have been scanned. The error, given as an average deviation of the retrieved phase from the distortion phase, is compared to the noise level of the simulated measurements (fig. 2.11a), and to the number of pixels per group, as well as to the number of iterations (fig. 2.11b). The test phase used for these examples was the phase of a harmonic oscillator model in order to compare to the measurements of sect. 4.1. As can be seen from fig. 2.11a, choosing 3 iterations leads to highest possible accuracy in the presence of noise for most measurements. The conclusion and recommendation is that a workable compromise of accuracy and the total number of measurement points is given by 3 iterations and 8 pixels per 4 groups, as can be seen from fig. 2.11b.

2.3.3 Multiphoton Intrapulse Interference Phase Scans (MIIPS)

"Multiphoton intrapulse interference phase scans" (MIIPS) is a method for phase retrieval using an optical pulse shaper and the second harmonic spectrum of a (flat-phase) reference material that has been introduced by Lozovoy et al. in 2004 [6]. It uses a series of sinusoidal test phase profiles, applied to the laser, and records the corresponding SH spectra of the sample. The resulting 2D map shows characteristic features that can be evaluated to approximately retrieve the phase distortions, present in the pulse. By applying the algorithm in an iterative fashion, the phase profile can be evaluated to a high level of accuracy.

In the following section, the original algorithm is reviewed, along with example phase scans recorded during this work. Afterwards, recent improvements of the phase scan (gated MIIPS) and the phase retrieval algorithm itself (improved MIIPS) from our group are presented. The main ideas of these improvements stem from the work of Comin et al. [11, 12].

Standard MIIPS

The second harmonic spectrum of a flat-phase material with instantaneous SHG can be calculated as follows [63]:

$$I^{SH}(2\omega) = c\varepsilon_0 \left| \chi^{(2)} \int_0^\infty d\Omega \quad E(\omega - \Omega) \cdot E(\omega + \Omega) \right|^2 , \tag{2.25}$$

where $E(\omega)$ is the complex electric field and $\chi^{(2)}$ the second order susceptibility of the material. During a MIIP scan, a test phase $\phi(\omega)$ will be added to the original but unknown phase $\varphi(\omega)$ of the laser pulse:

$$E_{MIIPS}(\omega) = |E(\omega)| \cdot e^{i[\phi(\omega)+\varphi(\omega)]}. \tag{2.26}$$

Expanding the phase of the field to orders of Ω, eq. 2.25 can be written as:

$$I^{SH}_{MIIPS}(2\omega) = c\varepsilon_0 \Big| \chi^{(2)} \int_0^\infty d\Omega \quad |E(\omega-\Omega)| \cdot |E(\omega+\Omega)| \times \\ \times \exp\left[i\big(1/2(\phi''(\omega)+\varphi''(\omega))\Omega^2 + 1/12(\phi^{(iv)}(\omega)+\varphi^{(iv)}(\omega))\Omega^4 + \dots\big)\right]\Big|^2. \tag{2.27}$$

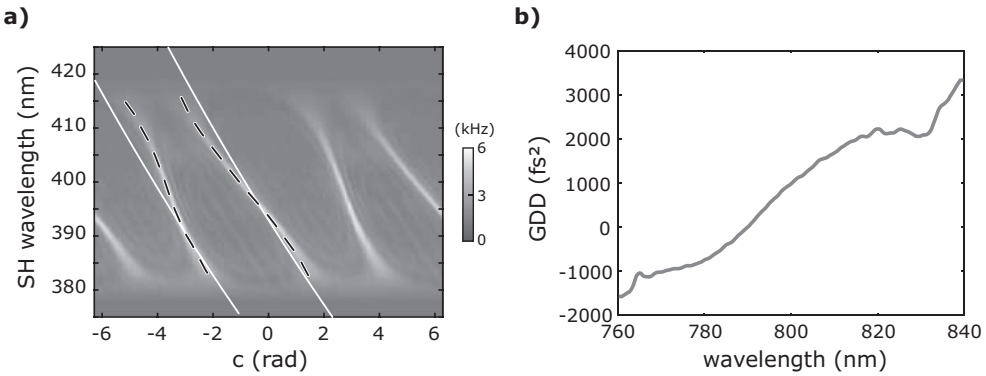

Figure 2.12: (a) Example of a MIIP scan in the focus of a NA 1.3 microscope objective. The black dashed lines indicate the maximum position of the traces, the white solid lines indicate the position of zero phase distortion. Scanning parameters were: $a = 10\,\text{rad}$, $b = 20\,\text{fs}$, $\Delta c = \pi/100$. (b) GDD retrieved from the maximum positions in (a), demonstrating a large amount of phase distortion.

Since the zeroth and first order of the phase do not contribute to the SH intensity, they do not occur in the formula. To second-order accuracy the condition for a maximum in the second harmonic spectrum reads:

$$\phi''(\omega) + \varphi''(\omega) = 0. \tag{2.28}$$

This condition is fulfilled, if the local second derivative (GDD) of the phase $\varphi(\omega)$ at the frequency ω is eliminated by the test phase $\phi(\omega)$ which then leads to efficient SHG. Lozovoy et al. propose a sinusoidal test phase of [6]:

$$\phi(\omega) = a \cdot \sin(b \cdot (\omega - \omega_0) - c) \tag{2.29}$$

with ω_0 being the central frequency of the laser pulse. a and b are parameters of the test phase that determine the range and accuracy of the phase scan, while c is scanned in steps of Δc over a range of at least 2π. A MIIPS measurement results in a spectrogram of the SH versus the scanning phase c and is shown in fig. 2.12a. There are curved lines of maximum intensity visible in the map, which are the MIIPS "traces". These traces determine the positions where the local GDD is equal to the second derivative of the test phase and hence the above mentioned condition is fulfilled. As the test phase $\phi(\omega)$ is 2π-periodic within c,

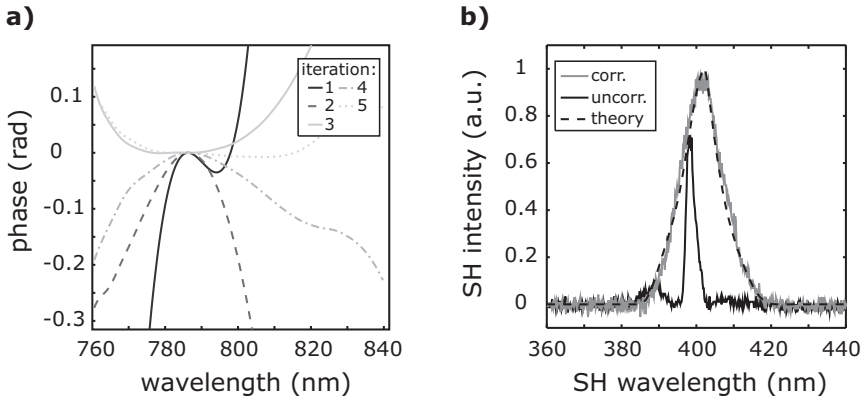

Figure 2.13: (a) Correction phases, retrieved in five successive MIIPS iterations. The phase profiles converge towards zero. The overall correction phase is the sum over all iterations (not shown). (b) Spectra of the second harmonic with and without the final phase correction, compared to the theoretical flat-phase SH spectrum.

the traces repeat themselves without adding more information. Evaluating the maximum position $c_{max}(\omega_{SH})$ for all SH frequencies $\omega_{SH} = 2\omega$ is the main step of the MIIPS method and has to be done by a peakfinding algorithm of choice. Depending on the signal-to-noise ratio, the resulting function can be ambiguous, particularly at the wings of the spectrum. The local GDD of the pulse is calculated from the function $c_{max}(\omega_{SH})$ (see fig. 2.12b):

$$\varphi''_{MIIPS}(\omega) = a \cdot b^2 \cdot \sin(b \cdot (\omega - \omega_0) - c_{max}(2\omega)). \tag{2.30}$$

The last step is the calculation of the phase $\varphi_{MIIPS}(\omega)$ by double integration of $\varphi''_{MIIPS}(\omega)$ with arbitrary integration constants. In most cases, at least two traces, carrying the same information, are completely visible in a MIIPS spectrogram, so the retrieved GDD is the mean value of the individual traces. A single iteration of MIIPS cannot retrieve the spectral phase very accurately, so a number of iterations has to be performed in order to achieve a reasonable precise result. As for microscopy, the number of iterations used varies between 4 and 20, strongly depending on the total GDD, the necessary exactness, the used parameters a, b, and Δc, and the setup-specific signal-to-noise ratio. The example shown in fig. 2.12 was measured using the setup described in sect. 2.2. The GDD retrieved during this scan spans more than $4000\,\mathrm{fs}^2$, which is a typical value for microscope objectives. Since the function is nearly linear, it can be concluded that a strong third order phase distortion was present at the laser pulse in the focus of the microscope objective. Around the central wavelength of the laser of 800 nm the GDD crosses zero which is not expected if centimeters of glass were introduced to the beam path. The reason for this is that the laser pulses get pre-compressed by the prism compressor before entering the microscope (c.f. sect. 2.2), which is able to remove the *mean* GDD of the entire pulse. The very strong remaining phase distortion that was measured here demonstrates the importance of additional and sophisticated phase retrieval and compression of broadband laser pulses if the bandwidth limit needs to be reached. In fig. 2.13, a convergence plot of five successive

MIIPS iterations is shown alongside different second harmonic spectra recorded with and without the retrieved phase correction. The magnitude of the phase correction that is determined in every iteration step constantly decreases. After the process has converged to an acceptably flat resulting phase, the theoretical second harmonic spectrum for a bandwidth limited laser pulse, calculated using the laser fundamental spectrum, is nicely matching the measured one. We usually interpret the converged MIIPS method and the SH spectrum matching the expectation for a bandwidth limited laser pulse such, that the bandwidth limit has been reached, i.e. the pulses are as short as they can get. On the basis of such a pulse correction, measurements on other materials can be carried out where the pulse profile is intentionally manipulated.

According to eq. 2.30, the maximum GDD that can be tested by MIIPS, is $GDD_{max} = \pm a \cdot b^2$. At a maximum relative error of the GDD of $\varepsilon = \Delta GDD/GDD$, it can be shown that the total accuracy cannot be better than $GDD_{min} = a \cdot b^2\sqrt{1 + (\varepsilon/\Delta c)}$. These two numbers should be considered when choosing the MIIPS parameters a, b, and Δc for measurements. Sect. 2.3.5 presents a detailed discussion on the level of precision to be reached by MIIPS and other phase measurements.

Gated MIIPS

The following section is based on the publication: "Compression of ultrashort laser pulses via gated multiphoton intrapulse interference phase scans" in Journal of the Optical Society of America B (2014), by Comin et al. [11], reproducing theory and figures.

Gated MIIPS (G-MIIPS) is a variation of MIIPS that uses an improved scanning algorithm which is able to compress a laser pulse with fewer iterations than the original MIIPS [11]. The initial idea is that the central condition of MIIPS eq. 2.28 in combination with the sinusoidal test phase has only a small validity range of the phase expansion that was carried out in the first place (eq. 2.27). The reason is that the test phase $\phi(\omega)$ has of course, higher orders that will influence the MIIPS measurement and the pulse phase $\varphi(\omega)$ may have them too. Consequently, the condition in eq. 2.28 should be rewritten:

$$\left(\phi''(\omega) + \frac{1}{6}\phi^{(iv)}(\omega) + \dots\right) + \left(\varphi''(\omega) + \frac{1}{6}\varphi^{(iv)}(\omega) + \dots\right) = 0.$$

Gated MIIPS aims at reducing the effect of the higher orders by restricting the available laser spectrum. For that purpose, an amplitude gate is used in addition to the sinusoidal test phase. The phase and amplitude masks for G-MIIPS with a Gaussian gate read:

$$\begin{aligned} \phi(\omega, c) &= a \cdot \sin(b \cdot (\omega - \omega_0) - c), \\ M(\omega, c) &= \exp\left[-\left(\frac{b \cdot (\omega - \omega_0) - c}{\sigma}\right)^2\right]. \end{aligned} \tag{2.31}$$

As the test phase progresses with c, the amplitude gate, centered at the frequency c/b, selects a small part of the spectrum with a width of σ. Since at every phase point c only

a small part of the spectrum contributes to the G-MIIPS map, the higher order terms are much less significant than for standard MIIPS. Therefore the advantage of G-MIIPS comes from the reduced error made by the second-order approximation of the local phase. After a scan, the phase is evaluated in the standard way with the exception that there is only a single trace in the map.

Fig. 2.14 shows an example G-MIIPS spectrogram, where the beam of a bandwidth limited laser pulse has traveled through 23 mm of SF10 glass as a reference phase distortion, resulting in an average GDD of as much as 3600 fs^2. The GDD of the laser pulse gets

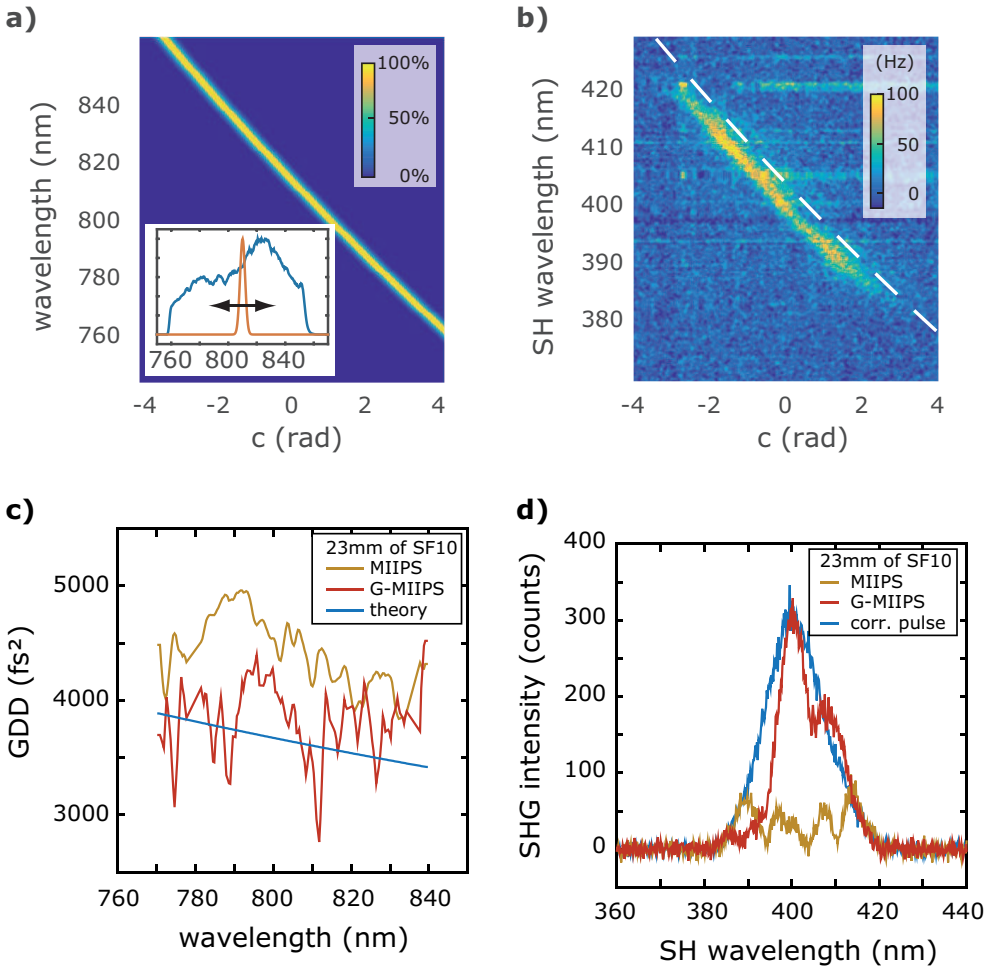

Figure 2.14: Demonstration of G-MIIPS for an introduced 23 mm of SF10 glass into the beam path of a compressed laser pulse. (a) Amplitude gate, using the parameters $a = 10$, $b = 25$ fs, and $\sigma = 0.18$. Inset shows the gate for $c = 0$ in front of the laser spectrum. (b) G-MIIPS spectrogram with the previous parameters. The dashed white line indicates the position of zero phase distortion. (c) Retrieved GDD in comparison to MIIPS and the theoretical value for the SF10 glass. (d) SH spectra after a single iteration of MIIPS, G-MIIPS and from a fully compressed pulse. *Adapted from Comin et al.* [11]

approximated much better by G-MIIPS than by MIIPS, however at the cost of a much lower total signal. In the present case, the total detected intensity of G-MIIPS was a factor 5 lower than for standard MIIPS, which can also be seen in the reduced signal-to-noise ratio of the GDD in fig. 2.14c. There is a general mismatch between signal-to-noise and accuracy: the latter is primarily determined by the MIIPS parameters and the gate width σ. One would like to decrease the gate size as much as possible in order to enhance the validity of the underlying series expansion of the phase, but this decreases the excitation intensity at the sample significantly. Therefore, the measurement has to be carried out for a longer time to not be limited by noise. Although gated MIIPS already presents an improvement to standard MIIPS, a way to overcome the problem of a reduced signal is shown in the next section.

Improved MIIPS

The following section is based on the publication: "Phase retrieval of ultrashort laser pulses using a MIIPS algorithm" in Optics Express (2016), by Comin et al. [12], reproducing the main points of the theory.

The MIIPS algorithm can be improved, even without changing the scanning technique. Standard MIIPS uses a local polynomial expansion of the phase of the electric field in eq.2.25. The series expansion that affects the phase term but *not* the amplitude term contains an approximation, limiting the validity of the procedure as such. This is the main reason why the MIIPS algorithm, also in case of an idealized, noise free measurement, is not able to retrieve the correct phase of a laser pulse in a single iteration.

The idea of improved MIIPS is to take the laser spectrum as extra information into account. With the laser spectrum known and the usual assumption of a homogeneous and instantaneous SHG, the theoretical SH spectrum for arbitrary phases can be calculated using eq. 2.25. The goal is to find a phase profile that reproduces a SH spectrogram of a MIIP scan, resembling a measured one as closely as possible. If such a phase profile is found, it is assumed to be the phase profile of the laser pulse. The improved MIIPS algorithm suggests a feedback mechanism to determine this phase, based on repeated calculation of the theoretical MIIPS map without the need to iterate the physical measurement as in standard and gated MIIPS. The method is limited by the resolution of the scan only, given by GDD_{min} and GDD_{max}. In the following, a detailed recipe for the procedure of phase retrieval with the help of the laser spectrum $I_{laser}(\omega) \propto |E_0(\omega)|^2$ is given:

1. Record a MIIPS spectrogram $I_{MIIPS}^{SH,exp}(c, 2\omega)$ in the range $c \in [-\pi, \pi]$. Use the standard peakfinding algorithm in order to get the first guess of the second-order phase φ''_{exp}, which will serve as reference to the experiment throughout the process. From this, calculate the first iteration of the phase by double integration: $\varphi_1 = \int\int \varphi''_{exp} d\omega d\omega$. This is iteration $n = 1$.

2. Calculate a MIIPS spectrogram $I_{MIIPS}^{SH,theo}(c, 2\omega)$ using the known laser spectrum and the phase approximation φ_n. Use the standard peakfinding algorithm in order to get

a second-order phase φ''_{fb} from the theoretical map, which will serve as a feedback to the current iteration.

3. The difference between the feedback term and the experimental second order phase $\delta = \varphi''_{fb} - \varphi''_{exp}$ reflects the error of the current iteration. A new iteration is now given by: $\varphi''_{n+1} = \varphi''_n - k \cdot \delta$. The numerical constant k can be tuned in order to improve the overall convergence. A good value to start with is $k = 0.5$.

4. Calculate the phase for iteration $n+1$ by double integration: $\varphi_{n+1} = \int\int \varphi''_{n+1} d\omega d\omega$.

5. Repeat the algorithm, starting at number 2.

6. Stop iterating when the estimated error δ is smaller than the experimental accuracy GDD_{min}.

Since the sinusoidal test phase is monotonic in the range $c \in [-\pi, \pi]$, the sign of the error δ is always correct in a sense that the error can be used to improve the current "guess" of the GDD φ''_n. With the use of the improved MIIPS retrieval algorithm, there is no need to iterate the physical experiment any longer to extract all phase information, present in a MIIPS trace. An example MIIP scan is shown in fig. 2.15 together with the fitted GDD and, as a comparison, the experimental GDD, obtained by 8 MIIPS iterations. Both GDD curves show that the result is identical. The MIIPS spectrogram, calculated on the basis of the retrieved phase and the laser spectrum, resembles the experimental one very nicely, which demonstrates the applicability of the method.

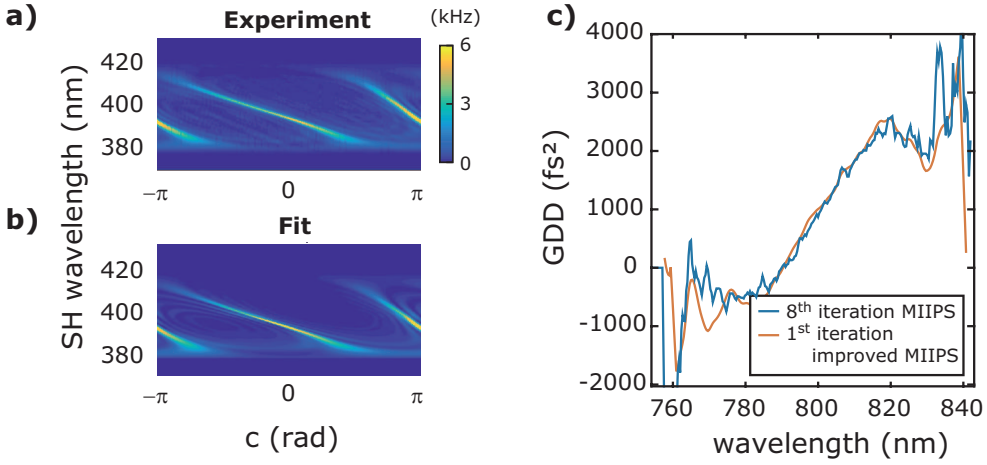

Figure 2.15: Demonstration of the improved MIIPS algorithm. (a) First iteration of a measured MIIPS spectrogram ($a = 10\,\text{rad}$, $b = 20\,\text{fs}$). (b) Calculated spectrogram from the MIIPS phase, retrieved with the improved algorithm, and the input laser spectrum. (c) Comparison of the MIIPS GDD from the improved algorithm with a converged MIIPS series of 8 iterations. Both methods yield the same result which demonstrates that improved MIIPS is more practical than standard MIIPS.

The fact that only a single measurement has to be taken can be a decisive improvement in the case of nanostructures with limited photostability. In terms of speed, it is clear that an improvement of a factor 5 to 10 is reached, depending on the commonly used number of iterations. Only if the experimental accuracy has to be enhanced, a new MIIPS trace with different parameters a, b, and Δc has to be recorded.

2.3.4 Spectrally resolved chirp scans

MIIPS is a method, based on the second harmonic spectrum of a sample material, using a sinusoidal test phase. In order to obtain phase information from the peak position of a second harmonic spectrogram, other suitable test phase profiles can be used too. One particularly simple method is to do spectrally resolved chirp scans [69, 70]. During the course of this work, this variation of MIIPS was often used in a semi-automatic fashion for everyday pulse compression. A chirp scan adds a second-order polynomial phase to the laser pulse and scans its magnitude c while recording the SH spectrum:

$$\phi_{test} = \frac{c}{2}(\omega - \omega_0)^2, \tag{2.32}$$

with ω_0 being the central frequency. At the maximum of the second harmonic in c, the applied chirp compensates the local GDD to the same order of accuracy as standard MIIPS. Therefore, the maximum position of c can be directly identified with the local GDD, which is shown in fig. 2.16.

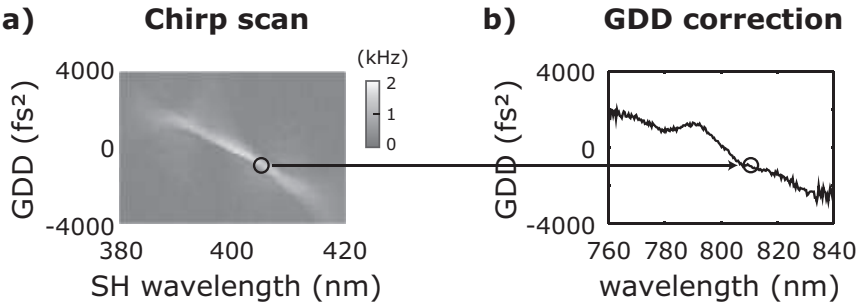

Figure 2.16: (a) Second harmonic spectrograms of a chirp scan. (b) The GDD of the laser pulse $GDD = \phi''(\omega)$ can directly be retrieved from the maximum position of the applied chirp c: $\phi''(\lambda) = -c_{max}(\lambda/2)$.

In more detail, a laser pulse with applied chirp c has the following complex valued electric field:

$$E(\omega, c) = |E(\omega)| \cdot \exp\left[i(\varphi(\omega) + c/2 \cdot (\omega - \omega_0)^2)\right], \tag{2.33}$$

with $\varphi(\omega)$ being the laser pulse phase profile which shall be determined. The second

harmonic spectrum from eq. 2.25 then reads:

$$I_{CS}^{SH}(2\omega, c) \propto \Big| \int_0^\infty d\Omega \quad |E(\omega-\Omega)| \cdot |E(\omega+\Omega)| \times \\ \times \exp\Big[i\big(\varphi(\omega-\Omega)+\varphi(\omega+\Omega) + c/2 \cdot \big((\omega-\Omega-\omega_0)^2 + (\omega+\Omega-\omega_0)^2\big)\big)\Big]\Big|^2.$$

Again, the phase is expanded to powers of Ω around ω and the first two terms are dropped, such that the approximation to the quadratic term reads:

$$\varphi(\omega-\Omega) + \varphi(\omega+\Omega) + c/2 \cdot \big((\omega-\Omega-\omega_0)^2 + (\omega+\Omega-\omega_0)^2\big) \approx (\varphi''(\omega) + c) \cdot \Omega^2.$$

The approximated second harmonic spectrum is now given by:

$$I_{CS}^{SH}(2\omega, c) \propto \Big| \int_0^\infty d\Omega \quad |E(\omega-\Omega)| \cdot |E(\omega+\Omega)| \cdot \exp\Big[i\big((\varphi''(\omega) + c) \cdot \Omega^2\big)\Big]\Big|^2. \tag{2.34}$$

The SH is maximized for:

$$\varphi''(\omega) = -c_{max}(2\omega), \tag{2.35}$$

so (unlike MIIPS) a peakfinding algorithm will directly give an approximation of the local GDD by the position of the maximum. It is easy to show, that eq. 2.34 is symmetric in c: $I_{CS}^{SH}(2\omega, c) = I_{CS}^{SH}(2\omega, -c)$; so the maximum position with respect to c coincides with the "center of mass":

$$c_{max}(2\omega) \equiv c_{com}(2\omega) = \frac{\int_{-\infty}^{\infty} dc \quad c \cdot I_{CS}^{SH}(2\omega, c)}{\int_{-\infty}^{\infty} dc \quad I_{CS}^{SH}(2\omega, c)}. \tag{2.36}$$

Finding the center of mass of a 2D spectrogram is simple and robust in comparison with finding the maximum, and in case of a low signal-to-noise ratio, this can be a decisive advantage. The validity of the approach is, as for standard MIIPS, restricted by the validity of the power series expansion of the phase term in eq. 2.25, but this time there are no higher orders of the test phase that introduce further errors. If substantial higher order terms occur for the approximation of the local phase, the identification of applied chirp with GDD is not correct anymore. In this case, an iterative procedure can be used, since the chirp c will always underestimate the real GDD. Fig. 2.17 shows the working principle of this approach in five iterations, using a decreasing scanning range in order to successively enhance the resolution.

A similar method has also been used without liquid crystal pulse shapers by inserting wedges of glass into a negatively chirped laser beam [71]. That way, it is also possible to accurately determine the phase of the laser pulse, but it cannot be compensated to the same order of accuracy.

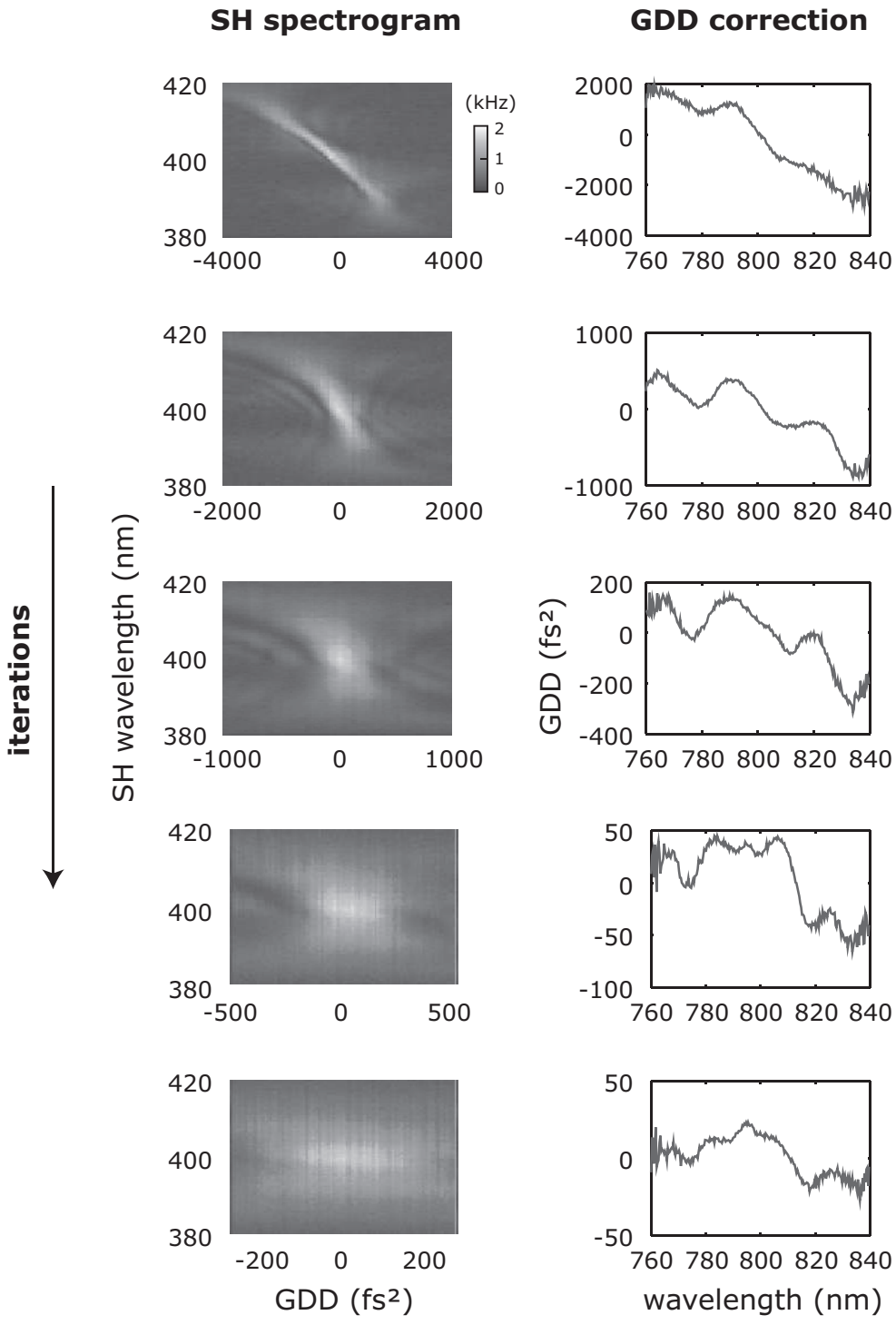

Figure 2.17: Second harmonic spectrograms of successive chirp scans. Each chirp scan gives an approximate GDD correction, which is applied to the pulse. Then the chirp scan is repeated with higher accuracy.

Compared to standard MIIPS, chirp scans have three advantages. First, the phase approximation works better because no error is made in the second-order approximation of the (second-order) test phase. Second, the peakfinding is simpler, because the maximum in c coincides with the center of mass, which can be determined in a very robust way even for low signal quality. And third, the overall detected second harmonic intensity is usually larger than for MIIPS, because the phase distortion introduced by the test phase is less severe than in case of the sinusoidal phase profile, which makes SHG more efficient. Compared to G-MIIPS, the last two points still hold, but depending on the phase distortions present in the system, the advantage of G-MIIPS can overrule them. The improved MIIPS algorithm outperforms the iterative chirp scan technique by far for the same reasons as it outperforms the other MIIPS variants. The algorithm of the improved MIIPS data evaluation can be applied to spectrally resolved chirp scans with only minor adjustments concerning the analysis of the GDD.

2.3.5 Remarks on the accuracy of MIIPS-based schemes

In this section, the experimental and theoretical limits of the used, pulse shaper based, approaches are discussed in an application oriented fashion. Additional experiments which can verify the retrieved pulse characteristics are presented as well as an estimation of the fourth-order error made in the central assumption of MIIPS. This is of particular importance, since it is generally anticipated that a converged MIIPS measurement yields a bandwidth limited laser pulse in the microscope's objective focus.

Benchmark tests

In a measurement, many features of the apparatus and the surrounding will influence the results in an unwanted fashion. Therefore only relying on a single method for pulse compression or characterization is not advisable since it can happen that phase distortions are overlooked in one particular method that would be easily visible in a second one. Unfortunately, the detection sensitivity itself is also able to alter the results in a way, as it is usually caused by phase distortions. If, for example, the spectral detection sensitivity is not accurately corrected, the theoretical and experimental SH spectra cannot overlap which would be a problem for improved MIIPS. Establishing reference experiments is therefore an important prerequisite for reliable experiments with bandwidth limited femtosecond laser pulses. During the course of this work, the following benchmark tests have been implemented and are now routinely used in our laboratory:

- Autocorrelation scans,
- Phase measurements of reference distortions,
- Comparison of the SH spectrum with the theoretical SH spectrum,
- The symmetry of spectrally resolved chirp scans.

Fig. 2.18 presents examples of all four mentioned methods, which are explained in detail below. All measurements were done on $Fe_2(IO_3)_3$ nanocrystals.

Autocorrelation (AC) scans can be carried out with the pulse shaper by introducing a cosine amplitude mask (see sect. 2.1.3). The theoretical AC scan for a bandwidth limited pulse can be calculated from the laser spectrum and serves as a reference for the quality of the pulse compression. The goal is to have fully overlapping curves whereas deviations from the optimal shape can be a sign of incorrect phase correction. Fig. 2.18a shows an example AC scan for an almost compressed laser pulse. The theoretical and the experimental curves which are scaled to the same height do not overlap perfectly, so it is desirable to determines the magnitude of the distortion. One way is to use the full-width-at-half-maximum (FWHM) of the curve and compare this to the theoretical case of a bandwidth limited pulse. In the present case this yields a value of 28.5 fs for the experimental curve (black line) and 30.2 fs for the theoretical (red line). Therefore the mistake does not originate from the phase but from the incorrectly recorded laser spectrum. As a comparison, simulated

residues between the bandwidth limited ($0\,\mathrm{fs}^2$) and distorted curves are plotted below the autocorrelation trace: $Res(t) = I_{0\,\mathrm{fs}^2}(t) - I_{dist}(t)$. They show that a phase distortion of $50\,\mathrm{fs}^2$ would barely be visible as a divergence from the best case AC trace.

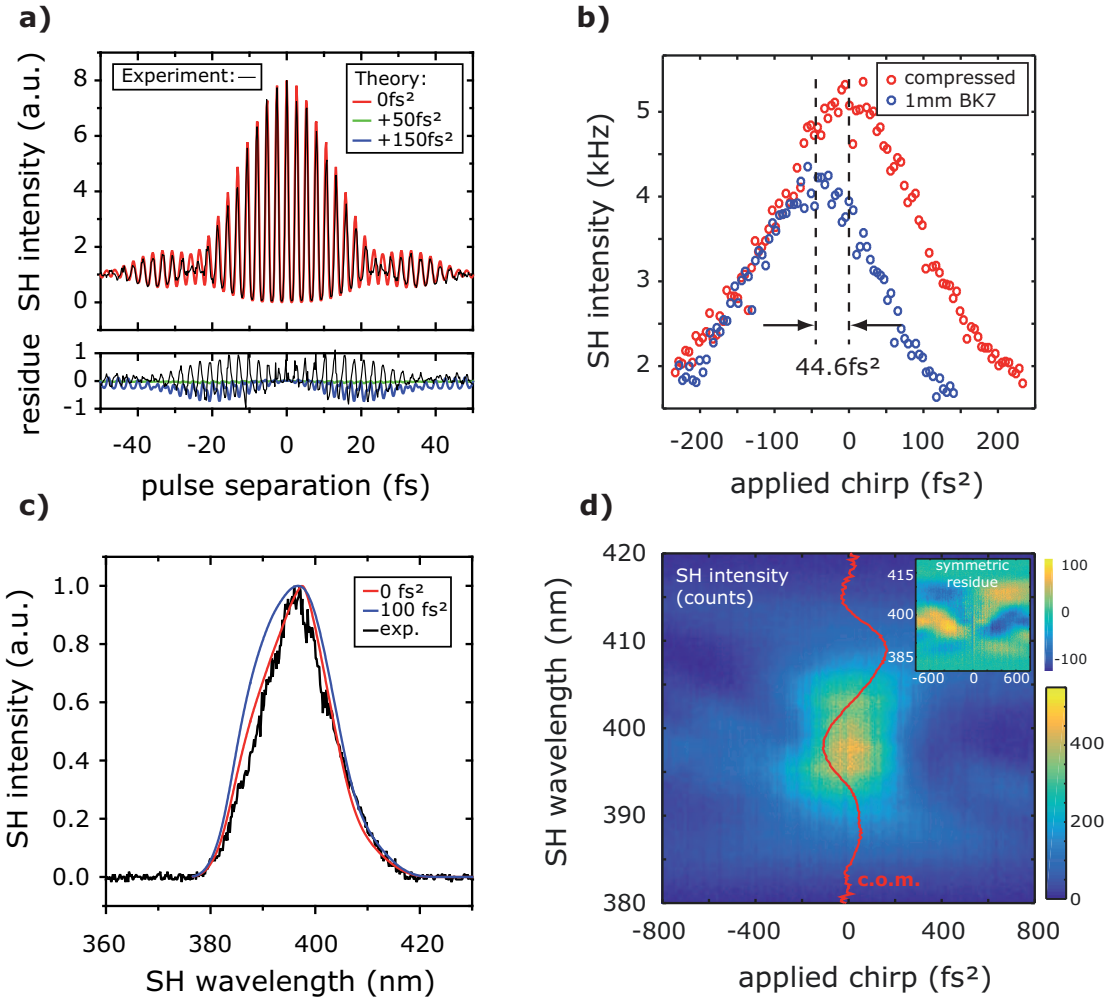

Figure 2.18: Quality checks for pulse compression, based on measurements of the second harmonic (SH): (a) Autocorrelation scan, (b) chirp scans, (c) SH spectrum, (d) spectrally resolved chirp scan. See main text for details.

Chirp scans have already been presented as a method to retrieve phase information (see sect. 2.3.2). Their accuracy is relatively high, as can be seen from fig. 2.18b. A chirp scan of a compressed laser pulse (red circles) is shown and compared to a second scan (blue circles), where a plate of 1 mm BK7 glass has been inserted as a known phase distortion. A chirp offset of $44.6\,\mathrm{fs}^2$ is expected at a central wavelength of 800 nm (c.f. tab. 2.1), visualized by the dashed lines. They coincide accurately with the maxima of the measured curves, which implies that a residual GDD of lower than $50\,\mathrm{fs}^2$ can be easily measured.

Fig. 2.18c presents the measured SH spectrum (black line) together with the theoretical bandwidth limited curve (red line) and a curve with $100\,\mathrm{fs}^2$ GDD (blue line). All are

scaled to 1 since the total intensity, which is determined by the efficiency of the measured nanocrystal, is generally unknown. The only criterion is then the shape of the spectrum, whose sensitivity can be estimated to $50 \ldots 100\,\mathrm{fs}^2$, depending on the signal-to-noise ratio. An advantage is that the measurement of a single SH spectrum is a very quick check, compared to the recording of AC traces or chirp scans.

The fourth method is shown in fig. 2.18d for a slightly distorted (i.e. not fully compressed) laser pulse. The spectrally resolved chirp scan takes more measurement time than the previous checks, but is most sensitive to residual phase distortions. It is plotted together with its center-of-mass (c.o.m.) which reveals s local GDD of up to $200\,\mathrm{fs}^2$. Importantly, the *mean* GDD of the pulse amounts to $0\,\mathrm{fs}^2$, so a measurement in the fashion of fig. 2.18b would have given the wrong result. The inset shows the symmetric residue (with a different color scale), calculated as: $I_{res}(\lambda, c) = I(\lambda, c) - I(\lambda, -c)$. Apart from the center of mass it directly gives a visual feedback on the quality of the previous pulse compression steps.

To summarize, there are many ways to check the quality of a pulse compression. Autocorrelation scans are historically very popular, but they only provide very limited accuracy. If one is using a pulse shaper, there are better and faster ways to verify the pulse shape. Comparing the second harmonic spectrum to the theoretical shape of a bandwidth limited laser pulse is a quick check, but its accuracy is limited. Both methods rely on the very accurate measurement of the fundamental laser spectrum and a spectrally flat detection sensitivity of the second harmonic signal. Chirp scans give a feedback on the pulse by the shift of their maxima, which can be spectrally integrated or resolved. The accuracy of those scans is superior to the other two mentioned methods and it does not rely on the knowledge of the laser spectrum.

Limitations of MIIPS from theory

The central simplification made by MIIPS and related methods is that the phase can be locally approximated by its second order. This simplification is only allowed if the higher local orders are small compared to the local second order. The effects of higher order phase distortions in the pulse have already been discussed in the sections about G-MIIPS and improved MIIPS (sect. 2.3.3), here the introduced error by the sinusoidal test phase will be discussed, which sets a theoretical limit to the usability of this kind of test phase. Remembering the phase term of eq. 2.25 while dropping the zeroth and first order:

$$\phi(\omega + \Omega) + \phi(\omega - \Omega) \approx \phi''(\omega) \cdot \Omega^2 + \underbrace{\frac{1}{12}\phi^{(iv)}(\omega) \cdot \Omega^4}_{\text{phase error}} + \ldots, \tag{2.37}$$

a formula for the total error of the phase is derived. The residuals to the local second-order approximation of the phase by its second derivative $\phi''(\omega)$ represent the error estimate. To leading order, this is equal to the fourth order term. In order to quantify it for a given laser pulse, the integrand Ω is replaced by the pulse width $\Delta\omega$, which is a conservative guess, and the frequency dependent fourth order $\phi^{(iv)}(\omega)$ is replaced by a typical value for

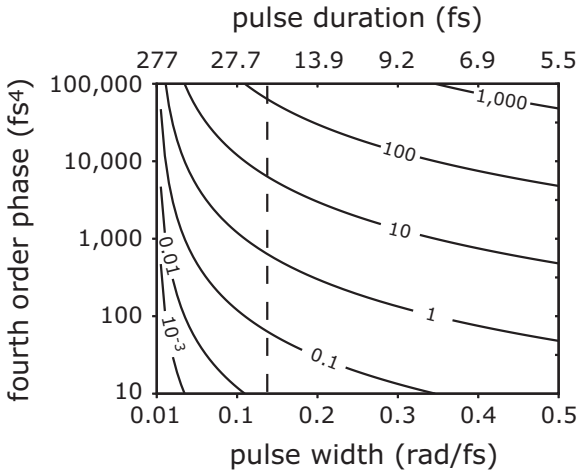

Figure 2.19: Logarithmic contour plot of the error of the second-order phase approximation vs. spectral pulse width and the fourth order phase. The labels at the solid lines are given in fs^2, representing the error in GDD. The dashed line indicates the used laser bandwidth. If an error of $10\,\mathrm{fs}^2$ over the spectrum is permissible, the fourth order phase distortion has to be smaller than $6,500\,\mathrm{fs}^4$ for the present system.

the respective spectrum $\Phi^{(iv)}$. The value of $\Phi^{(iv)}$ can in this context be interpreted as the maximum permissible fourth order phase error throughout the full spectrum. The error estimate ε for the GDD then reads:

$$\varepsilon = \frac{1}{12}\Phi^{(iv)} \cdot \Delta\omega^2. \tag{2.38}$$

Fig. 2.19 gives an overview about the consequences of this error. In cases where a high fourth order is present in the laser pulse, iterating MIIPS often improves the result. As can be seen from eq. 2.38, the error always has a sign which leads to an underestimation of the retrieved GDD, so it can be successively eliminated by iterating the procedure. If the fourth order is above the permissible error threshold, given in fig. 2.19, then iterations will not improve the situation.

During a MIIP scan, the maximum fourth order of the sinusoidal test phase amounts to:

$$\phi^{(iv)}_{MIIPS}(a,b) = a \cdot b^4. \tag{2.39}$$

This fourth order is unwanted and, depending on the used MIIPS parameters, features a severe additional phase which leads to an incorrect phase retrieval [11, 12]. In case of gated MIIPS, this is not a big problem, since the spectrum is reduced such that much higher local errors can be tolerated. The error in local GDD that can result from this term is given in fig. 2.20. This figure, together with fig. 2.19, highlights the subsistent reason for the need to iterate the MIIPS process. The fourth order of the scanning test phase profile creates a local phase distortion which becomes even more pronounced if the values

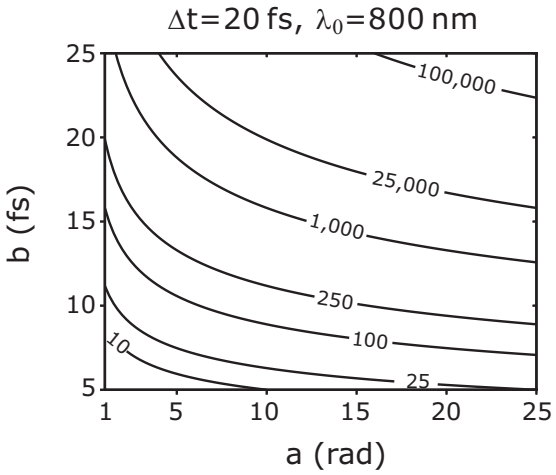

Figure 2.20: Logarithmic contour plot of the maximum error of MIIPS vs. the scanning parameters a and b for the case of a 20 fs Gaussian laser pulse, centered at 800 nm. The labels at the solid lines are given in fs^2, representing the error. If an error of $100\,\mathrm{fs}^2$ over the spectrum is permissible in one iteration and the amplitude is $a = 10\,\mathrm{rad}$, the modulation frequency should be smaller than $b \leq 9\,\mathrm{fs}$.

for a and b are higher than usual. If this fourth order error does not exist, for example in spectrally resolved chirp scans, the problem of the second-order phase approximation persists, though it is less severe.

The case of improved MIIPS circumvents both these problems and retrieves the correct phase profile.

Chapter 3

Non-linear optics of Graphene

3.1 Introduction

The linear dispersion of the massless Dirac Fermions in graphene is enabling an ever increasing number of optical and optoelectronic applications [22, 23, 32, 33]. The resulting spectrally flat absorption in combination with ultrahigh electric switching rates makes graphene particularly interesting for high-speed applications in photodetectors [30, 31, 32] and as broadband saturable absorbers in ultrafast lasers [23, 72]. However, the linear dispersion is also connected to efficient higher-order optical responses, including non-linear broadband photoluminescence and four-wave mixing (FWM) [73, 74, 75, 76].

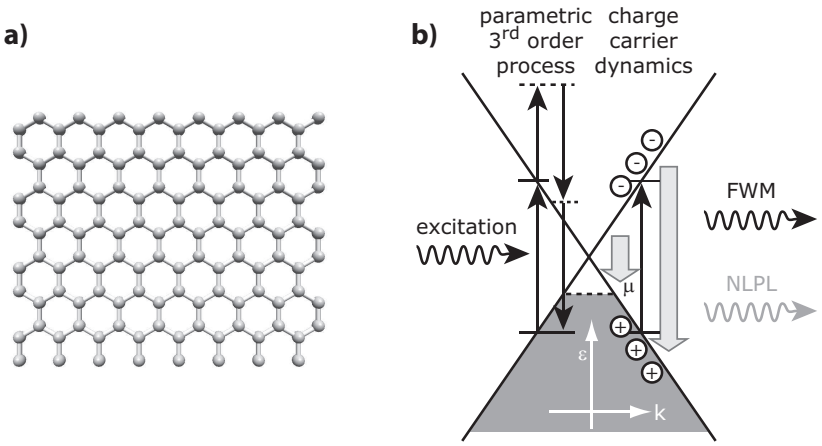

Figure 3.1: (a) Atomic structure of graphene, (b) simplified band structure near the K-point. Pulsed optical excitation of graphene causes two different non-linear optical effects: the parametric process of four-wave mixing (FWM) and non-linear photoluminescence (NLPL) which is driven by nonequilibrium charge-carrier dynamics.

Two very different non-linear processes are stimulated under femtosecond laser excitation. The first is instantaneous four-wave mixing which is a parametric third-order non-linear effect [75]. The second originates from the large density of charge carriers that

can be created during pulsed excitation. There are electrons lifted from the valence to the conduction band, leaving holes back in the valence band. The dynamics of these charge carriers lead to a non-linear, broadened light emission; the non-linear photoluminescence (NLPL) [73]. Fig. 3.1 presents a simplified schematic of the linear band structure near the K-point summarizing the two effects of four-wave mixing and non-linear photoluminescence.

In the first part of this chapter, sect. 3.2, the efforts of this work to better understand the properties of the third-order susceptibility of graphene are presented. The detected near-degenerate four-wave mixing is used as a reference signal for phase characterization. In the second part of this chapter, sect. 3.3, the non-linear photoluminescence is studied. Joint theoretical-experimental work is presented that helps to understand the origin and magnitude of the charge-carrier driven NLPL. Two-pulse correlation experiments then complete the picture by investigating phonon driven cooling processes, whose velocity is found to depend on the chemical potential μ.

3.2 Graphene's near-degenerate four-wave mixing for femtosecond pulse characterization

The following section is based on the publication: "Graphene Near-Degenerate Four-Wave Mixing for Phase Characterization of Broadband Pulses in Ultrafast Microscopy" in Nano Letters (2015), by Ciesielski et al. [77], reproducing parts of the text and figures.

3.2.1 Theoretical background: Third-order non-linear susceptibility of graphene

In 2010, Hendry et al. experimentally demonstrated non-degenerate four-wave mixing in graphene at the frequency $\omega_{FWM} = 2\omega_1 - \omega_2$ [75], an effect that in theory had already been predicted and described by Mikhailov [74]. The third-order nonlinearity of graphene is large; the non-linear susceptibility $\chi^{(3)}$ was observed to be 2 orders of magnitude higher than for thin gold films of comparable absorptivity [78], which is explained by the fact that all vertical transitions are resonant at all frequencies ω_{FWM}, ω_1 and ω_2 [75].

A simplified description of the non-linear response (Mikhailov [74]) is given in the following. Free charge carriers near the K-point in graphene possess the well known linear energy spectrum given by:

$$\varepsilon = (-1)^l \cdot V \cdot |\mathbf{p}| = (-1)^l \cdot V \cdot \sqrt{p_x^2 + p_y^2}. \tag{3.1}$$

Here the graphene sheet is oriented in the x-y plane, V is the Fermi velocity of about 10^6 m/s, $\mathbf{p}$ is the quasi-momentum, and l is determined by the particle type, namely $l = 1$ in case of a hole and $l = 2$ in case of an electron. If a sinusoidal (in plane polarized) electric field $\mathbf{E} = \mathbf{E}_0 \cdot \cos(\omega t)$ is applied to graphene, then according to Newton's equation of motion, the force $\mathbf{F}$ on the charge carriers with charge q is given by:

$$\mathbf{F} = \frac{d\mathbf{p}}{dt} = q \cdot \mathbf{E}. \tag{3.2}$$

Magnetic interactions are neglected here due to the large resulting mismatch in the magnitude of the resulting forces. Assuming an x-polarized electric field, the integration over time yields an expression for the momentum: $p_x = q \cdot E_0/\omega \cdot \sin(\omega t)$. From this, the time dependent charge carrier velocity under continuous wave illumination can be calculated from Hamiltonian mechanics:

$$v_x = \frac{\partial \varepsilon}{\partial p_x} = V \frac{p_x}{\sqrt{p_x^2 + p_y^2}} \overset{p_y \to 0}{=} V \cdot \mathrm{sgn}\big(p_x\big) = V \cdot \mathrm{sgn}\big(\sin(\omega t)\big). \tag{3.3}$$

The resulting ac electric current $j_x(t) \propto v_x(t)$ is strongly anharmonic and in the limit of $|\mathrm{p}| \approx p_x$, it is proportional to the signum function of the excitation field, so it flips between positive and negative current at optical frequencies and resembles a square wave. The

Fourier series of the resulting square wave current, with n being the charge carrier density per unit area, reads:

$$\begin{aligned} j_x(t) &= qnV \cdot \mathrm{sgn}\big(\sin(\omega t)\big) \\ &= qnV\frac{4}{\pi} \cdot \Big(\sin(\omega t) + \frac{1}{3}\sin(3\omega t) + \frac{1}{5}\sin(5\omega t) + \dots\Big). \end{aligned} \tag{3.4}$$

Apparently, the current has strong contributions of the electric field's odd orders (ω, 3ω, 5ω, ...), which lead to strong non-linear susceptibilities of odd orders. The third-order susceptibility $\chi^{(3)}$ therefore plays an important role in the optical non-linear spectrum of graphene, which can be seen as a direct consequence of the linear band structure near the K-point.

The presented approach illustrates the basic physical origin of the nonlinearity in graphene, but it represents a highly simplified description. Taking into account the Fermi distribution of electrons and holes as well as the tight binding model, one arrives at a more precise description of the coherent non-linear phenomena in graphene [74, 79, 80, 81], which also provide quantitative predictions.

3.2.2 Near-degenerate four-wave mixing spectra of graphene

As a parametric process, four-wave mixing has several realizations fulfilling energy conservation [82]:

$$\omega_{FWM} = |\pm\omega_1 \pm \omega_2 \pm \omega_3|, \tag{3.5}$$

where ω_i are the input optical frequencies. Typically, one can distinguish a degenerate and a non-degenerate case, where $\omega_{FWM}^{degenerate}$ equals one of the three input frequencies and $\omega_{FWM}^{non-degenerate}$ is different from all of them [82, 75]. In the case of a broadband laser, frequency mixing terms across the spectrum become important and lead to significant contributions directly next to the laser spectrum, defining the *near degenerate* (ND) case [82, 83].

Fig. 3.2a plots the single layer graphene emission spectrum (black symbols), excited by a 15 fs laser pulse centered at 1.55 eV (grey line) in the focus of a high NA=1.3 objective. On both sides of the excitation pulse an intense signal is seen, decaying rapidly with increasing energy shift. In the following, measurements are presented which verify that the signal indeed results from near-degenerate four-wave mixing, maximized for the shortest (bandwidth limited) laser pulse. Using either the low or the high energy side of the emission as a signal for an intensity map, high contrast confocal images of graphene are recorded as shown in fig. 3.2c. The signal on the detector reaches several million counts per second at a laser pulse energy of 5.4 pJ. Therefore, it is easily detected, and in combination with the weak background, stemming probably from the immersion oil and the glass substrate, near-degenerate four-wave mixing provides a very clear signal-to-background contrast, accompanied by a high signal-to-noise ratio.

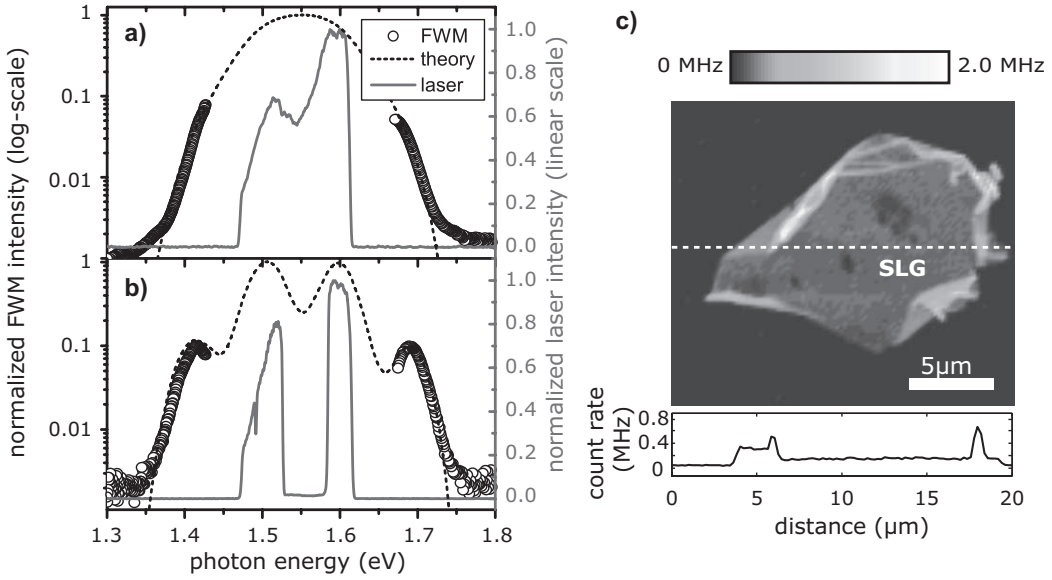

Figure 3.2: (a) Near-degenerate four-wave mixing (ND-FWM) spectrum of single layer graphene (SLG) on glass (semi-log plot). The laser pulse is transform limited in the focus of the objective. The dashed line corresponds to the calculated FWM-spectrum on the basis of a flat spectral amplitude and phase response and the spectrum of the incident laser. (b) The ND-FWM signal originating from a tailored excitation spectrum follows the theoretical prediction. (c) Confocal scan (Stokes side) of SLG on glass. ND-FWM provides a nearly background free signal contrast that highlights features such as wrinkles. The dashed line indicates the position of the cross section. *Adapted from Ciesielski et al.* [77]

Four-wave mixing spectra can be calculated according to the following integral [82]:

$$I^{FWM}(\omega) = c\varepsilon_0 \Big| \chi^{(3)} \int_{\omega_{min}}^{\omega_{max}} d\Omega_1 \int_{\omega_{min}}^{\omega_{max}} d\Omega_2 \quad E(\Omega_1) \cdot E(\Omega_2) \times \\ \times E(\Omega_1 + \Omega_2 - \omega) \cdot e^{i\cdot(\varphi(\Omega_1)+\varphi(\Omega_2)-\varphi(\Omega_1+\Omega_2-\omega))} \Big|^2 \tag{3.6}$$

where $\chi^{(3)}$ is the constant third-order susceptibility, E is the amplitude of the excitation laser field, c the speed of light, ε_0 the vacuum permittivity, ω_{min} and ω_{max} are the lower and upper frequency limits of the laser spectrum, and $\varphi(\omega)$ is the spectral phase of the pulse. This model description is in very good agreement with the experimental response, as seen in fig. 3.2a and b. At energies further away from the excitation, the experimental signal exceeds the theoretical curve, which is attributed to non-linear photoluminescence [73, 84, 85], c.f. sect. 3.3. This contribution is at least two orders of magnitude lower than the four-wave mixing signal.

The total emitted four-wave mixing energy per incoming pulse for the present measurement is determined in two steps. First, the calculated FWM spectrum (dashed line in

fig.3.2a) is scaled to the measured intensity, taking into account the overall detection sensitivity of the setup. This allows access to the FWM intensity also in the non-measurable regime covered by the laser pulse. Integrating the scaled spectrum, the full FWM energy per pulse of 10^{-17} J is obtained, corresponding to the spectral integral over eq. 3.6. From this, a value of:

$$\chi^{(3)}_{Graphene} = 4.3 \times 10^{-6}\,\text{esu} \tag{3.7}$$

is determined for the non-linear susceptibility at a central energy of 1.55 eV. This result is in general agreement with the value of $\chi^{(3)} = 1.5 \times 10^{-7}$ esu reported by Hendry et al. [75], while the deviation could result from the tight focusing of the excitation pulse in the present measurement, in combination with the nonlinearity of the signal[1].

The case of two spectrally separated excitation pulses $E_1(\omega)$ and $E_2(\omega)$ is implemented in fig. 3.2b. Here *intra*pulse frequency mixing within E_1 and E_2 does not contribute to the detected four-wave mixing signal. Only signal from *inter*pulse mixing following $\omega^{non-degenerate}_{FWM} = 2\omega_1 - \omega_2$ are observed with $\omega_2 > \omega_1$, where ω_1 and ω_2 are the central frequencies of the two pulses. In this case eq. 3.6 simplifies to:

$$I^{FWM}_{non-deg.}(\omega_S) = c\varepsilon_0 \left| \chi^{(3)} \int_{\omega_{min}}^{\omega_{max}} d\Omega \quad E_1^2(\Omega) \cdot E_2(2\cdot\Omega - \omega_S) \cdot e^{i(2\cdot\varphi(\Omega) - \varphi(2\cdot\Omega - \omega_S))} \right|^2 \tag{3.8}$$

for the Stokes side (Anti-Stokes correspondingly). Again, a very good agreement between the parameter-free calculation, assuming a spectrally constant $\chi^{(3)}$ response, and the experimental spectrum is found, as shown in fig. 3.2b.

The power dependence of the ND-FWM signal can be readily verified using amplitude pulse shaping. For the Stokes side, the dependence on the input power is quadratic for $I_1 \propto |E_1|^2$ and linear for $I_2 \propto |E_2|^2$ and vice versa for the Anti-Stokes side. The four resulting power laws are confirmed on single layer graphene as shown in fig. 3.3a.

Additionally, it is possible to verify the FWM origin of the signal within the probed range directly by scanning the frequency spacing between the central frequencies of the individual pulses using amplitude shaping, shown in fig. 3.3b. The dependence of the input frequencies and of the input power as well as the good agreement with the theoretical curves for different spectral pulse shapes confirms that the detected signal stems mainly from FWM with a spectrally flat amplitude response of $\chi^{(3)}$.

[1] Because of the tight focusing of fields and the resulting spatially nonuniform intensity, non-linear material constants are difficult to quantify in microscopic measurements. The reported value for $\chi^{(3)}$ represents the equivalent obtained for plane wave excitation with a circular diameter of 375 nm. While the individual characteristics of the components in the detection beam path are well-known, such as filter transmission and camera sensitivity, they add up to a total uncertainty of about an order of magnitude.

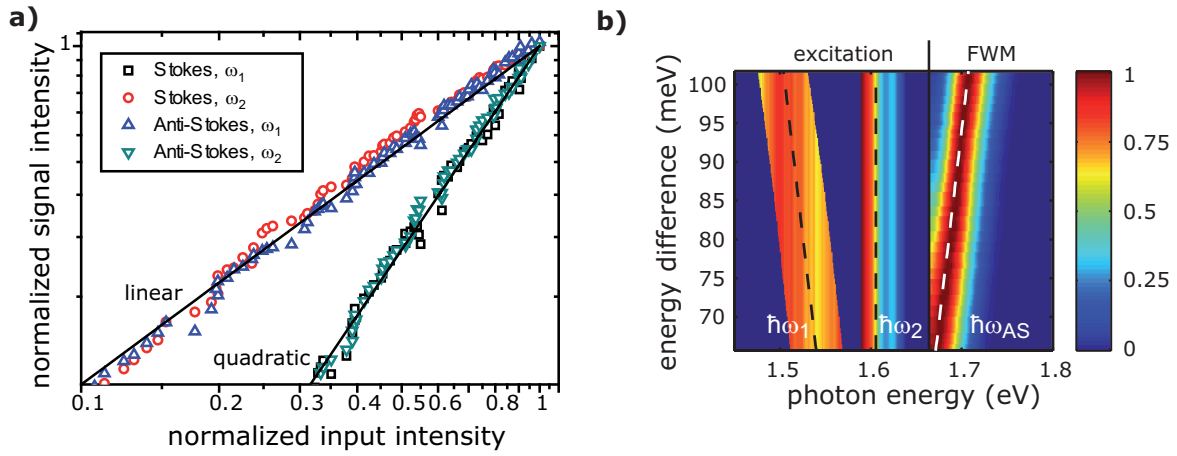

Figure 3.3: (a) Stokes and Anti-Stokes power dependence of the FWM signal. Two narrowband pulses are cut out of the full spectrum by the pulse shaper and individually varied in power. The measured power dependencies (symbols) match the theoretical curves (solid lines) in all four possible cases. (b) Control of FWM by scanning the energy difference between two pulses shifts the Anti-Stokes band (Stokes not shown). FWM are normalized to one, ω_1 and ω_2 are the center-of-mass frequencies of the individual pulses, the Anti-Stokes frequency follows: $\omega_{AS} = 2\omega_2 - \omega_1$. *Adapted from Ciesielski et al.* [77]

3.2.3 Experimental proof of a flat-phase response in the spectral region of 1.45...1.65 eV

A key requirement for broadband pulse characterization is a well-defined spectral phase response of the sample. To check for a phase dependence of the FWM signal in single layer graphene, chirp scans were performed. A well-defined chirp was applied to the pulse using the pulse shaper while monitoring the corresponding ND-FWM signal on the Stokes and anti-Stokes side. The resulting data shows a strong dependence of the FWM signal on the applied chirp, as can be seen in fig. 3.4. This is expected since adding chirp to a fem-

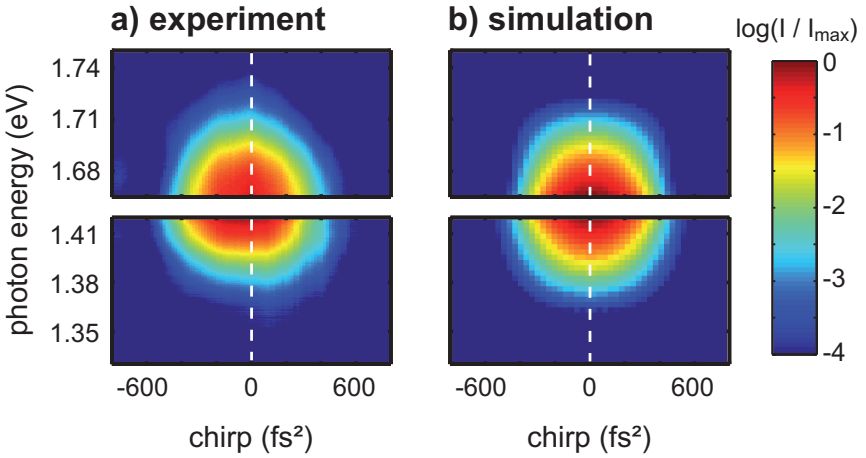

Figure 3.4: (a) Normalized SLG-FWM signal as a function of the chirp of the excitation laser pulse (logarithmic scale). The signal maximum is at $0\,\mathrm{fs}^2$, indicating that the material itself produces the highest signal for a pulse with flat phase. (b) Simulation on the basis of a flat phase $\chi^{(3)}$ following eq. 3.6. *Adapted from Ciesielski et al.* [77]

tosecond laser pulse leads to temporal broadening, decreasing the maximum field intensity. Importantly, the maximum FWM signal occurs for zero chirp for all photon energies. A shift of the whole pattern along the chirp axis would indicate a second-order phase dependence in $\chi^{(3)}$, as follows from eq. 3.6. The same applies to higher even polynomial orders, while higher odd orders would result in a non-symmetric shape of the pattern (a situation which is fully analogous to the second harmonic spectra in sect. 2.3.4). Thus it is concluded that the chirp dependence is only due to the associated time domain intensity variation and that the graphene phase response causes no additional chirp, i.e. is dispersionless in the probed spectral range. Fig. 3.4b plots the theoretical ND-FWM signal according to eq. 3.6. This agrees well with the experimental data in fig. 3.4a, further corroborating the claim of a flat phase $\chi^{(3)}$.

3.2.4 Discussion of the dispersionless third-order susceptibility

For the calculation of the theoretical FWM spectra upon broadband excitation (c.f. eq. 3.6) it was assumed that $\chi^{(3)}$ is constant within the laser bandwidth. In the following this assumption is discussed in more detail and from a theoretical point of view. For the special case of two discrete input frequencies $\omega_{FWM} = 2\omega_1 - \omega_2$ it was predicted that the amplitude of the third-order nonlinearity scales with ω^{-4} at optical frequencies [75, 74]. This dependency appears to be large at a first glance. Fig. 3.5 gives a comparison of the theoretical curves of fig. 3.2 with and without this spectral dependence. The difference between the predicted spectra is only minor and can experimentally not be distinguished.

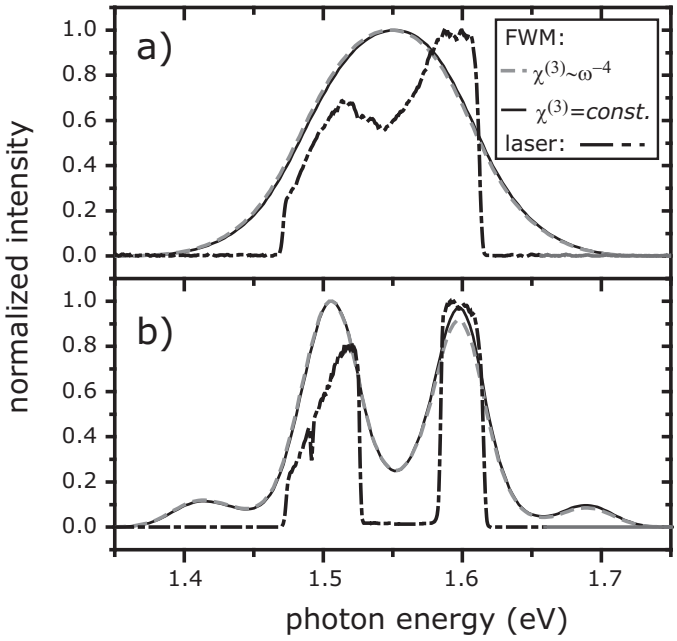

Figure 3.5: Comparison of theoretical FWM emission signals for two different models of $\chi^{(3)}$, analogous to fig. 3.2. (a) Calculation with the full laser spectrum, (b) calculation with two separate pulses. The differences are very small in both cases. *Adapted from Ciesielski et al.* [77]

While an analytical description has not yet been developed for FWM in the general case of three independent input frequencies as noted above, a corresponding model has been presented for the related phenomenon of third harmonic generation (THG) by Mikhailov [80]. Fig. 3.6 shows the spectral dependence of the third order nonlinearity in the relevant spectral range according to the full theory for THG. Within the considered spectral range, THG nearly scales with ω^{-4} comparable to FWM in the case of two discrete frequencies. It is thus anticipated that FWM will follow a similar scaling behavior also in the general case of three independent input frequencies. The expected error made by assuming a spectrally constant $\chi^{(3)}$ within the laser bandwidth will thus be on the order of the differences seen

between the solid and the dashed lines in fig. 3.5.

It has to be noted here that the optical nonlinearity of the THG theory [80] is a complex valued function that carries a phase dependence. Its magnitude depends crucially on the chemical potential and the observed spectral range. Therefore the second derivative of the predicted phase is compared to the sensitivity of the used setup.

The expected influence on the second-order phase is below $1\,\mathrm{fs}^2$ as seen from the inset in fig. 3.6. This is well below our detection threshold of approximately $10\,\mathrm{fs}^2$. In terms of pulse length, a 15.00 fs laser pulse at 1.55 eV would experience a temporal broadening to 15.07 fs by an additional (constant) second order phase of $1\,\mathrm{fs}^2$. The used approximation of zero spectral phase of the third-order nonlinearity is therefore also theoretically well justified.

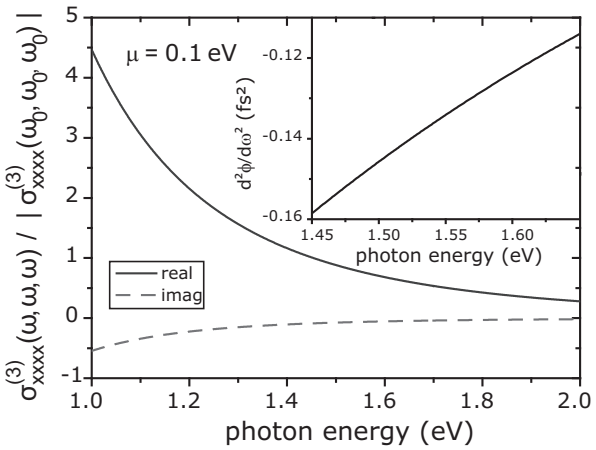

Figure 3.6: Diagonal tensor element of the non-linear optical conductivity $\sigma^{(3)}_{xxxx}$ for the case of third harmonic generation (c.f. Eqs. 10–12 in Ref. [80]). A typical chemical potential of 0.1 eV was chosen, the scattering parameter γ is set to zero because it does not exert any influence at the current energy range. The data was normalized to the amplitude at an energy of $\hbar\omega_0 = 1.55\,\mathrm{eV}$. (Inset) The second derivative of the phase of $\sigma^{(3)}$ is very small compared to the sensitivity of the measurements. *Adapted from Ciesielski et al.* [77]

3.2.5 Application to pulse compression

Having established that the third-order susceptibility of graphene is spectrally homogeneous and dispersionless, it is possible to utilize the signal for temporal pulse characterization as presented in sect. 2.3.2 for the case of second harmonic light. Again, the shortest (bandwidth limited, flat-phase) pulse produces the highest non-linear signal. In this scheme, the ND-FWM signal for a laser pulse of unknown phase is maximized by varying the spectral phase profile of the pulse using the pulse shaper. In a first step, the ND-FWM signal is detected while scanning the linear and quadratic chirp in a polynomial phase scan, analogous to the SH on page 20. The peak phase is then used as the starting point for the following procedure.

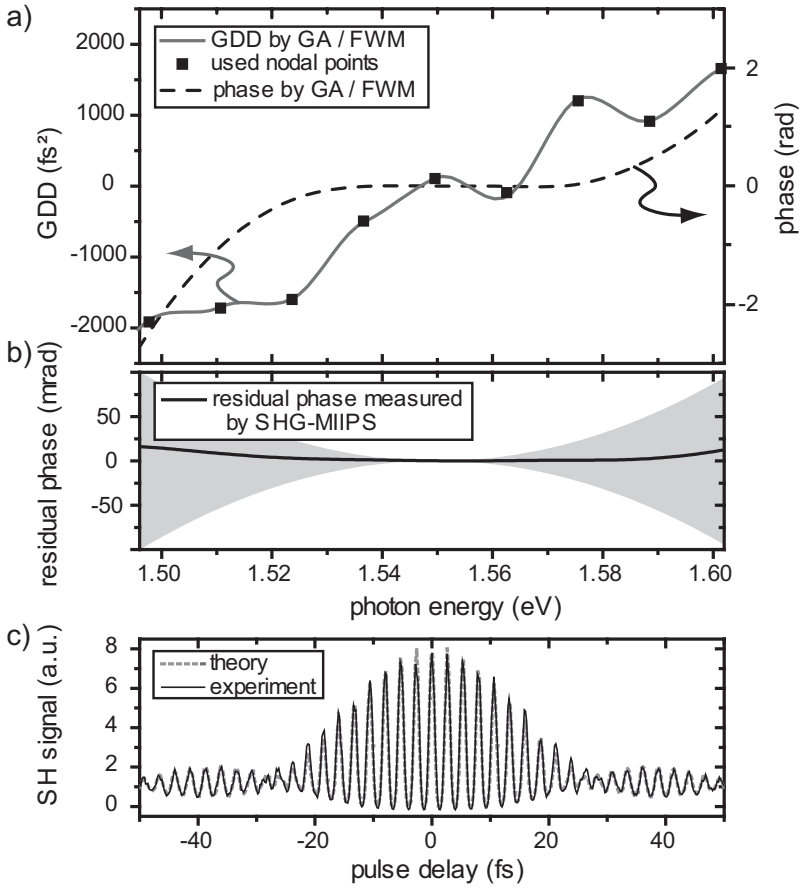

Figure 3.7: Demonstration of pulse compression using a genetic algorithm (GA) to maximize the ND-FWM signal on the Anti-Stokes side of the laser. (a) Reconstructed group delay dispersion (GDD) of the pulse, approximated by cubic interpolation between 9 nodal points (black symbols), used as free parameters for the optimization. (b) Residual phase measured by MIIPS from second harmonic generation (SHG) on $Fe_2(IO_3)_3$ nanocrystals. The gray area is a conservative estimate on the error. (c) Second harmonic generation auto-correlation with the phase correction of fig. a shows very good agreement with the theoretical curve obtained from the input spectrum. *Adapted from Ciesielski et al.* [77]

Final reconstruction of the phase, or more precisely its second derivative, is achieved by maximizing the ND-FWM signal using a genetic algorithm [86] as introduced on page 20. The second-order phase is varied at 9 nodal points over the spectrum, while the parts in between are approximated by cubic interpolation. The number of parameters for the genetic algorithm is therefore 9, allowing for a rapid convergence, typically within 10 to 20 generations. The actual phase applied to the pulse shaper is calculated by double integration with arbitrary integration constants as usual. At the end of this procedure, the laser has reached its bandwidth limit.

After compressing the pulse by maximizing the ND-FWM signal, the result is verified by measuring the residual phase with MIIPS [6], using the second harmonic of a reference sample of $Fe_2(IO_3)_3$ nanocrystals, detected in the same microscope. Fig. 3.7b demonstrates that there is only a very small residual phase at the detection limit of the system. An interferometric second harmonic autocorrelation scan further verifies that the pulse is bandwidth limited after compression (fig. 3.7c). This demonstrates the feasibility of phase characterization using the near-degenerate four-wave mixing signal from single layer graphene.

From a materials perspective, graphene has several advantages. Its sub-nm thickness provides the optimum focus definition, which is particularly relevant for microscopy applications. In contrast, for other materials such as beta barium borate (BBO) or iron(III) iodate ($Fe_2(IO_3)_3$) nanocrystals, the size is typically on the order of several tens of nanometers, adding uncertainty to the focal position and depth (c.f. the electron micrograph in fig. A.1 in the appendix). In the worst case, this can include propagation effects in the non-linear response, causing erroneous phase corrections. The lateral position and beam quality on the other hand cannot be juged from the presented approach with the spatially extended graphene sheets. At the same time, the graphene four-wave mixing is an extremely efficient process leading to easily detectable signals that reach photon count rates of several millions per second. Most importantly, its spectrally uniform response should allow for phase characterization of laser pulses reaching from the THz to the visible regime.

Near-degenerate FWM avoids drawbacks of schemes relying on higher harmonic detection and the associated requirements regarding the achromaticity and the large spectral detection range as discussed in the following. This could be particularly useful for pulses in the visible spectral range and for ultra-broadband pulses, where optics come to a limit if second harmonic generation is used as a feedback. Moreover, near-degenerate FWM at a given detection frequency contains the contribution of a broad range of input frequencies following eqn. 3.6. The ND-FWM signal is maximized under the condition that:

$$\varphi(\Omega_1) + \varphi(\Omega_2) - \varphi(\Omega_1 + \Omega_2 - \omega) = 0 \tag{3.9}$$

for all combinations of Ω_1 and Ω_2 covered by the input laser spectrum. This condition is notably different from the one for maximum SHG in eg. 2.28, which was defined locally and could be satisfied for a local frequency ω. Eq. 3.9 is true for a flat spectral phase profile only, and in the limits of $\omega \approx \omega_{min}$ or $\omega \approx \omega_{max}$ all spectral components contribute at once. As a consequence, no spectrometer is required for phase characterization when using a spectrally

integrated signal that ranges sufficiently close to the excitation spectrum[2]. A drawback of intensity based pulse measurements is that there is no subsistent feedback on the quality of the retrieved phase. If such feedback is needed, the peak position and symmetry of a spectrally resolved chirp scan as in fig. 3.4 can be used as well as a comparison of the ND-FWM spectrum with the theoretical spectrum.

It is noted that for ultra-broadband pulses exceeding $1600\,\mathrm{cm}^{-1}$ of bandwidth, non-linear Raman scattering from the G mode in graphene could contribute to the detected signal. In this case the procedure could be modified, e.g. the spectrum could be compressed step-wise by limiting the bandwidth.

It is also noted that other pulse characterization procedures based on FWM have been presented, e.g. in combination with an additional gate pulse [65] or spectral detection analogous to FROG [87]. Compared to these procedures the presented approach based on graphene's near-degenerate four-wave mixing appears to be simpler and more easily implemented.

[2]On the other hand, no spectrum-based algorithm as MIIPS is possible.

3.3 Non-linear charge carrier dynamics in graphene, excited in the sub 20 fs regime

Optical excitation of graphene efficiently creates electrons and holes in the conduction and valence band, respectively. Due to their high peak intensity, pulsed lasers can generate a non-equilibrium charge carrier distribution which is followed by subsequent scattering of the charge carriers along the Dirac cone and by carrier multiplication [29, 88]. The resulting broadening of the bath of excited electrons and holes leads to a spectrally broad light emission which is super-linear with the excitation intensity. Microscopically, this non-linear photoluminescence (NLPL) has two different origins, one connected to the rapid dynamics of charge carrier thermalization and one connected to the slower, phonon mediated carrier cooling. For very broad laser spectra, the high third-order optical susceptibility of graphene creates additional four-wave mixing contributions to the total emitted signal [75, 77] (see sect.3.2). Different from NLPL, the third-order process is parametric [74].

So far the ultrafast dynamics in graphene have been studied both experimentally and theoretically using different techniques such as optical pump-probe spectroscopy [28, 29], time-resolved photoelectron spectroscopy [89] or photoluminescence studies [26, 27, 90]. There are only a few optical studies on the timescale below 20 fs [28, 29, 85]. Apart from the microscopic description of charge carrier dynamics and light-matter interaction based on the density matrix formalism [91], a phenomenological description of the hot electron dynamics by a two temperature model has successfully been used [26]. From pump-probe studies it is known that this model holds for laser pulses in the visible as short as 10 fs [28, 29]. As will be shown, this is not true for the full spectrum of the emission.

Here, an experimental discrimination between the coherent and the incoherent non-linear photoluminescence is presented (sect.3.3.1), followed by a broadband overview over the non-linear spectrum of graphene (sect. 3.3.2) and finalized by detailed, time-resolved studies of the dynamics of the incoherent part (sect. 3.3.3).

3.3.1 Coherent and incoherent non-linear photoluminescence

The following section is based on the publication "Microscopic view on the ultrafast photoluminescence from photoexcited graphene" in Nano Letters (2015), by Winzer et al. [85], reproducing theory and figures.

Within the theoretical framework of the semiconductor optical Bloch equations, the photophysics of graphene from the visible to the infrared are understood as follows [91]. In case of excitation with femtosecond laser pulses, the absorption of 2.3 % of the light intensity in the near infrared leads to a high number of charge carriers created in a femtosecond time span. The absorption is driven by the microscopic polarization p_k which has a distribution of the wave vectors k, initially reflecting the polarization of the optical excitation. The microscopic polarization itself gives rise to the substantial charge carrier

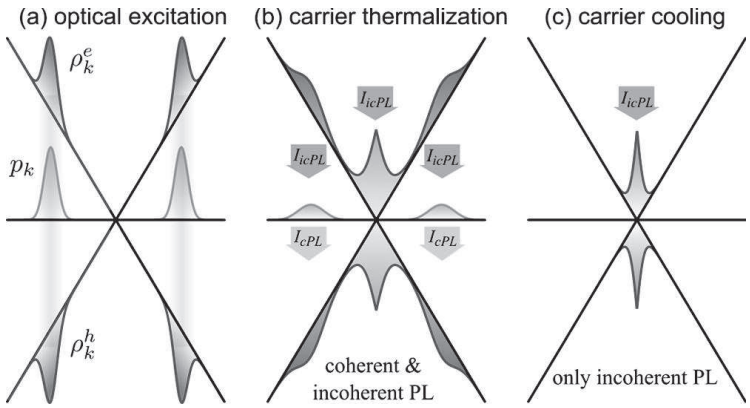

Figure 3.8: Schematic of the initial dynamics in optically excited graphene. (a) Optical excitation (shaded area) creates a microscopic polarization p_k and a carrier distribution $\rho_k^{e/h}$. (b) Carrier scattering towards the K-point and dephasing of p_k within the first tens of femtoseconds. (c) Carrier cooling on a picosecond timescale leads to a narrower distribution near the K-point. During the process, spontaneous carrier recombination leads to broadband and incoherent photoluminescence I_{icPL} while p_k induces a coherent photoluminescence I_{cPL}, centered at the laser energy. *Adapted from Winzer et al.* [85]

population $\rho_k^{e/h}$ of electrons e and holes h. The laser created population is not in thermal equilibrium and its initial dynamics are dominated by Coulomb-induced carrier-carrier scattering events, which drives the carrier distribution towards the Dirac point and breaks up the inital structure in momentum space, as shown schematically in fig. 3.8. On a femtosecond timescale, this leads to a thermalized, hot carrier distribution without a preferred directionality in k-space. The total absorbed energy plays a crucial role for the distribution of hot carriers, which can exceed the laser central energy substantially. Once the hot state is reached and the microscopic polarization has undergone complete dephasing, the dynamics slow down. On a picosecond timescale, the carrier distribution cools down and finally disappears.

During the process, two different effects cause light emission: first, the oscillating microscopic polarization p_k, which is the solid state analog to the oscillating dipole moment of a two-level system, induces radiation. This is called the *coherent* photoluminescence I_{cPL}, and its coherence stems from the fact that it is driven by the oscillations of the microscopic polarization which carry "memory" of the exciting laser field. For the same reason, it is spectrally centered around the laser excitation, although it exceeds it for both higher and lower energies. The second effect is spontaneous carrier recombination, whose magnitude is only driven by the (time dependent) carrier distribution. This is the *incoherent* photoluminescence contribution I_{icPL}, which is independent of the initial phase and temporal shape of the laser but mainly depends on the deposited energy. Both sources of radiation have a distinct temporal behavior which is bound to the dynamics of charge carriers and the microscopic polarization. In a measurement, it is at the moment impossible to observe

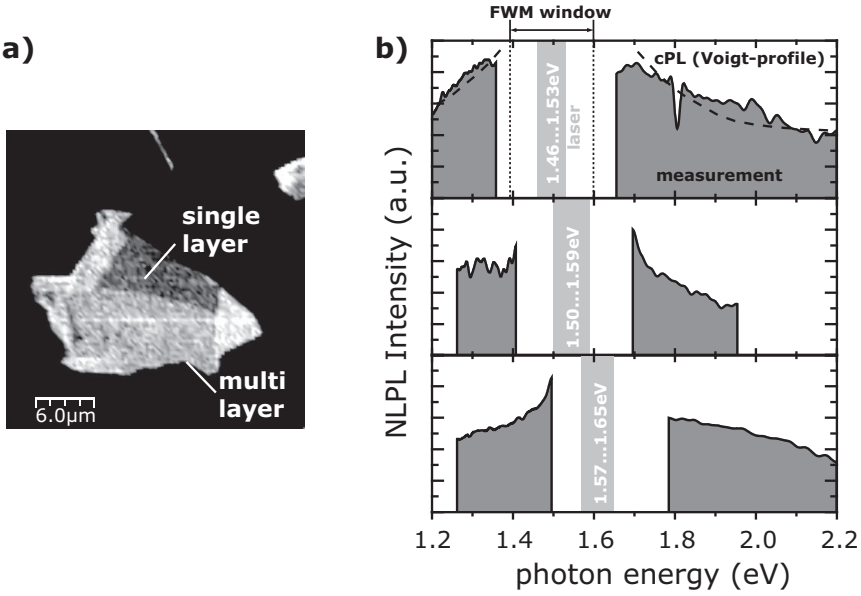

Figure 3.9: (a) Confocal PL scan of a graphene flake on glass detecting the emission between 1.2 eV and 1.3 eV under excitation with the full laser spectrum, centered at 1.55 eV. (b) Measurements of the NLPL on single layer graphene at different laser central energies. The four-wave mixing (FWM) regime is cut out by spectral filters. A feature towards the laser central energy is visible that follows the excitation. *Adapted from Winzer et al.* [85]

these dynamics because the signal detection is time integrated, such that it is proportional to the total emitted light intensity.

Experimentally, there are two hallmarks of the coherent and incoherent PL, which can be used to discriminate between them. The spectrum of the coherent PL has to follow the laser central energy. The spectrum of the incoherent PL on the other hand, is only influenced by the irradiated laser fluence. The spectrum of the incoherent contribution is known to be broadband and independent of the laser central energy since 2010 [26, 90], but the existence of the coherent part, predicted by theory [88, 91], was first demonstrated during this work on the basis of the following measurements [85].

Here, the non-linear photoluminescence of single layer graphene for three different laser central energies was measured by restricting the laser spectrum with long and shortpass filters. All measurements were carried out at the maximum permissible fluence that did not visibly damage the flakes ($\leq 320\,\mu J/cm^2$). The pulses, used for these experiments, had a bandwidth of about 0.08 eV (50 nm) which corresponds to a pulse length of about 40 fs. All spectra were background corrected on glass near the graphene flake and restricted to a spectral range excluding four-wave mixing[3]. The results in fig. 3.9 show the shoulders of a PL feature following the laser central energy. In fig. 3.9b, this feature is fitted with a Voigt profile as a visual guide for one spectrum. Below the coherent PL, there is a

[3]If the laser spectrum reaches from ω_1 to ω_2, FWM is excluded in regions of $\omega < 2\omega_1 - \omega_2$ and $\omega > 2\omega_2 - \omega_1$, see sect. 3.2.

broad part that extends up to 2.2 eV and further, which is attributed to the incoherent PL in the current situation. The coherent PL is unfortunately strongest, where it cannot be measured. This occurs at the laser central energy and closest to it, where it interferes with four-wave mixing. The only parts left within the detectable range are therefore the smaller shoulders, seen in fig. 3.9b and highlighted by the Voigt profile. Fig. 3.10 presents

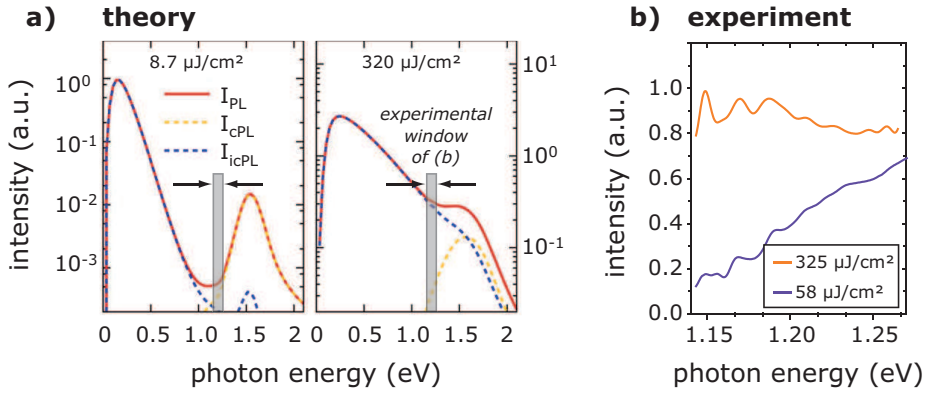

Figure 3.10: Comparison of the high power and low power regime for the influence of the incoherent PL (no FWM included). (a) Theory, gray area shows the detection window of the experiment: (b) incoherent PL on a glass substrate. *Adapted from Winzer et al.* [85]

a joint theoretical and experimental comparison of incoherent and coherent PL under different excitation fluences. In the low fluence regime, amounting to 8.7 μJ/cm^2 for the theory, and 58 μJ/cm^2 for the measurement, the total emitted incoherent PL is reduced to a minimum in the visible and near infrared region (blue dashed lines in fig. 3.10a). The charge carriers scatter towards the Dirac point and loose the majority of their energy before they recombine and emit light, whose photon energy then lies below 1 eV. In the high power regime of 320 μJ/cm^2, the total emitted light intensity is higher and extends much more into the visible spectral range, almost until 2 eV. As a consequence, the region of 1.15 . . . 1.25 eV was chosen here for detection while exciting with the full laser spectrum of 1.46 eV to 1.65 eV. Within this region, coherent PL is basically absent and the effect on the incoherent PL can be studied. Fig. 3.10b gives the comparison of low and high power regime in this spectral window. It clearly shows a strong increase of the detected incoherent PL with increasing laser power, as expected from the theory in fig. 3.10a. From comparison with the measurements in fig. 3.9, a substantial background of coherent PL can be excluded, leaving only the incoherent PL.

In summary, a joint theory-experiment study on the ultrafast photoluminescence in photoexcited graphene was able to identify a coherent contribution to the photoluminescence. As opposed to the known, incoherent part, it is characterized by a clear shift with the excitation energy. Variation of the excitation power shows a strong effect of the incoherent PL, whose spectrum is predicted to move substantially towards the visible. These experimental findings corroborate the calculations by Winzer et al. [85], based on the semiconductor Bloch equations for graphene.

3.3.2 The non-linear spectrum of graphene under 15 fs pulsed laser excitation

Sections 3.3.2 and 3.3.3 are based on the publication (in prep.): "Ultrafast response and carrier dynamics in graphene probed by femtosecond pulse shaping microscopy" by Ciesielski et al. [92], reproducing text and figures.

In the previous section it was shown that the charge carrier driven non-linear photoluminescence of graphene consists of a coherent and an incoherent part. As the relative weight of both contributions depends on the pulse length and the excitation fluence, it is not always possible to clearly observe the coherent PL signal, which is often overlaid by four-wave mixing and the strong incoherent PL. Now, the optical response of graphene to a 15 fs excitation pulse, centered at 1.55 eV at a pump fluence of 100 μJ/cm^2 is shown in the semi-log plot of fig. 3.11.

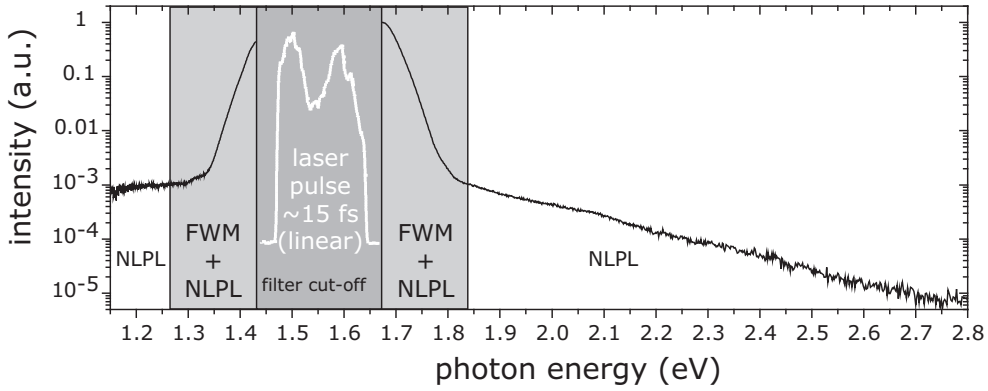

Figure 3.11: Ultrafast emission spectrum of single layer graphene upon excitation using a 15 fs bandwidth limited laser pulse showing two distinct types of emission on the Stokes and Anti-Stokes side: Near-degenerate four-wave mixing (ND-FWM) and non-linear photoluminescence (NLPL). *Adapted from Ciesielski et al. [92]*

We first note, that upon broadband excitation, graphene exhibits an extremely strong near-degenerate four-wave mixing signal (c.f. chapt. 3.2), occurring at frequencies ranging from $\omega_S = 2\omega_{L,min} - \omega_{L,max}$ (Stokes) to $\omega_{AS} = 2\omega_{L,max} - \omega_{L,min}$ (Anti-Stokes) [74, 75, 77] which is marked by the grey area in the plot. Here $\omega_{L,min} = 1.46\,\mathrm{eV}/\hbar$ and $\omega_{L,max} = 1.65\,\mathrm{eV}/\hbar$ denote the lower and upper frequency limits of the incident laser pulse spectrum, shown by the white solid line in a linear scale. The four-wave mixing signal rapidly decays for larger energy differences to the laser. In the measurable range, its emission intensity is three orders of magnitude larger than that of the other spectral contributions.

The second type of emission has its origin in the ultrafast photoluminescence of graphene [26, 27, 85, 90], which is, as discussed, mostly the incoherent PL in this case. The broad contribution extending into the blue and near-infrared spectral range originates from carrier recombination reflecting the carrier population density at the emission energy. Lui et al. [26] quantitatively described this contribution on the Anti-Stokes side upon excitation

with 30 fs pulses using a two-temperature model, which is simpler than the theoretical description based on the semiconductor Bloch equations. In this model the electronic system thermalizes quasi instantaneously upon pulsed excitation due to very efficient carrier-carrier scattering and can be described by a Fermi-Dirac distribution at all times. On a slightly longer time-scale of few tens of femtoseconds the electronic system equilibrates with strongly coupled optical phonons (SCOP). The non-linear PL then results from the hot electron distribution that emits as a black-body radiator with a temperature corresponding to the instantaneous temperature of the excited carriers[4]. For the pump fluence of 100 $\mu J/cm^2$ and a spectral width of 0.2 eV used in the experiments of this and the following section, coherent PL is the weakest contribution to the spectrum. Therefore it is neglected in the following, sticking to the simpler description of the incoherent PL, based on the two temperature model. An important parameter of this model is the total chemical potential of graphene, which reflects doping [89]. In the present case, graphene is slightly p-doped from the substrate (see appendix A.2 for Raman spectroscopy), which is typical for such samples [93].

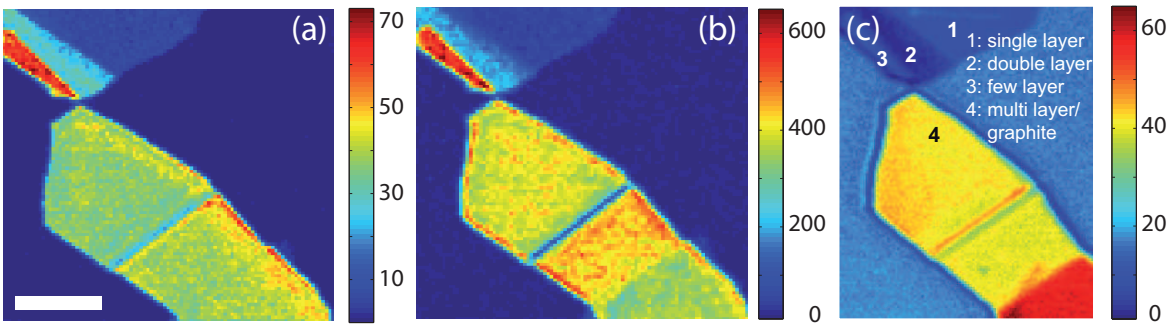

Figure 3.12: Confocal scan images of flakes with single layer graphene, multilayer graphene and graphite regions. The scale bar corresponds to 4 µm, colorbars indicate count rates in kHz. (a) NLPL detected between 1.31 and 1.24 eV. (b) ND-FWM signal detected at the Stokes side between 1.44 and 1.31 eV. (c) Elastic scattering image using a HeNe laser operating at 1.96 eV. *Adapted from Ciesielski et al. [92]*

Graphene can be readily observed in a confocal microscope by detecting the NLPL [26, 27, 90]. Since near-degenerate FWM is orders of magnitude stronger for the present pulse duration (see fig. 3.11), imaging of graphene and few layer graphene becomes even easier. A comparison between the image contrast obtained using NLPL and near-degenerate FWM and that of elastic scattering is shown in fig. 3.12. FWM and NLPL images are quite similar, since the intensity of both signals depends on the layer number. Different from the scattering image, we note that the highest signal stems from few layer graphene as opposed to multilayer graphene or graphite. If the layer number is too high (> 20), reabsorption limits the total emitted signal for NLPL, FWM, and Raman, while reflection still increases [84].

[4] Compared to the non-radiative decay channels via phonons, the radiative recombination rate of the charge carriers is small, so energy dissipation by radiation can be neglected.

3.3.3 Femtosecond correlation spectroscopy of graphene

Confocal detection allows us to probe the temporal response of the material in a spatially resolved fashion and to study its layer dependence. Autocorrelation measurements (or two-pulse correlation measurements) are a powerful tool to investigate the temporal behavior of non-linear signals. They can be performed in a collinear way using the pulse shaper and are implemented here in a degenerate pump-probe scheme by applying a cosine amplitude modulation at constant carrier envelope phase as presented in sect. 2.1.3. An energy resolved autocorrelation scan of the single layer graphene emission is presented in fig. 3.13a. In this image all spectra were normalized to their maximum value at zero delay. For all emission energies a rapid decay from overlapping to separated pulses is observed. The "temporal width" Δt is determined as a central outcome of the experiments, defined by the double standard deviation of the intensity of an autocorrelation scan. If $I(\omega, \tau_k)$ is the intensity measured for the pulse delay τ_k at the frequency ω, the temporal width is given by:

$$\Delta t(\omega) = 2 \cdot \sqrt{\frac{\sum_k \tau_k^2 \cdot I(\omega, \tau_k)}{\sum_k I(\omega, \tau_k)}}. \tag{3.10}$$

The average value of τ_k is zero by measurement definition. Since the signal does not vanish at the borders of the accessible measurement range, this range was kept constant from $-30\,\text{fs} \ldots +30\,\text{fs}$ in order to quantitatively compare the numbers. An alternative definition of the temporal width by the full-width-at-half-maximum gives a lower signal-to-noise ratio and depends on both the width and shape of the curve, which is why the double standard deviation was chosen here as a measure.

While the temporal width of the autocorrelation trace at higher photon energies around 2 eV is on the order of the actual pulse width, the traces become broader for lower emission energies of $\approx 1.2\,\text{eV}$. From 2.3 eV over 1.3 eV to 1.2 eV the temporal width monotonically increases from 22 fs to 32 fs for the parts that are not dominated by FWM. This observation reflects the charge carrier dynamics determining the incoherent non-linear PL as discussed below [26]. Apart from this general trend, there is a pronounced modulation in the temporal width near the laser excitation energy in the range that is dominated by near-degenerate FWM. This variation can be quantitatively described by an instantaneous third-order process and the spectrally flat third-order non-linear polarizability $\chi^{(3)}$ of graphene, as stated in sect. 3.

Measured spectrally resolved autocorrelation data is now modeled using FWM theory and the two-temperature model (TTM) formulated for graphene by Heinz et al. [26]. The model assumes that the electrons are in thermodynamical equilibrium at all times and that their distribution can as such be described by Fermi-Dirac statistics and an electron temperature. There is a single relaxation channel via strongly coupled optical phonons. The phonon distribution is described by Bose-Einstein statistics and a corresponding phonon temperature. The PL emission is finally modeled as black body radiation from the hot electrons. Figs. 3.13d–f illustrate the predictions of the TTM for two-pulse excitation for the present pulse duration and the physical parameters of graphene. The FWM signal is

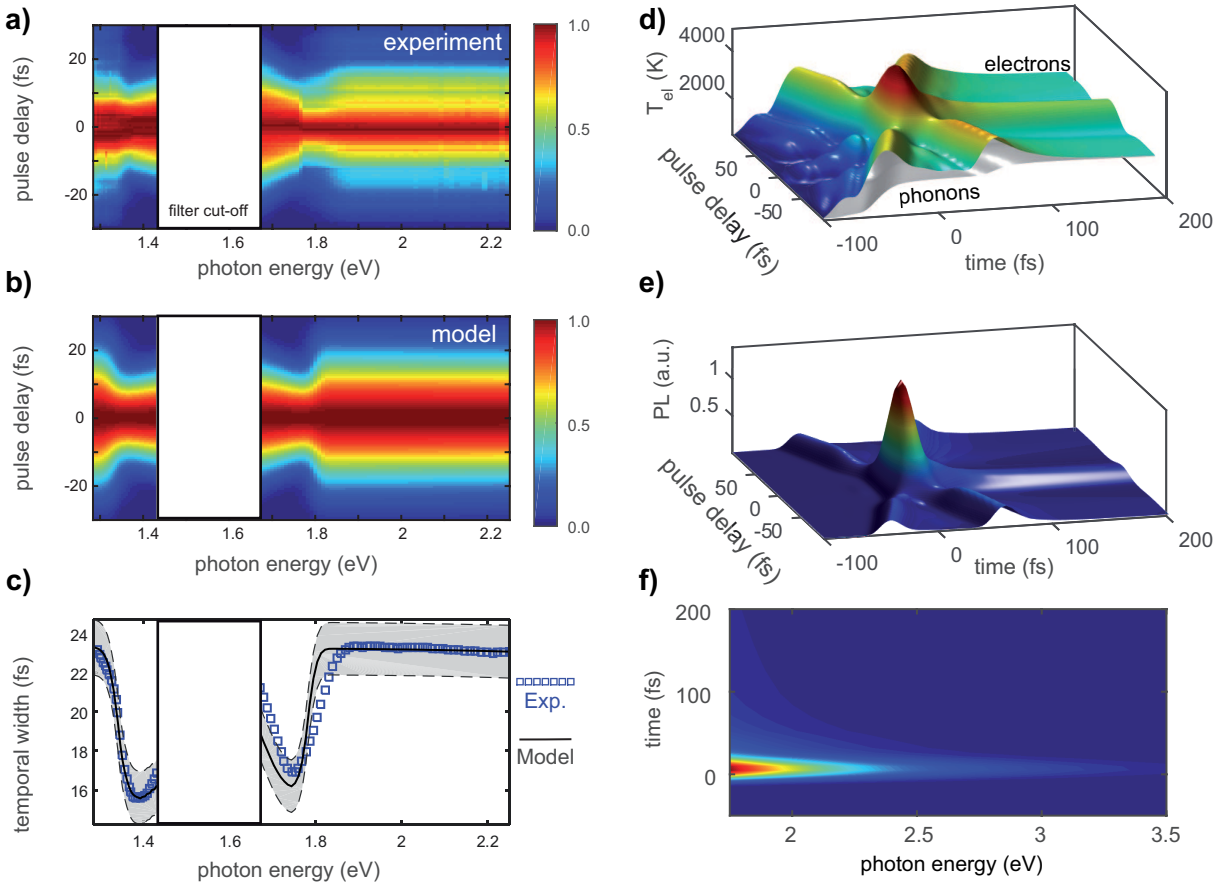

Figure 3.13: Spectrally resolved auto-correlation scan of single layer graphene. The spacing between two 15 fs laser pulses is varied while detecting the emitted light. (a) Experimental results and (b) theoretical results based on a two-temperature model and constant $\chi^{(3)}$. All spectra are normalized to their respective maximum at zero pulse delay. (c) Temporal width of the autocorrelation, as a function of emission energy, measured as the double standard deviation of the upper traces. (d) Instantaneous electron (colored) and phonon (grey) temperature as a function of pulse delay calculated using the two-temperature model. (e) Derived PL intensity detected between 1 eV and 3 eV. (f) Corresponding time-dependent non-linear PL emission spectra. *Adapted from Ciesielski et al. [92]*

calculated directly from the incident laser spectrum using the spectrally flat and dispersionless $\chi^{(3)}$ of graphene. The intensity ratio between FWM and PL is a fitting parameter. The full set of formulas used can be found in the appendix B.4.

Within the TTM, a high electronic temperature causes strong luminescence emission. Fig. 3.13d shows the electronic and phononic temperature for the autocorrelation experiment, calculated from the TTM on the basis of the laser spectrum. Clearly, the electrons reach a much higher temperature when the two pulses temporally overlap. These hot electrons cause luminescence according to the black body formula at every point in time, visualized in fig. 3.13e, whereas the PL spectrum for these times is given in 3.13f. It is here observed that the largest fraction of emission stems from the times with highest electron temperature. There are two parameters that determine this maximum electronic temperature, the total absorbed energy and the pulse length. At a given pulse energy, the PL can still show a substantially different total intensity and spectral position if the pulse length is varied, because the peak temperature differs.

The final fitting results are shown in fig. 3.13b. All features including the modulation of the signal in the near-degenerate FWM range are well reproduced. The derived temporal width follows the same trend as has been observed experimentally. The decrease of the temporal width with increasing detection energy can be understood based on fig. 3.13d, showing the electron and phonon temperatures throughout the autocorrelation measurement as well as the PL emission based on the TTM in 3.13e and f. While the electron distribution cools down, the emission peak shifts to lower energies. Hence, in the two-pulse correlation experiment at larger pulse delays, the excitation by the second pulse does not lead to an equally high temperature compared to the first one. The main PL contribution occurs within 50 fs and already a pulse separation of 30 fs reduces the total emitted signal by a factor of 5. For multi-layer graphene, spectrally resolved autocorrelation traces were recorded too (not shown). The autocorrelation traces show the same trend although at substantially decreased temporal width. This can be explained by changes in the chemical potential due to substrate induced doping (see below). Probably due to the stronger signal from multi layer graphene, the decrease of the temporal width towards higher emission energies is more clearly visible.

All ultrafast measurements presented up to now were performed at fixed sample positions in the focus of the confocal microscope. It is on the other hand also possible to perform the same sample characterization in an imaging mode, as will be shown. Successive confocal scans with different pulse separations were recorded while detecting only the non-linear PL on the Stokes side using a 980/20 nm bandpass filter. From 10 data points between 0 fs to 30 fs the temporal width of the PL autocorrelation can be extrapolated for every pixel, establishing an image which shows the response time of the non-linear PL at different positions. As presented in fig. 3.14a and b, the response time depends on the layer number in a negative correlation: the thicker the graphene, the narrower the autocorrelation's temporal width. For single layer graphene, a temporal width of 23 fs, for bilayer 19 fs, and for multi-layer graphene 16 fs can here be reported. The broad distribution observed for single layer graphene most likely reflects spatially heterogeneous substrate-induced doping which will have a smaller influence for thicker flakes due to dilution of defects.

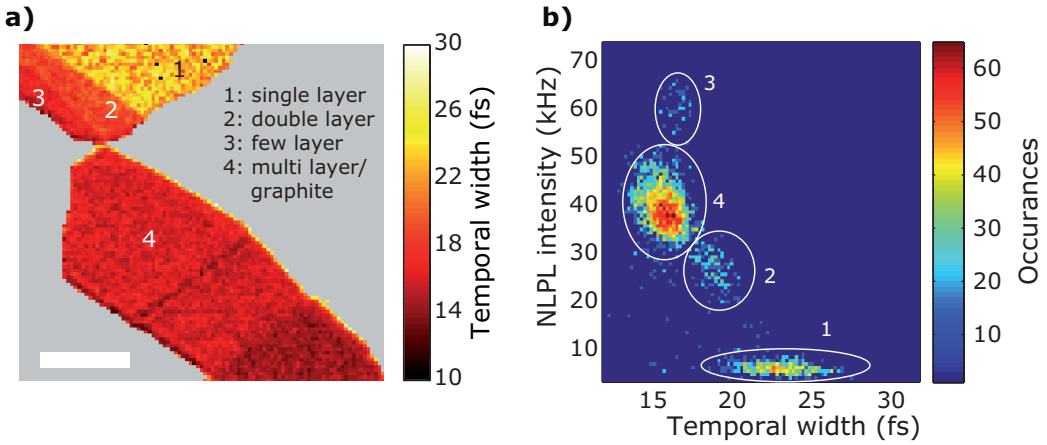

Figure 3.14: (a) Confocal scan of the temporal width of the NLPL at a photon energy of 1.27 eV. The gray area contains no graphene, scale bar is 4 µm. (b) The 2D correlation function of NLPL intensity (Fig. 3.12a)) vs. the temporal width of the auto-correlation shows a clear anti-correlation between the two quantities. Different parts of the plot can be identified with different positions at the sample, indicated by the numbers. The higher the sample, the shorter the temporal width. *Adapted from Ciesielski et al. [92]*

Using the two-temperature model, the different dynamics of single layer and few layer or multi layer graphene can to a certain extent be explained in terms of substrate-induced doping which enters the equations through the chemical potential. As can be seen from Raman spectra, substrate-induced doping of single layer graphene is larger than the average doping level of multi layer graphene (c.f. appendix A.2). Considering the corresponding shift in chemical potential μ in the two-temperature model leads to a change in the temporal width congruent to the experimentally observed trend. However, the large change observed in the experiment can not be reproduced within the TTM at reasonable values of μ. This result can be attributed to different electron dynamics for multi layer graphene and graphite as compared to single layer graphene which is not covered by the model. In particular, the density of states is changed and additional inter-layer relaxation channels for electrons and phonons exist as compared to single layer graphene.

For very high pulse energies it should be possible to saturate the electronic temperature as it is possible to saturate the absorption [72]. Due to the damage threshold of the graphene samples is use, this regime was not reached. In contrast to the presented results, Stöhr et al. [27] reported a very high luminescence yield at a pulse length of 7 ps and pulse energies of tens of picojoules. The pulse energy used in this study amounts to about 10^{-2} pJ, explaining a PL yield, which is comparably lower. The peak intensity of the femtosecond laser pulses is so high already that an increase would damage the structure of graphene.

3.4 Conclusion

In summary, this chapter presented measurements of the ultrafast luminescence from graphene, excited by femtosecond laser pulses on specified sample positions. The total emission spectrum contains three different contributions: four-wave mixing close to the laser excitation energy, coherent photoluminescence which is also spectrally bound to the the excitation energy, and incoherent photoluminescence which is broadband. Four-wave mixing contributions become more dominant for shorter laser pulses while the incoherent PL intensity depends on the total deposited energy and the temporal shape of the excitation. The measured magnitude of the third-order susceptibility of graphene, which originates from the linear band structure near the K-point, amounts to $\chi^{(3)} = 4.3\times10^{-6}$ esu. This is a much larger number than what was obtained for comparable material systems such as thin gold films with $\chi^{(3)} = 10^{-9}$ esu [78]. The most interesting feature of the non-linear susceptibility is that it is basically dispersionless over a large spectral region, as shown here, which makes the material an ideal candidate for phase retrieval. Compared to the standard techniques based on second harmonic light detection of nanoparticles, graphene's near-degenerate four-wave mixing has advantages such as a higher signal yield and a better detectability. Furthermore, two-pulse correlation traces of the non-linear emission were presented, showing a clear maximum of the emission intensity at zero delay. The temporal width of the PL emission is influenced by the local layer number which is visible in the image contrast for the spatially resolved temporal width of the NLPL. As long as the coherent PL can be neglected, the two-temperature model as proposed by Lui et al. [26] in combination with a constant $\chi^{(3)}$ model are able to explain the emission spectra in a very broad frequency range for the two-pulse correlation measurements that were carried out. The overall response time of the PL in the autocorrelation scans show that the electron thermalization is completed approximately within the temporal duration of the laser pulse. A pronounced dependence of the relaxation time with the layer number is observed for multilayer graphene. Here, the relaxation time decreases with increasing layer number, which can be explained by a larger number of available relaxation channels and a decreased total substrate induced doping level, due to the larger number of carbon atoms.

Chapter 4

Phase determination and non-linear imaging of plasmonic nanoparticles

The ability to simultaneously control the spatial extent of light pulses on a nanometer scale and their temporal duration on a femtosecond scale is a key requirement to study the dynamics of individual nanostructures. The general farfield limit of about half the wavelength for the optical resolution can partly be circumvented by near-field optics [1, 2], which in the case of apertureless scattering near field probes comes with the additional advantage of field enhancement [94]. The gap between farfield radiation and nanometer resolution is closed by the antenna effect that small metallic structures can provide [52]. Using spatial light modulators, the temporal pulse shape of a laser in an arbitrary position of the nearfield can in principle be controlled with a very high degree of accuracy [38, 95]. The task is to bring together the two techniques, to benefit from the high spatial confinement and control of the fields in nearfield optics and from the temporal control of pulse shaping microscopy at the same time. Similar attempts have been made since at a number of years, including adiabatic plasmon compression at a sharp metal tip [13, 14, 15], scattering configurations [10, 16] and localized antennas [17, 18, 19].

Common to all methods, the laser pulses get a phase profile imprinted at the pulse shaper which is inverse to all occurring phase distortions of the setup, such that it leads to bandwidth limited laser pulses in the focal region only. To achieve this, an algorithm will aim at maximizing a non-linear feedback signal of a well known reference material by varying the spectral phase of the laser pulse. The idea behind this resembles the one for pulse compression in the focus of a microscope objective (see sect. 2.3), just on the smaller scales, realized by the localized fields of the plasmonic antenna structures. In most cases, the second harmonic (SH) light emission from the metallic nanostructure itself is used [13, 14, 15, 17, 18, 19], which has the advantage that it directly reflects the position of the highest nearfields which presumably creates the majority of the SH signal. Recently, near-degenerate four-wave mixing (ND-FWM) from a sharp metallic tip was used for this purpose [15], extending the approach to other non-linear processes. The aim of all these studies is to temporally control the localized nearfields of a plasmonic nanostructure, thus it is important to emphasize an implicit assumption made in this context: The spectral

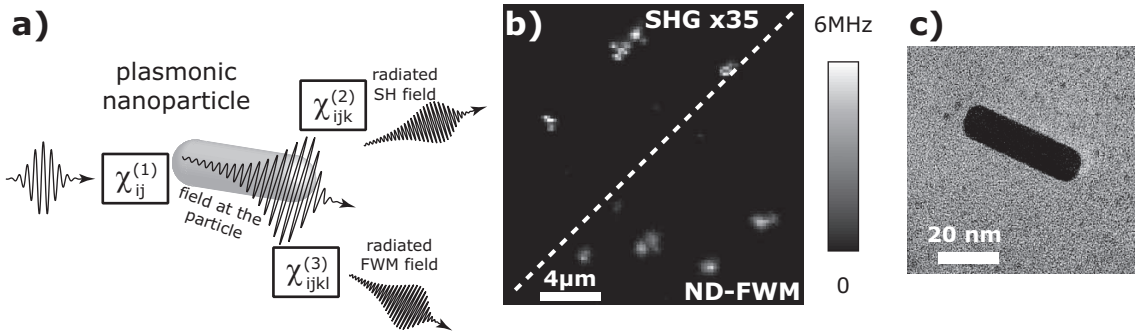

Figure 4.1: (a) Schematic of non-linear light emission from a plasmonic nanorod. The incoming, short laser pulse gets stretched according to the linear susceptibility. The resulting plasmon enhanced fields at the particle are the origin of second harmonic generation (SHG) and four-wave mixing (FWM). (b) Confocal scan of a sample of gold nanorods on glass, detecting SHG and near-degenerate FWM of the particles, excited with a 15 fs laser at 1.55 eV. The SHG signal is 35 times lower than the ND-FWM signal at comparable detection efficiency. (c) Representative TEM image of a gold nanorod.

phase of the surface charges, which is responsible for the second harmonic generation and four-wave mixing, is believed to reflect the spectral phase of the laser pulse in the nearfield outside of the structure.

In the remainder of this chapter, it is first discussed that this assumption is not always justified, especially not at particle resonances or if the non-linear susceptibility carries a phase dependence itself. Second, single particle phase measurements on basis of second harmonic MIIPS and PRISM are presented and third, the study is extended to the third-order nonlinearity of near-degenerate four-wave mixing by plasmonic nanoparticles. The two different non-linear signals are compared and finally used for selective signal enhancement in clusters of nanoparticles. The model system used here are monocrystalline gold nanorods with an average length of 40 nm, deposited on a glass coverslide (see appendix A.3). The dilution of the sample material was chosen such that the majority of particles was well separated on the substrate. The optical resonance of these particles was grouped around a design resonance energy of 1.59 eV (see appendix A.3), which lies inside the available laser spectrum, ranging from 1.45 eV to 1.65 eV. Fig. 4.1 presents a schematic of the non-linear light generation process in such small, metallic nanorods. A confocal scan, detecting SH and ND-FWM demonstrates the general usability of the two processes as imaging contrasts with a very high signal-to-noise ratio.

4.1 The nearfield spectral phase of plasmonic nanoparticles

The spectral phase near a plasmonic nanostructure is generally dependent on the distance to the structure's surface [39], which is much pronounced near the resonance energy. The physical reason is that the scattered nearfields, described by electromagnetic multipole moments, show very strong spatial variations, which explains the general position-phase relation. The origin of the frequency dependence, on the other hand, lies solely in the material's response function (c.f. chpt. 4.3 in 39). As further known from electromagnetics, electric fields have a wave node at perfectly conductive surfaces, implying a phase change of π at that position. Realistic metals possess a finite conductance which results in a nonzero reaction time to impinging electromagnetic waves, therefore the phase change is not exactly π and again determined by the material's response function. The consequence is that the spectral phase of the surface charges of a plasmonic nanostructure is different from the spectral phase in its nearfield.

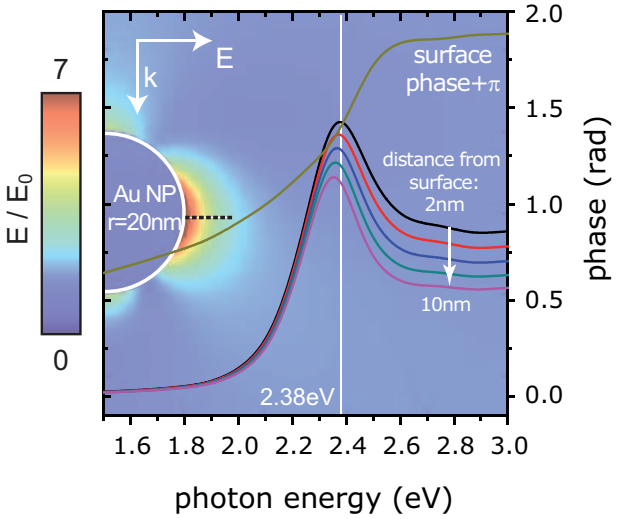

Figure 4.2: False color plot of the electric field distribution $|\mathbf{E}|/|\mathbf{E_0}|$ of a gold nanosphere with a radius of 20 nm inside a medium with a refractive index of $n = 1.518$ under plane wave excitation at the resonance energy of 2.38 eV. Overlaid is the spectral phase parallel to the excitation field for different distances from the surface (black dashed line). The phase at the surface is offset by π.

To demonstrate this situation, fig. 4.2 plots the electric field distribution of a gold[1] nanosphere together with the spectral phase at different positions, calculated by Mie theory [39]. Around the resonance energy of 2.38 eV there is a pronounced maximum in the phase profile which decreases in magnitude for increasing distance to the sphere's surface and also shows a slight red shift if further away from the particle. For a given laser pulse,

[1]The dielectric function of gold was modeled according to the data of Johnson and Christy [96].

the temporal profile of the electric field is therefore dependent on the actual spatial position one is looking at. Furthermore, the phase profile at the surface of the sphere is different from the phase profile on the outside. Assuming that the phase profile at the surface is relevant to non-linear light generation, because it describes the temporal evolution of the electric charge distribution, the phase that is retrieved by methods based on the non-linear response of the particle itself is not the same as the phase in the nearfield of the very same structure. There is an important restriction to this statement, concerning the resonance position: as can also be seen, the phase becomes flat for spectral positions away from the resonance, which means that the group delay dispersion tends to zero at that point. The temporal profile of the pulse at the surface and in the nearfields coincides in such cases, justifying the use of SHG or ND-FWM based methods, because it mainly reflects the laser pulse phase.

4.2 Discussion on phase retrieval by second harmonic generation from plasmonic nanostructures

Gold has a centro-symmetric unit cell which does not permit standard second harmonic generation from the bulk. At the surfaces, this symmetry is broken, leading to an anharmonic electric potential of the electron gas. Driven by the incident laser field, the oscillating particle plasmon then gives rise to SH light emission mainly from the surfaces but also from a nonlocal bulk contribution and electric field gradients inside the structure [97, 98]. This non-linear response $\chi^{(2)}_{ikl}(\omega;\omega_1,\omega_2)$ depends on the material used, the shape of the particle and it also carries a phase response, potentially influencing the SH yield. It is a tensor, so the results for different laser polarizations will not be identical, which also reflects the particle's shape. To further complicate the story, the detectable SH light also depends on the linear susceptibility at the second harmonic frequency $\chi^{(1)}_{ij}(2\omega)$, yet only on its amplitude. The situation is schematically presented in fig. 4.3 at the example of a double resonance, accounting for a long and short-axis surface plasmon resonance, contrasted with the situation of a constant $\chi^{(1)}$ and $\chi^{(2)}$.

As interim result it is noted that maximizing the second harmonic response of a plasmonic nanoparticle provides a spectral phase profile, containing components of the linear susceptibility $\chi^{(1)}_{ij}(\omega)$ of the particle at the fundamental frequency ω as well as a component of the non-linear susceptibility $\chi^{(2)}_{ijk}(\omega;\omega_1,\omega_2)$. The interpretation of this phase is trivial only if the susceptibilities are constant, in which case the phase resembles the laser's spectral phase. If this is not the case, a suitable model has to be used to disentangle the various components [18].

Nevertheless, phase retrieval by second harmonic detection is considered a key technique at the moment [15, 19], partially because it is the best at hand. The challenge is that individual plasmonic particles may give a very weak signal, which limits the phase resolution one can achieve by noise. Fig. 4.4a presents the application of gated MIIPS (G-MIIPS, see sect. 2.3) to an individual gold nanoparticle, showing an acceptable data

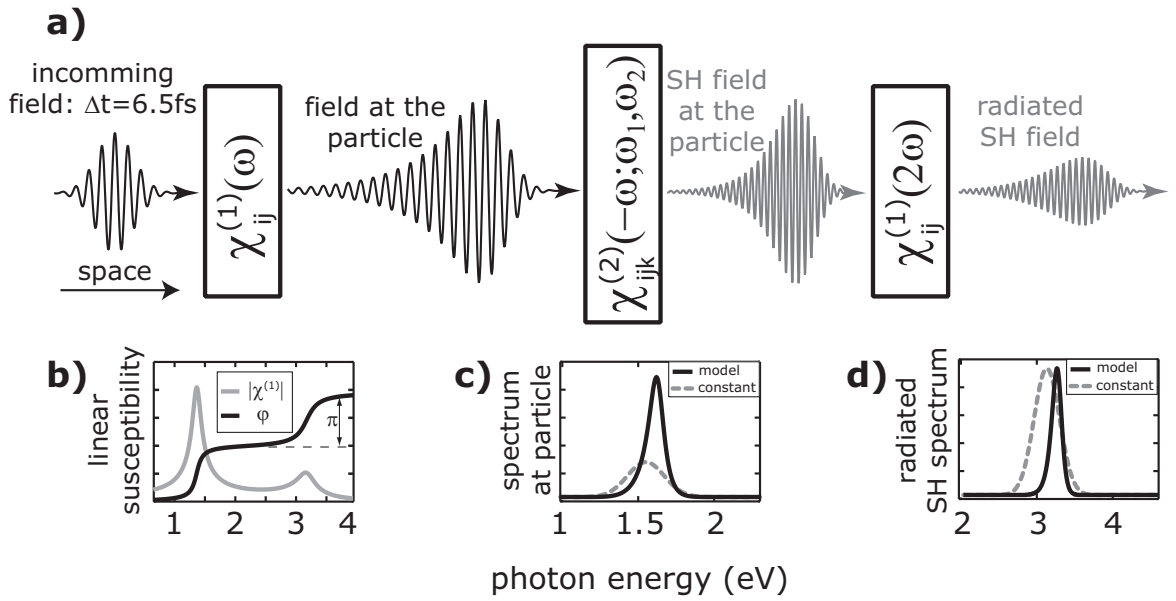

Figure 4.3: Schematic of the second harmonic generation (SHG) process from a plasmonic nanoparticle. (a) Processes involved, (b) linear susceptibility model with two harmonic oscillators, (c) excitation spectrum at the particle, compared to a constant linear susceptibility, showing field enhancement, (d) far-field SH spectrum, compared to a constant linear and non-linear susceptibility (scaled).

quality. A difficulty of MIIPS measurements is that many spectra have to be recorded for a high phase resolution, which is because of the scanning precision on one hand and phase errors inherent to MIIPS on the other hand, demanding several iterations. The use of gated MIIPS is in this case a good compromise between data quality and accuracy, since the overall signal strength is reduced but the method is less prone to errors. Improved MIIPS cannot be used here because an amplitude dependence of the linear susceptibility is expected, which is not covered by the method. As a side note, SH spectra of seven different gold nanorods are presented in fig. 4.5. They vary widely in amplitude and spectral position, reflecting different individual resonances and orientations on the substrate. The spectral window shown in the graph reflects approximately the (frequency doubled) spectral window accessible by the laser, therefore it also demonstrates that the plasmonic resonances do not fully overlap with the given excitation. This amplitude dependence is expected to be a result of the linear susceptibility in the present case (see also theory below).

For the measured nanorod from fig. 4.4a, the phase can be extracted, showing a characteristic profile, plotted in 4.4b along with its scattering spectrum and its second harmonic spectrum under illumination with a pulse, corrected in the focus of the objective. Scattering and SH both have a resonance at similar (fundamental) photon energies of 1.59 eV and 2×1.61 eV and the extracted phase features strong variations over the detected range. From nanorod to nanorod, the measured shape of the phase varies strongly, underlining

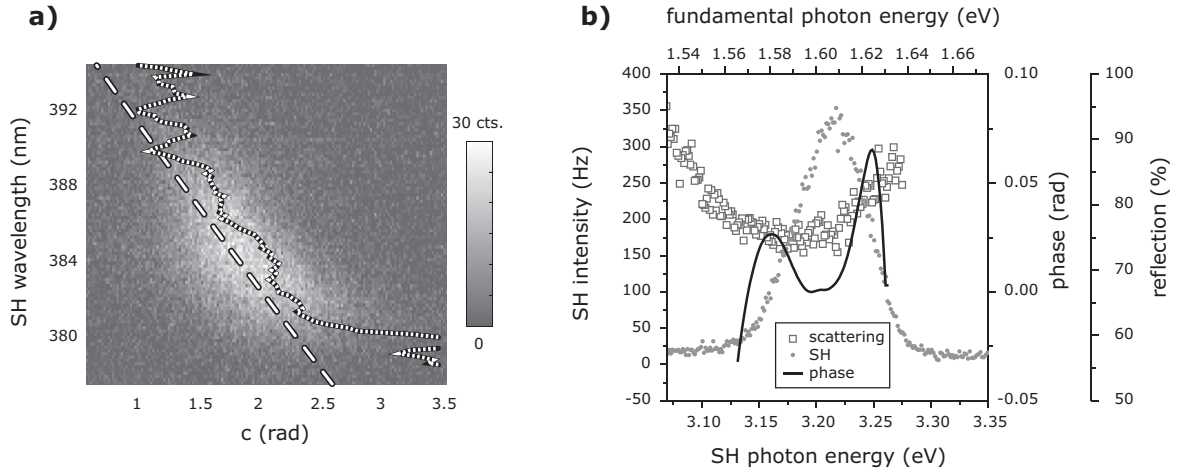

Figure 4.4: (a) G-MIIPS of a single gold nanorod on glass. The line of zero GDD (dashed) is compared to evaluated peak positions (dotted), showing the phase response of the plasmon. (b) Scattering spectrum, SH spectrum and retrieved phase profile of the same nanorod.

the need of individual phase characterization in the context of plasmonic nanoparticles.

For the gold nanorods in use the (linear) phase dependence is illustrated by electromagnetic simulations, based on the boundary element method (BEM) [99], presented in fig. 4.6. The electric field amplitude distribution $|\mathbf{E}(\mathbf{r})|$ around a gold nanorod situated above a glass substrate is plotted at its resonance energy of 1.57 eV. The major part of the second harmonic light as well as the four-wave mixing contribution is expected to originate from the tips of the nanorod, where the highest fields are found at the surface, creating so called "hot spots". Particle plasmons can be well described as Lorentzian (harmonic) oscillators in many cases[2] [39, 52], which results in an arc tangent shaped phase profile over the resonance. Fig. 4.6 shows the spectral phase of the electric field parallel to the plane wave excitation at the tip, which is indeed very similar to an arc tangent, reflecting the spectral position and width of the optical long axis resonance. It is not the same as the experiment's measured phase of fig. 4.4b, because the non-linear susceptibilities are not taken into account here and because the exact geometry and orientation of the observed nanorod are unknown.

Retrieving the spectral phase by second harmonic generation of plasmonic nanostructures is challenging on a technical level but feasible, as has been shown by several groups before [13, 14, 17, 100] and demonstrated in this work too. Applying the inverse phase is then believed to compress the laser pulse in the particle's hot spot, which introduces the problem that possible non-linear phase contributions are not taken into account. The different signatures of the nanoparticles in the second harmonic spectrum and the retrieved phase profiles do show that it is necessary to get an individual pulse compression phase for each particle.

We note that gold also shows two-photon photoluminescence (TPPL) [101, 102, 103]

[2]This does not include the nearfield distribution.

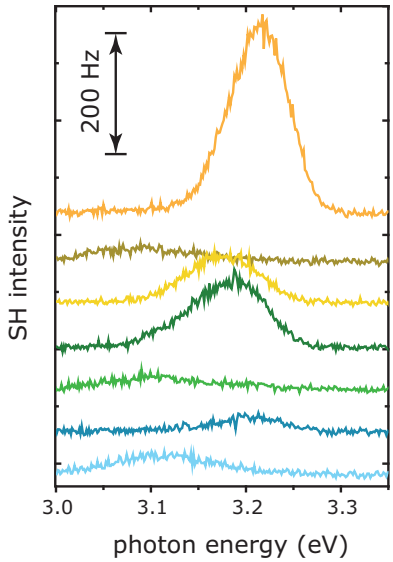

Figure 4.5: Second harmonic spectra of individual gold nanorods. The peak positions and amplitudes result from the different nanorod geometries, described by individual susceptibilities $\chi_{ij}^{(1)}(\omega)$, as well as from non-linear phase and amplitude contributions.

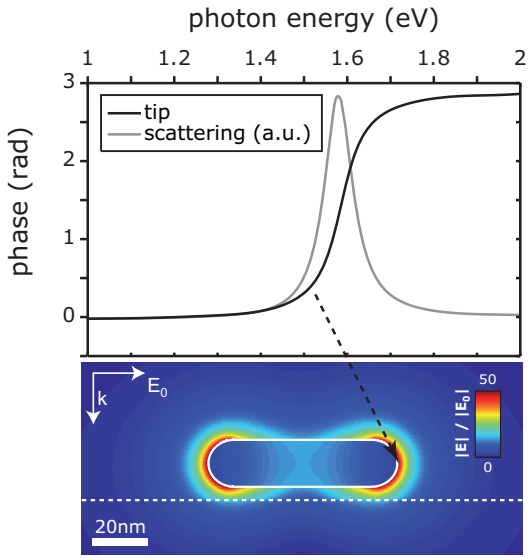

Figure 4.6: Boundary element method (BEM) simulation of phase and electric field distribution for a 65 nm × 19 nm gold nanorod, placed 5 nm above a glass substrate. The phase at the tip undergoes a shift of almost π. For comparison, the scaled scattering spectrum is shown (grey).

when excited with laser light. The strength and spectral shape of this kind of emission is influenced by the particle shape, the crystallinity of the sample and the laser pulse duration. For femtosecond pulses in particular, the yield was found to not depend on the pulse duration anymore [103]. It was shown that polycrystalline samples, as for example produced by gold evaporation and electron beam lithography, have a much higher TPPL yield than monocrystalline samples, which is caused by the nanoscopic structure [104]. In the present case, the TPPL signal was much weaker than the SH signal, which is the reason that it was not included in the description of the non-linear light emission. When working with polycrystalline samples, the background from TPPL was much higher than from the monocrystalline gold nanorods used in this study.

4.3 Non-linear imaging of plasmonic nanostructures

Depending on the temporal shape of an exciting laser pulse, the efficiency of non-linear light generation can vary strongly. This does not only depend on the duration of the pulse in free space but to a large amount on the nanostructure itself. A phase profile that, for instance, efficiently creates second harmonic light at position A, does not necessarily create second harmonic light in another position B, with the same efficiency. Other non-linear processes may have a different dependence on the pulse profile on the very same nanostructure. For imaging, this can either be a difficulty or it can be used as a means to optically distinguish different particles. Near-degenerate four-wave mixing (ND-FWM) of nanostructures has successfully been used as a signal for microscopy, and it is a particularly strong effect in plasmonic nanoparticles, which provide a very high local field strength [105]. Four-wave mixing as a third-order non-linear process is even more sensitive to the field strength and therefore to the pulse phase than second harmonic generation. Up to now, there was no study directly comparing the imaging properties of second harmonic generation and near-degenerate four-wave mixing in plasmonic nanostructures, which both show a very strong signal contrast. Here, exemplary measurements of gold nanorods are presented, demonstrating strong spatial variations of light emission for different phase profiles. It is possible to selectively highlight parts of a sample depending on the particle for which the phase was optimized and on the non-linear process which was used for imaging.

The non-linear polarizability for the cases of second harmonic and near-degenerate four-wave mixing is given by [63]:

$$P^{(SHG)}(\omega = \omega_1 + \omega_2) \propto \chi^{(2)}_{ijk}(-\omega; \omega_1, \omega_2) E(\omega_1) E(\omega_2), \tag{4.1}$$

$$P^{(FWM)}(\omega = \omega_1 + \omega_2 - \omega_3) \propto \chi^{(3)}_{ijkl}(-\omega; \omega_1, \omega_2, -\omega_3) E(\omega_1) E(\omega_2) E^*(\omega_3). \tag{4.2}$$

No difference is made between second harmonic generation and sum frequency generation here because the spectrum of a pulsed laser creates both of them at the same time. Both non-linear susceptibilities have tensorial character but this will be dropped for the reason that the laser polarization is fixed and only nanoobjects are investigated. Therefore, all polarization components are fixed and no propagation effects have to be considered. The

electric field $E(\omega)$ is the electric field *at* the sample, so it carries the phase of the excitation $\varphi_{laser}(\omega)$ plus the phase, imposed by the first-order susceptibility $\phi_{lin}(\omega)$. We assume that the phase $\varphi_{laser}(\omega)$ of the laser pulse is known and tunable. The phase from the non-linear susceptibility shall be called $\psi_{SH}(\omega)$ for SHG and $\psi_{FWM}(\omega)$ for FWM. A flat total phase is the condition for maximum signal emission. According to eqns. 4.1 and 4.2, for a single frequency ω, the following phase relations fulfill the flat phase condition:

$$0 = \psi_{SH}(-2\omega;\omega,\omega) + 2\cdot\big(\phi_{lin}(\omega) + \varphi_{laser}(\omega)\big), \tag{4.3}$$

$$0 = \psi_{FWM}(-\omega;\omega,\omega,-\omega) + \phi_{lin}(\omega) + \varphi_{laser}(\omega). \tag{4.4}$$

Clearly, if a pulse profile $\varphi_{laser}(\omega)$ fulfills condition 4.3, it will not fulfill condition 4.4 at the same time, if the non-linear susceptibilities carry some phase dependencies themselves. More specifically, the difference lies in the phase dependence of the nonlinearity, because the linear optics phase $\phi_{lin}(\omega)$ influences both cases in the same way.

It is now the question if the statements made here can be experimentally verified. Assuming there are two different laser phase profiles $\varphi_{laser}^{SHG}(\omega)$ and $\varphi_{laser}^{FMW}(\omega)$ known, which maximize the SH and the ND-FWM signal respectively, the phase profiles of the non-linear responses cannot be determined directly, unless the linear phase profile $\phi_{lin}(\omega)$ is known too. The reason is, that the two eqns. 4.3 and 4.4 contain three unknowns each, so the situation is under-determined. This is an unfortunate situation, because up to an undefined linear phase, $\varphi_{laser}^{SHG}(\omega)$ and $\varphi_{laser}^{FMW}(\omega)$ can be determined by measurements.

Such measurements are demonstrated at the model system of monocrystalline gold nanorods on glass. Due to the high fields created by surface plasmons, both SHG and FWM are very efficient processes in plasmonic gold nanostructures [15, 19, 106]. In order to retrieve the phase profiles based on SHG or FWM, the "phase resolved interference spectral modulation" (PRISM) technique [10, 68] was used (see sect. 2.3.2). This method records a non-linear feedback signal while systematically varying the phase of the laser pulse by means of an optical pulse shaper. From the resulting trace of intensities, the spectral phase can be reconstructed by a Fourier transform. PRISM is not specific to the type of non-linear feedback signal used, thereby excluding method-specific artifacts when comparing data of different origin. This makes the method very well suited for the purpose of comparing the spectral phase at second harmonic and four-wave mixing conditions. Results for individual gold nanoparticles are presented in fig. 4.7. Since the total phase offset and linear phase cannot be measured by standard non-linear optical techniques [38] and do not influence the temporal pulse shape, they were adjusted to zero. Note that in all three cases the two phases are different from zero, that they do not coincide, and that the SH phase shows generally larger fluctuations over the spectral range than the FWM phase. In contrast, when the measurements were repeated on pristine graphene for FWM [77] and on $Fe_2(IO_3)_3$ nanoparticles [107] for SH as a reference, a flat phase profile for both cases was found, as was expected for bandwidth limited laser pulses (not shown). This result is interpreted such that first, the expected influence of the particle plasmon on the spectral phase of the laser pulse is seen in both situations, and second, that the temporal shape of the laser pulse for optimum second harmonic generation has to be different from the shape for optimum four-wave mixing.

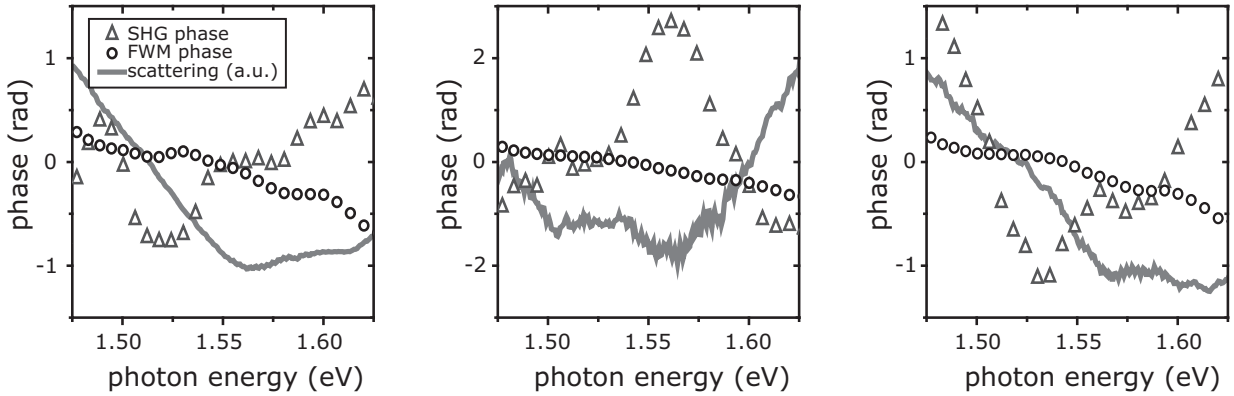

Figure 4.7: Phase retrieved by PRISM on the basis of the particles second harmonic (triangles) and four-wave mixing (circles) for three different gold nanorods on a glass substrate. The scattering spectrum (gray) of the individual particles is given as a comparison.

From a theoretical point of view, it is likely that the observed difference in phase has its origin in the second-order susceptibility $\chi^{(2)}$ and not in the third-order susceptibility $\chi^{(3)}$. Second harmonic generation is caused by a variety of effects which directly depend on the motion of charges, defining the particle plasmon [97, 98]. In other words, the strength of the SHG is influenced by the particle shape not only via the field strength but also via the spatio-temporal evolution of the charge oscillation, which causes nonlocal effects. Four-wave mixing on the other hand is no such collective phenomenon, because it only depends on the bulk third-order non-linear constant $\chi^{(3)}$ plus the local field strength [78]. Since it is a parametric process relying on virtual levels, it is less likely that there is a phase dependence for four-wave mixing at all [63]. To further judge this point, the linear phase of the particles $\phi_{lin}(\omega)$ would have to be measured by an additional method, for instance spectral interference [100, 108], in order to disentangle the three effects.

The knowledge that different non-linear processes in plasmonic nanoparticles show distinguishable phase profiles, makes it is possible to utilize this material specific property for imaging. Fig. 4.8 presents confocal scanning images of a small cluster of stochastically placed gold nanorods. The scan was repeated several times, varying the detection method and the applied phase profile. SH detection was achieved by blocking the laser fundamental and ND-FWM detection was achieved on the Stokes side by using cut-edge longpass filters (c.f. sect. 3.2). First of all, images with a flat phase pulse were recorded. The signal contrast clearly shows that different parts of the structure are highlighted, there is for instance a bright spot in the center of the figure for the second harmonic representation, which is much dimmer in four-wave mixing. Then, a specific spot of the sample, indicated by a white circle, was chosen and the PRISM algorithm was applied at that position for the two detection schemes. With the two resulting FWM and SH phase profiles, the sample was scanned in either way again (data for SH detection and FWM phase is missing).

Using the FWM phase in FWM detection clearly highlights the position which was used for phase determination. The same is true for SH imaging while using the SH correction

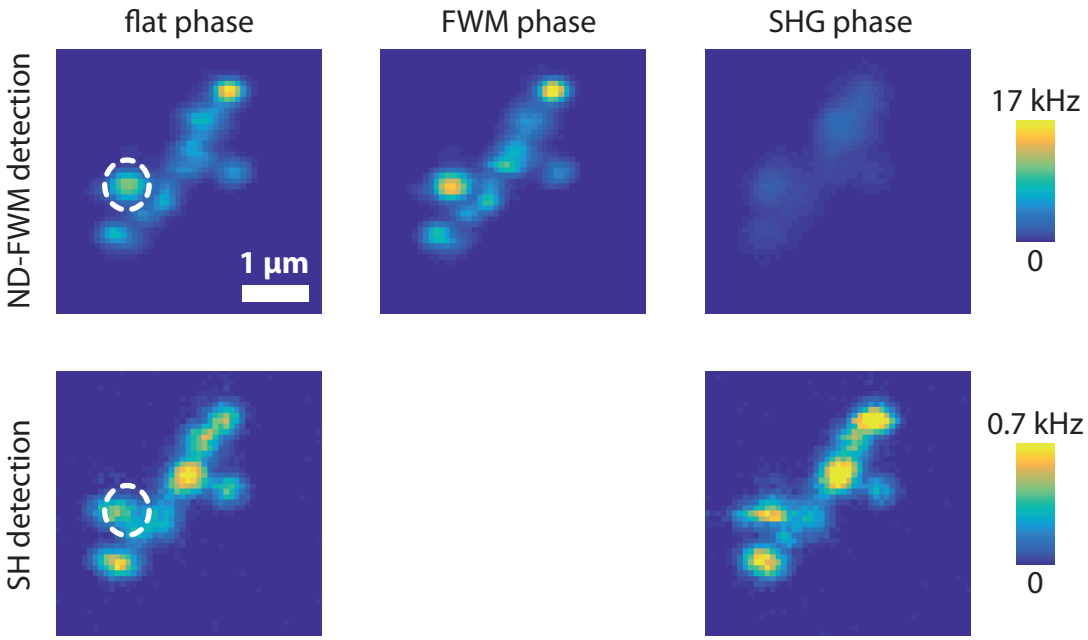

Figure 4.8: Demonstration of selective signal enhancement by near-degenerate four-wave mixing (top row) and second harmonic (bottom row) imaging of a cluster of gold nanorods. Different phase corrections were used in order to record the images, highlighting different parts of the structure. The white, dashed circle indicates the position that was used to measure the phase profile for both methods. (Data for SHG detection and ND-FWM phase is missing.)

phase, but with a different spatial distribution. The overall intensity rises in both versions, but it is more pronounced for second harmonic generation. Scanning the structure in FWM detection by using the SH correction phase leads to a strong decrease in signal. The image appears washed out and does not reach the count rate of the first measurements. The position and method-dependent count rates are able to tell two things. First of all, the notion that the non-linear light emission efficiency depends on the individual spectral features of the nanoobjects is confirmed. The point on the sample, used for phase characterization is later on highlighted because the temporal profile was optimized for exactly this spot. Second, it is possible to enhance or decrease the signal inside the sample in very different positions using the different non-linear processes. As for particle selective imaging or nanoscopic hot spot tailoring experiments, this gives a new degree of freedom for coherent control.

4.4 Conclusion

The temporal and spatial compression of laser pulses is an ongoing and active field of research, which gained momentum by the idea of using the strongly confined plasmonic nearfield of hot spots. Apparent ambiguities in phase retrieval based on the non-linear answer of a plasmonic particle were discussed. These are possible differences of the temporal field profile *at* the surface and *near* the surface on one hand and the partly unknown influence of the non-linear process on the phase the other hand. Ideally, one would use a probe particle, brought to the nearfield in order to measure the phase. Instead, the second harmonic generation was compared to the process of near-degenerate four-wave mixing in plasmonic particles, which, due to the high fields and the third-order intensity dependence, is very strong. It was found that a phase profile, that maximizes the SH yield of a structure typically shows stronger features than a phase profile that maximizes its ND-FWM emission. Hints exist that the influence of SHG on the phase is possibly larger than the influence of ND-FWM. In terms of imaging, both methods can be used in order to enhance different sample areas of a heterogeneous structure, which could have applications in coherent control experiments.

Chapter 5

Coherent dynamics of the radial breathing mode of (5,4) single-walled carbon nanotubes, excited by 20 fs laser pulses

The following chapter is based on the publication (in prep.) "Electronic and vibrational coherences in single semiconducting carbon nanotubes probed by femtosecond pulse shaping microscopy at room temperature" by Ciesielski et al. [109], reproducing text and figures.

Semiconducting single-walled carbon nanotubes (SWCNTs) are quasi-1D model systems that have become increasingly interesting for quantum optical studies and applications. Their electronic properties depend on the number of carbon atoms per circumference

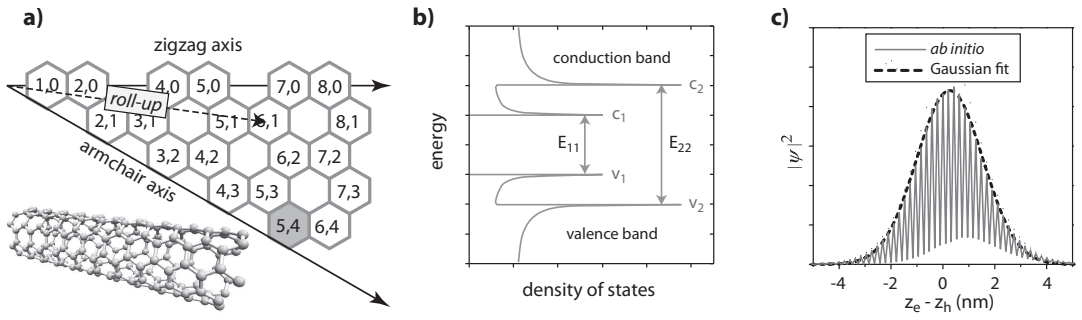

Figure 5.1: (a) Schematic of a honeycomb lattice of carbon atoms, showing the roll-up vector for semiconducting chiralities (n,m) and the structure of a (5,4) carbon nanotube. (b) Density of states for semiconducting SWCNT, indicating the E_{11} and E_{22} transition. (c) E_{11} exciton wave-function of the (11,0) nanotube, in the lowest excited state, *c) adapted from Capaz et al. [110].*

and the precise orientation of the carbon grid, dividing them into groups of metallic and semiconducting nanotubes [34, 35]. Singe walled carbon nanotubes are more than an order of magnitude thinner than the state of the art in transistor size of modern, silicon based chip technology. Therefore they are a potential link to the miniaturization of electronics and moreover, could be used for quantum information technology in the future. After the first observation of the emission of non-classical light in terms of single photons from individual carbon nanotubes at low temperatures [111, 112, 113], recent improvements in nanotube growth and well-controlled doping extended single photon emission to room temperature [37]. A single-walled carbon nanotube is often visualized as a sheet of graphene that is rolled up along a specific vector of the honeycomb lattice of carbon atoms [34], shown in fig. 5.1a. This "roll-up" vector can be expressed as a linear combination of the two unit vectors of the crystal structure and in this way, all different nanotube chiralities can be classified by the two integer coefficients of the roll-up vector, which is therefore called *chiral* vector. The first unit vector is parallel to the "zigzag" axis while the second one is parallel to the "armchair" axis. The chiral vector's angle with the zigzag axis is called the chiral angle, while its length equals the circumference of the tube. Carbon nanotubes as quasi-1D systems show an electronic density of states with distinct peaks, which are van Hove singularities [34, 35] (fig. 5.1b). The first two optically allowed transitions between corresponding valence and conduction bands, called E_{11} and E_{22}, mainly determine the photoluminescence properties of the different chiralities, thereby providing also a powerful tool for their discrimination [114]. Semiconducting SWCNTs have a bandgap on the order of 1 eV between the highest occupied state of the valence band and the lowest available state of the conduction band, which lies between two of the mentioned van Hove singularities (c.f. fig. 5.1b). To first-order approximation, the size of the bandgap is inversely proportional to the tube's diameter [114], such that the wavelength of the first optical resonance scales directly with the nanotube's diameter:

$$\lambda_{11} = \frac{hcd_t}{2a_{cc}\gamma_0}, \tag{5.1}$$

where h is Planck's constant, c the speed of light, d_t the diameter of the nanotube, a_{cc} the carbon-carbon bond length, and γ_0 the interaction energy between neighboring carbon atoms. Better estimates are available, also taking into account the chiral angle [110], but the general trend is confirmed. Single walled carbon nanotubes show a rich spectrum of Raman lines that contain much information about size, structure, defects, and doping [34]. The radial breathing mode (RBM) in particular is a Γ-point phonon mode that periodically increases and decreases the diameter of the nanotube, therefore having an impact on the bandgap energy [115, 116, 117]. The comparably strong Coulomb interaction, which is a consequence of the low dimensionality of the system, leads to a favored creation of excitons at the interaction with light [36]. The average distance of an electron and the corresponding hole, calculated on the basis of *ab initio* or heuristic calculations [110], gives typical values around 1.5 nm for the E_{11} excitons (see fig. 5.1c for an example of a (11,0) nanotube). This number, which can be interpreted as the "size" of the exciton, is 1.1 nm in case of a (5,4) SWCNT, exceeding the nanotube's diameter by a factor of 2.

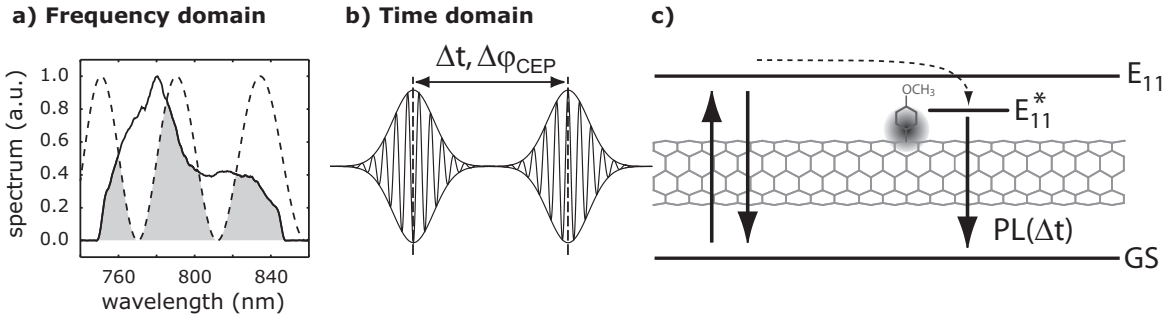

Figure 5.2: Interaction between a pair of phase-locked 20 fs laser pulses and a single carbon nanotube's optical E_{11} resonance. (a) Laser spectrum (solid line), modulation amplitude for a pulse separation of 50 fs (dashed line) and resulting excitation spectrum (grey). (b) Schematic of the pulses in the time domain. (c) Optical absorption is monitored by photoluminescence (PL) emission from a localized sub-band gap dopant state $|E_{11}^*\rangle$ populated by diffusive transport on a picosecond timescale. *Adapted from Ciesielski et al.* [109]

In this chapter measurements are presented, showing coherent wavepacket oscillations of the RBM phonon mode, excited by 20 fs laser pulses, resonant to the E_{11} excitonic transition. The initial few hundred femtoseconds of light absorption by the exciton in single, doped, semiconducting (5,4) SWCNTs of 0.61 nm diameter are investigated by ultrafast pulse shaping microscopy. Photoluminescence (PL) detection of intentionally introduced doping states upon dual-pulse illumination for varying pulse separation provides access to the absorption of the nanotubes, which is periodically modulated by the phonon wave packets. For smaller pulse separations, the experimental signal is mainly determined by the width of the exciton peak of the nanotube, resulting in a measurement scheme similar to a Fourier spectrometer [118]. After this signal contribution has decayed, the coherent wavepackets of the radial breathing mode (RBM) phonon can be identified through oscillations of the PL signal.

5.1 Experimental approach

The approach employed here has previously been used for similar experiments on single fluorescent molecules and organic quantum wires [118, 119, 120, 121, 122], and is schematically shown in fig. 5.2. In the key experiment a single nanotube is resonantly excited at E_{11} by a pair of broadband laser pulses with defined relative carrier envelope phase difference $\Delta\varphi_{CEP}$ and temporal separation Δt. The pulse pair is created by a cosine spectral amplitude mask at the pulse shaper (fig. 5.2a), which allows to control the temporal separation and the carrier envelope phase difference in a spectral fashion. A prerequisite to achieve the time domain pulse profile, depicted in fig. 5.2b, from the amplitude mask, is a bandwidth limited (flat phase) laser pulse, which was achieved by compressing the pulses on a reference sample of $Fe_2(IO_3)_3$ nanocrystals (see sect. 2.3). The resulting, tailored excitation pulses interact with the SWCNT by its E_{11} optical resonance, creating an exciton. The

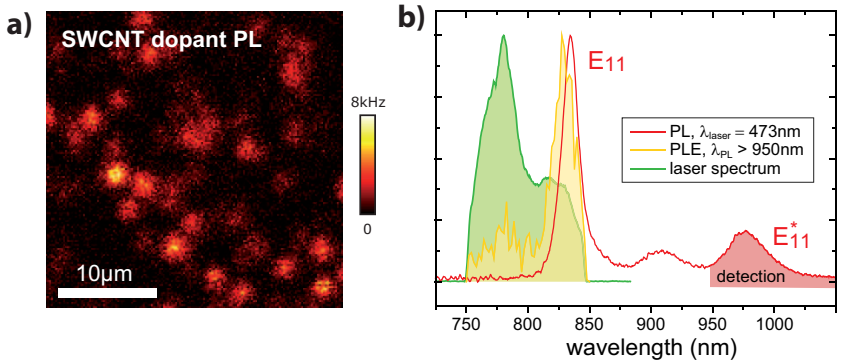

Figure 5.3: (a) Confocal PL image showing individual bright spots resulting from single SWCNTs, typically shorter than the image resolution. (b) The PL spectrum of a single SWCNT obtained upon E_{22} excitation shows spectrally distinct E_{11} and E_{11}^* emission. The photoluminescence excitation (PLE) spectrum of the same SWCNT detected at the E_{11}^* emission demonstrates the population of this state upon E_{11} excitation. The laser spectrum (green) used for the ultrafast experiments covers the complete range of the E_{11} absorption. *Adapted from Ciesielski et al.* [109]

absorbed light intensity is monitored by a defect state, luminescent at lower energy (see fig. 5.2c). A confocal PL image of a typical sample area is shown in fig. 5.3a. Well-isolated PL signals of similar brightness are seen that arise from the emission of (5,4) SWCNTs as verified by confocal PL and photoluminescence excitation (PLE) spectra recorded at a number of these bright spots, exemplary shown in fig. 5.3b.

The Stokes-shift between exciton absorption and emission in SWCNT is very small, on the order of 5 meV for the studied nanotubes (fig. 5.3b), so resonant broadband excitation of the $|E_{11}\rangle$ state and detection of its emission is practically impossible. Therefore doped SWCNTs were studied, which provide emission from localized dopant states $|E_{11}^*\rangle$ approximately 130 meV below $|E_{11}\rangle$ as reporter for the $|E_{11}\rangle$ population. Photoluminescence excitation (PLE) spectra of the studied SWCNTs, shown in fig. 5.3b and in fig. A.6 in the appendix, confirm that E_{11} excitation leads to the population of the $|E_{11}^*\rangle$ state presumably by efficient diffusive transport along the nanotube [37, 123, 124, 125].

5.2 Broadband excitation spectroscopy

The described experimental approach of measurements at optical excitation with two identical laser pulses is similar to the method of Fourier transform spectroscopy. In Fourier transform spectroscopy, a spatial delay between two optical paths is scanned and the resulting interferogram can be used to retrieve spectral information about the absorption by means of a Fourier transformation [126]. In the present case, no physical delay has been introduced, but the spectrum was modified in a way, which is equal to the coherent superposition of two temporally separated laser pulses. The only difference of the excitation spectrum to the case of a Michelson interferometer, as it would usually be used for Fourier transform spectroscopy, is the fixed carrier envelope phase difference of the two pulses. In fig. 5.4a a PL intensity measurement of a single (5,4) carbon nanotube is presented for increasing pulse separation Δt and constant carrier envelope phase difference $\Delta\varphi_{CEP} = 0$ within the first 300 fs.

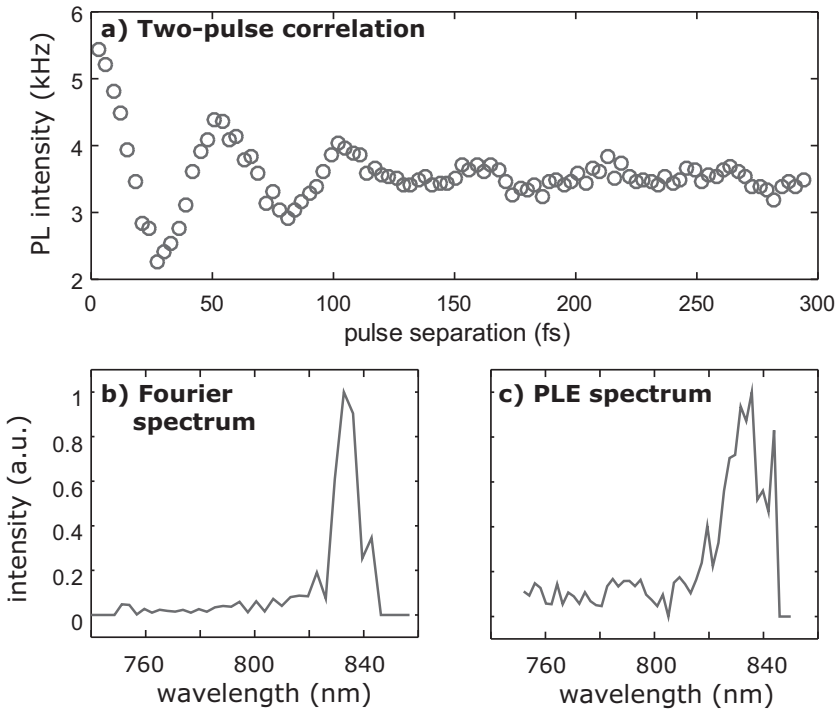

Figure 5.4: (a) Two-pulse correlation experiment on an individual (5,4) SWCNT, varying the temporal delay between two identical 20 fs laser pulses with a fixed carrier envelope phase difference of zero. Monitored is the defect PL. (b) The Fourier transform, normalized to the laser spectrum, gives the absorption spectrum of the nanotube, which is compared to (c) the photoluminescence excitation (PLE) spectrum of the same nanotube. *Adapted from Ciesielski et al.* [109]

The measured PL trace shows rapidly decaying oscillations with a period of about 50 fs, mainly reflecting the spectral detuning $\omega_{SWCNT} - \omega_0$ of the transition energy of the

SWCNT $\hbar\omega_{SWCNT}$ vs. the laser energy $\hbar\omega_0$. As a consequence of the fixed carrier envelope phase difference between the two pulses, there are no interference fringes with the period of the exciting laser field visible, as they would occur in a Michelson interferometer.

The spectral information about the absorption, encoded in a two-pulse correlation trace like in fig. 5.4a, lies in the convolution of the nanotube's interferogram with the interferogram of the laser spectrum [118, 126]. It can be shown, that a Fourier transform of the recorded signal $S(\Delta t)$ yields the absorption spectrum $A(\omega)$, multiplied with the excitation spectrum, such that the wanted information is given by:

$$A(\omega) = \frac{\mathcal{FT}\left[S(\Delta t)\right](\omega)}{I_{laser}(\omega)}. \tag{5.2}$$

Fig. 5.4b presents the signal that was retrieved from the recorded data by eq. 5.2 and compares it with the corresponding PLE data in fig 5.4c. The wavelength axis in fig. 5.4b had to be adjusted according to the detuning and the central laser wavelength of 790 nm, because this information is not contained in the two-pulse correlation trace at fixed CEP difference[1]. Both spectra contain information on the absorption and, as expected, look similar. The spectral position of the peak reflects the absorption band of the excitonic resonance and the width of the peak results mostly from dephasing. At sufficient signal contrast and resolution, a linewidth analysis could be used in order to split the peak shape in contributions of pure dephasing and other effects, as for example heterogeneous broadening [127]. Using the full-width-at-half-maximum of the absorption peak of the observed individual (5,4) carbon nanotubes, dephasing times of around 100 fs to 200 fs are extracted. This is in general agreement with dephasing times around 200 fs which have been determined for micelle suspended SWCNTs using four-wave mixing and transient absorption spectroscopy at the ensemble level [128, 129]. For single polymer-suspended or freely suspended SWCNTs at 9 K where the RBM-induced dephasing is absent, dephasing times reaching up to 830 fs and 2.1 ps, respectively have been reported [130].

Due to a detection regime which is spectrally separated from the excitation, broadband excitation spectroscopy has an excellent signal-to-background contrast, for which reason it is very sensitive and can also be applied to single molecules [118] or SWCNTs, as has been shown here. Compared to a conventional absorption spectrum, no total absorptivity can be extracted from the data, because the measurement does not directly record the absorbed energy. This represents also the main difference to Fourier transform infrared (FTIR) spectroscopy, where typically the transmission or scattering of a sample are the measured quantities [126]. Different from the approach with a beam splitter and a delay stage, the current version does, in theory, not require any coherence of the incoming light field. This is due to the fact that the *spectrum* of the excitation is modulated by the pulse shaper [131] and only in case of a bandwidth limited, broadband laser pulse, the cosine modulation results in the anticipated two-pulse correlation experiment (c.f. fig. 5.2a and b). For the present measurement, the incoming laser pulses were always bandwidth limited, which was ensured by the mentioned non-linear reference measurements on $Fe_2(IO_3)_3$ nanocrystals.

[1] In contrast, an interferometric two-pulse correlation scan also contains information about the absolute position of the spectrum on the frequency axis.

In principle, this enables measurements reaching much further than the so far introduced, linear technique of broadband excitation spectroscopy. The excited optical resonance in the carbon nanotube is a quantum system that carries a specific time dependence, leading to the observed absorption band, which is broadened by dephasing. The mechanics of this dephasing could be described by a suitable model, in the simplest case a two-level system, leading to a deeper insight in the underlying dynamics [132]. Studies based on this would require a non-linear power regime to operate in, where the temporal resolution of the given laser source can be exploited [131]. It is very likely that the experiments, presented here, already fulfill the requirements for coherent control and excite and modulate the E_{11} optical resonance on a femtosecond time-scale. Nevertheless, it is not possible to prove this notion at the moment, because the detected signal is linear with the input intensity.

5.3 Temporal trace of the radial breathing mode

Upon closer examination of the time traces of single carbon nanotubes as in fig. 5.4, an additional oscillating feature at pulse separations larger than 150 fs can be seen, which substantially exceeds the dephasing times and therefore has a different origin. Fig. 5.5a shows the two-pulse correlation trace of a SWCNT up to 500 fs pulse separation. After the complete decay of the initial oscillations at around 150 fs, three distinct maxima with a separation of about 90 fs are seen. These can be assigned to the coherent excitation of the radial breathing mode (RBM) of the carbon nanotube, which for (5,4)-SWCNTs occurs at 373 cm^{-1} [114, 133], corresponding to an oscillation period of $T_{RBM} = 90$ fs.

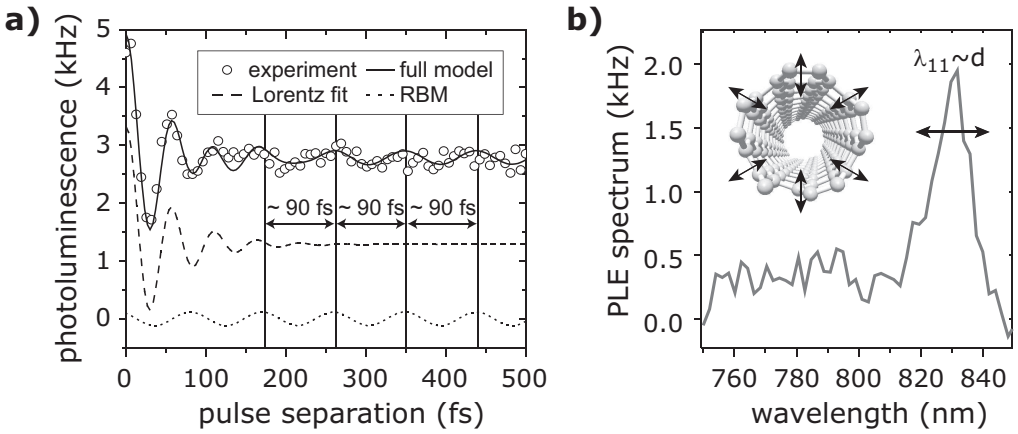

Figure 5.5: Vibrational coherence in a single carbon nanotube. (a) For larger pulse separations, coherent phonon oscillations with a period of about 90 fs, caused by the radial breathing mode (RBM) become visible. The absorption-dominated and coherent vibrational contributions to the full model function are shown as offset, dashed lines. (b) The RBM periodically modulates the diameter d of the nanotube, leading to a proportional shift of the E_{11} absorption wavelength. *Adapted from Ciesielski et al.* [109]

Coherent vibrational wavepackets in single molecules are well known, and have been visualized via fluorescence detection by Brinks et al. [120]. In carbon nanotubes, coherent phonon excitation has been studied theoretically and experimentally on the ensemble level using ultrafast pump-probe spectroscopy [115, 116, 117]. The influence of the RBM on the detected photoluminescence time traces is understood as follows: the first laser pulse creates coherent phonon wave packets by impulsive excitation. The 20 fs duration of the bandwidth limited laser pulse is substantially shorter than the 90 fs oscillation period of the phonon, so its excitation can be considered quasi-instantaneous. Since the radial breathing mode is characterized by a periodical modulation of the nanotube's diameter d, the second laser pulse experiences a modulated absorption, caused by the diameter-dependent excitonic absorption energy $\hbar\omega_{SWCNT} \propto 1/d$ [116, 117]. Because in the present experimental configuration the E_{11} absorption is at the low energy edge of the laser spectrum (c.f. fig. 5.3b), phonon induced shifts of the excitonic energy towards lower energies are expected to lead to smaller total absorption, while the opposite is the case for high energy shifts [117, 134, 135].

Following this discussion, the coherent phonon-induced intensity modulation of the PL signal I_{RBM} can be described using a sine function:

$$I_{RBM} = \alpha_{RBM} \cdot \sin(\omega_{RBM}\Delta t + \phi), \tag{5.3}$$

with phase ϕ and amplitude factor α_{RBM} scaling the signal contribution relative to the stronger signal contributions of the first 150 fs. The total signal is modeled as:

$$I_{PL} = I_{TPC} + I_{RBM}, \tag{5.4}$$

where I_{TPC} is the intensity signal of the two-pulse correlation. In order to separate the signal contributions, a model fit was used to describe the initial oscillations of the recorded PL trace. In the last section, this part was explained to result from the modulated laser spectrum, convoluted with the absorption spectrum of the sample. A re-calculation of the PL trace by an inverse Fourier transform of the measured absorption spectrum would include the contribution of the RBM phonon oscillation and is therefore not suited to extract this part of the signal. By using a Lorentzian fit to the absorption spectrum, it is possible to simulate the measurement without the influcence of the RBM and get to a model description that resembles the experimental data closely (dashed line in fig. 5.5). The central wavelength, determined from the recorded trace of fig. 5.5, is $\lambda_{SWCNT} = 830\,\text{nm}$, and the full-width-at-half-maximum amounts to $\Delta\lambda = 26.6\,\text{nm}$, corresponding to a dephasing time of $T_{dep} = 86\,\text{fs}$. The resulting part I_{RBM} can, for pulse separations larger than 150 fs, be fitted to the experimental curve, which yields the parameters α_{RBM}, and ϕ. The chirality-dependent frequency $\omega_{RBM} = 0.07\,\text{rad/fs}$ is known [114, 133]. In fig. 5.5, the time trace of a single nanotube together with the model fit and the two contributions I_{TPC} and I_{RBM} are shown.

Theory predicts that upon impulsive excitation at the E_{11} transition the nanotube diameter of SWCNTs for which $[(n-m) \bmod 3 = 1]$ first expands [117]. Due to the inverse scaling of the band gap energy with the diameter [114], this is connected to an initial redshift of the absorption for (5,4) SWCNTs. As said before, this results in a decreased overlap

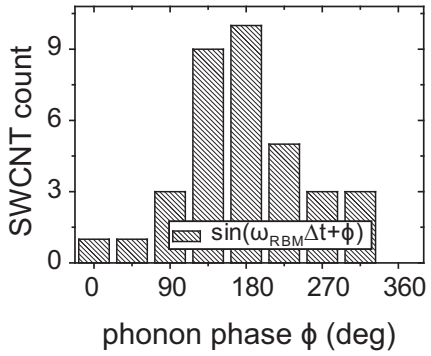

Figure 5.6: The histogram of the initial phonon phase proves that under impulsive excitation, the (5,4) carbon nanotubes initially increase their diameter. *Adapted from Ciesielski et al.* [109]

of laser spectrum and absorption band in the present case. If the detected PL signal at sufficiently large pulse separations is interpreted as a measure of absorption, then an initial decrease of the PL intensity is predicted. According to the simple model of eq. 5.3, such a decrease corresponds to an absolute phase ϕ of the RBM oscillations of 180°. Out of the experimental data sets, 35 SWCNTs showed a sufficient signal contrast to fit the sinusoidal RBM signature to the autocorrelation trace. Fig. 5.6 shows a histogram over the retrieved set of nanotubes which is heterogeneous but has a clear maximum at a phase of 180°, supporting the notion of the nanotube initially expanding upon impulsive excitation.

5.4 Conclusion

In this chapter, the photoluminescence response of single semiconducting carbon nanotubes to a pair of 20 fs laser pulses was investigated, where the temporal separation of the pulses was varied and the carrier envelope phase difference between the two pulses was kept constant. On a sub-150 fs timescale, the resulting PL traces contain spectral information about the absorption bands of the nanotube, which can be retrieved by a simple Fourier transform, similar to FTIR spectroscopy. On longer timescales, coherent phonon wave packets of the radial breathing mode modulate the optical response with a period of about 90 fs. Statistical evaluation of 35 individual nanotubes showed that the probability of absorption of the second laser pulse is initially decreased. In accordance with theoretical predictions, this result is interpreted such, that on the onset of the coherent wave packet oscillations under impulsive excitation the nanotube's diameter would first expand.

In the future, studies in the non-linear regime of absorption on SWCNTs are desirable, because they enable true coherent control experiments on the single nanotube level. A potential extension of the detection scheme to electrical readout is promising as well, since they open the door to exciton dynamics and transport properties [34, 136].

Chapter 6

Summary and outlook

In the course of this work, a measurement scheme was implemented that allows to temporally control femtosecond laser pulses in the diffraction limited spot of a confocal microscope. Up to now, it was a highly difficult task to measure and compensate the phase distortions that are introduced by the optics, first of all by the objective lens. The work presented here aims at simplifying phase retrieval by demonstrating improved versions of second harmonic based pulse phase measurements and suggesting the use of graphene's near-degenerate four-wave mixing as reference signal. This lead to a better understanding of the accuracy and precision which can be reached within the scope of confocal pulse shaping microscopy. Benefiting from the achieved temporal and spatial resolution, the ultrafast and non-linear photophysics of graphene were investigated, leading to new insights about the corresponding fundamental mechanisms. The question of the temporal pulse profile in the vicinity of hot spots, created by plasmonic nanostructures, was reviewed, focussing on the two non-linear processes of second harmonic generation and four-wave mixing. Finally, coherent control of the radial breathing mode in individual, semiconducting, single-walled (5,4) carbon nanotubes at room temperature was demonstrated. In more detail, the key findings are presented in the following.

As an important prerequisite for time-resolved measurements of nanostructures, a setup was built that combines a spatial light modulator for pulse shaping with a confocal microscope operating at the diffraction limit of light. The spatial resolution lies at about 400 nm at laser pulses of 1.55 eV central energy and 15 fs temporal resolution. The resulting configuration is very flexible with respect to the spectral phase and amplitude profiles that can be applied to the laser pulse. This flexibility was achieved by a specialized software for the setup, which was developed during this work, that implements all the various scanning procedures presented and reviewed here. Examples are MIIPS, chirp scans, PRISM, a genetic algorithm, and phase-locked two-pulse correlation schemes. To determine the pulse phase distortions that were accumulated throughout the optical path, mainly the popular technique of MIIPS was used. In our group, the scanning algorithm was improved by introducing an amplitude gate that minimizes inherent phase artifacts and thus requires less iterations than the original version. The phase retrieval algorithm was further improved

by including information on the laser spectrum. This thesis demonstrated experimentally that these approaches give better results than the standard MIIPS. Most importantly, the necessity of iterating the procedure is dispensed, which speeds up the process and is an advantage at low signal intensities orif the samples are not photostable. The total accuracy which can be achieved was reviewed, demonstrating a precision of better than $50\,\mathrm{fs}^2$ for quick routine measurements and better than $10\,\mathrm{fs}^2$ at the detection limit of the system. This corresponds to an uncertainty of about 1 fs at bandwidth limited laser pulses of 15 fs duration, centered at 1.55 eV in the focus of an NA 1.3 microscope objective.

Exfoliated graphene was the very first mono-atomic material that was available and has therefore attracted much attention. Along the line, immense research activities were triggered by the new properties of the quasi-2D material. In this thesis, two detailed studies of the non-linear photophysics of single layer graphene on a glass substrate contributed to this field of research. First, the third-order nonlinearity, which leads to easily detectable near-degenerate four-wave mixing signals, was investigated. This kind of emission is spectrally centered around the laser excitation and shows a three times as broad spectrum as the laser. It was shown experimentally during this work that the third-order non-linear susceptibility of graphene is dispersionless in the probed spectral range which makes it an ideal candidate for phase characterization. Compared to the standard approach using second harmonic generation, the third order signal has the advantage of being spectrally close to the laser. This fact often makes it easier to detect than second harmonic light, because the optics do not have to transmit ultraviolet light. Next, the first experimental evidence for the existence of two kinds of non-linear photoluminescence from graphene was provided: there is a coherent and an incoherent contribution. The coherent one is spectrally bound to the laser and overlaps with the near-degenerate four-wave mixing in some cases. The incoherent one is broadband and in its magnitude and peak energy mainly determined by the total amount of light absorbed during the interaction with the laser pulse. The incoherent part was further investigated and a characteristic dependence on the substrate induced doping was found, demonstrating a generally increased speed of the charge carrier cooling at higher doping levels. Combined, these three contributions describe the full non-linear optical signal of graphene from the visible to the near-infrared spectral region.

Optical microscopy has the potential to be used at a spatial resolution below the diffraction limit by exploiting the localized nearfields of plasmonic nanostructures. The concentrated light fields, created inside so called hot spots, can in principle also be used for pulse shaping microscopy, but for this purpose their spectral phase has to be measured. Recent approaches to phase measurement, using the second harmonic generation of the nanostructures themselves, were reviewed and demonstrated by applying MIIPS to single gold nanorods. It was confirmed that the phase profile depends strongly on the microscopic details of the nanoparticles, which underlines the need for individual correction phases. Since the phase profile, measured by non-linear processes of the particle itself, will in general be different from the phase profile in its nearfield, these measurements were contrasted with similar data, obtained by near-degenerate four-wave mixing from the same particles. The

phase profiles are different, but the origin could not be explained with certainty. It was demonstrated that the different non-linear processes can nevertheless be useful for selective imaging of plasmonic nanostructures.

The last material system investigated in the course of this thesis were semiconducting, (5,4) single-walled carbon nanotubes. The first optical resonance, caused by the formation of the E_{11} exciton, causes an absorption band which can be measured by broadband excitation spectroscopy with single nanotube detection sensitivity. Two-pulse correlation experiments were presented that showed evidence of coherently excited wave-packets of the radial breathing mode for pulse separations larger than 150 fs. The expected oscillation period of about 90 fs could directly be observed in the recorded trace, caused by a periodic modulation of the bandgap. Statistical data evaluation furthermore proved the theoretical prediction, that under impulsive excitation the diameter of a (5,4) nanotube would first expand.

The results presented in this work demonstrate the feasibility and robustness of the combined approach of optical pulse shaping and confocal microscopy and give new insight into the photophysics of selected nanostructures. Both techniques on their own are powerful already, but the opportunity of a simultaneous temporal control of light fields at the diffraction limit and at the bandwidth limit is intriguing. The investigation of nanostructures in general benefits from the access to small scales and a high temporal resolution. Therefore, for future measurements the spectral width of the pulses should be increased and the excited spectral volume should be decreased, for instance by using plasmonic nearfields. Experiments would further benefit from a larger flexibility with respect to the spectral range, which was fixed for most experiments presented here. The connected challenges are of technical nature, since laser sources are available for a large variety of spectral ranges and pulse compression can meanwhile well be handled. Electrical readout of photoexcited carriers is an important next step for experiments on materials such as graphene or carbon nanotubes since it opens the door to transport measurements. These carry potentially much information about the physical processes involved and are also of interest for opto-electronic applications. Finally, optical pulse shaping is a technique that acts on the excitation of a sample only. General improvements can be expected in time-resolved detection schemes, such as time-correlated single photon counting. An approach that combines time-resolved excitation and time-resolved detection in microscopy could open the door to interesting new discoveries.

Appendix A

Sample materials: Fabrication and characterization

A.1 Iron(III)-idodate nanocrystals

Iron(III)-iodate ($Fe_2(IO_3)_3$) nanocrystals provide a high, stable, photo-resistant, and phase-free second harmonic signal, ideally suited as a local probe for phase retrieval, based on second harmonic light detection [107]. The nanocrystals used throughout this work were home made, based on the procedure described by Bonacina et al. [107]. The sample material is emulsed in purified water, treated with ultrasound for about one minute and then spin-coated on a glass coverslide. A scanning electron microscopy image of such crystals on a fluorine tin oxide substrate is presented in fig. A.1, showing that the material consists of sub-micron, needle like structures.

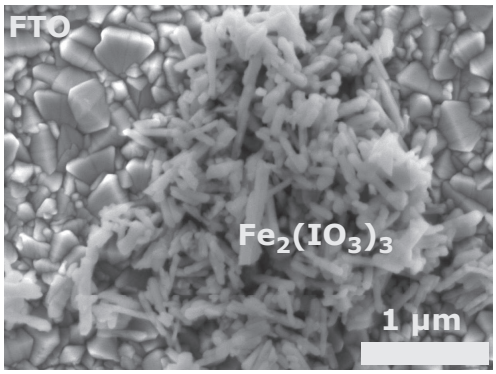

Figure A.1: Scanning electron micrograph of $Fe_2(IO_3)_3$ nanocrystals on a substrate of fluorine tin oxide (FTO).

A.2 Exfoliated graphene on glass substrates

Samples of graphene on glass were used in chapt. 3. They were fabricated in the group of Andrea C. Ferrari at the Cambridge Graphene Centre, United Kingdom. Graphene layers are deposited by micromechanical cleavage [137] on Si wafers covered with 300nm of SiO_2. Monolayers are identified by a combination of optical microscopy [25] and Raman spectroscopy [24, 138]. Graphene layers are transferred onto glass by a polymer-based wet transfer process [23]. PMMA (molecular weight 950K) is spin coated onto the substrate where graphite flakes are exfoliated, then the sample is immersed in de-ionized water, resulting in the detachment of the polymer film due to water intercalation at the PMMA-SiO_2 interface [23]. The flakes attach to the polymer and can be removed from the Si/SiO_2 substrate. The polymer and graphene film is then placed onto the glass substrate and, after complete drying of the water, PMMA is removed by acetone. Success of the transfer is confirmed both optically and by Raman spectroscopy. No significant D peak is detected after transfer, showing that the process does not result in structural defects.

In fig.A.2 we present Raman spectra of the areas indicated in figs. 3.12c and 3.14a. It is possible to identify single layer, double layer, few layer graphene and graphite.

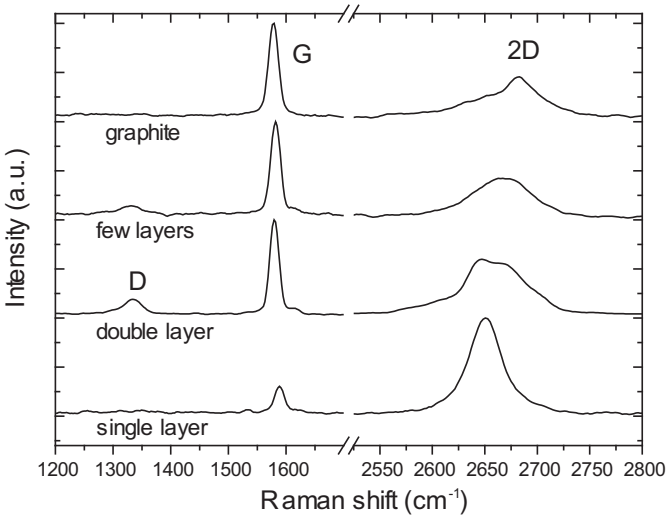

Figure A.2: Raman spectra of graphene at 633 nm excitation wavelength of different positions as indicated in figs. 3.12c and 3.14a. Comparison with references [24, 138] enables identification of single, double and few layer graphene as well as graphite.

Graphene on glass is typically p-dopend and in the literature, values of $\mu = -0.12\,\mathrm{eV}$ are reported for graphene on a glass substrate [93]. Fig. A.3 gives an approximate doping level of $p = 2 \times 10^{12}\,\mathrm{cm}^{-2}$, coming from the substrate or the PMMA transfer. Using the electronic density of states $D(E) = 2E/(\pi\hbar^2 v_F^2)$, a value for the chemical potential of: $\mu = -\hbar v_F \sqrt{\pi p} = -0.18\,\mathrm{eV}$ is calculated.

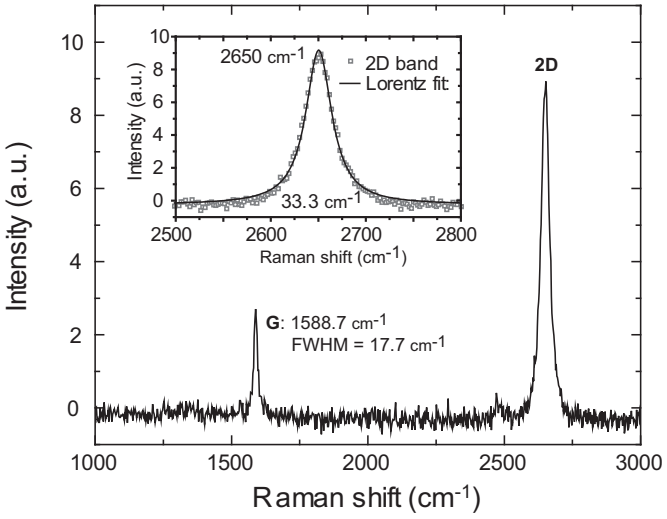

Figure A.3: Raman spectrum at 633 nm excitation wavelength of single layer graphene (position 1 in Fig. 5b of the main manuscript.) According to Ferrari [139], the position of the G-band indicates a doping level of $\approx 2 \times 10^{12}\,\mathrm{cm}^{-2}$.

A.3 Gold nanorods

Gold nanorords, as used in chpt. 4, were grown in solution by the group of Sebastian Mackowski at the Nicolaus Copernicus University in Toruń, Poland [140]. The particles were covered by a layer of cytric acid to prevent them from clustering through van der Waals forces. Fig. A.4 shown transmission electron micrographs (TEM) of typical nanorods and a size distribution histogram. The average length is 41 ± 11 nm, the average thickness is 19 ± 5 nm. Their plasmon resonance on glass lies at about 1.6 eV. Fig. A.5 presents an ensemble measurement of the nanorods in water.

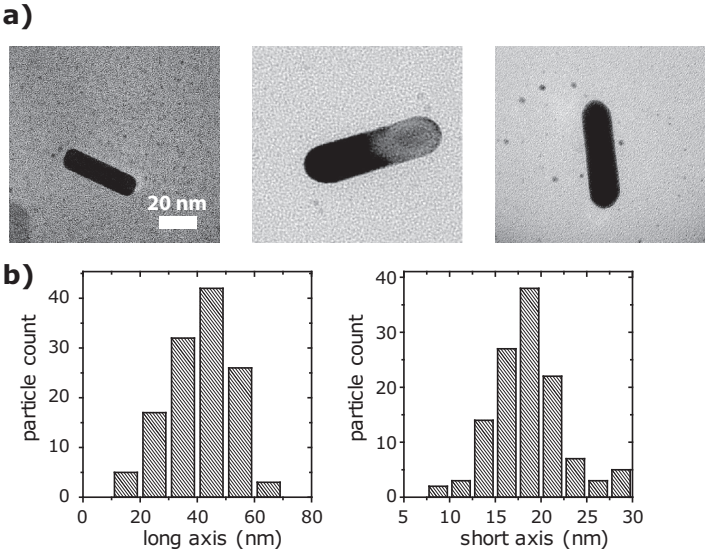

Figure A.4: (a) TEM images of typical Au nanorods. (b) Size distribution histograms.

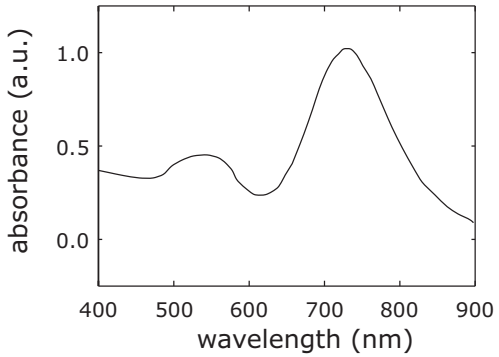

Figure A.5: Absorbance spectrum of the gold nanorods in water. *By courtesy of D. Piatkoswki, Nicolaus Copernicus University of Toruń, Poland*

A.4 High purity (5,4) single-walled carbon nanotubes with engineered defects

Chpt. 5 used samples of (5,4) SWCNTs with engineered defects, that were synthesized according to the following description in the group of Stephen K. Doorn at Los Alamos National Laboratory, Los Alamos, United States of America. CoMoCAT SG76 grade SWCNTs were dispersed through ultrasonication and subsequently cleaned from bundles and prefractionated by ultracentrifugation. Enrichment in single-species (5,4) was accomplished via the iterative aqueous two-phase extraction (ATPE) technique, based on results described previously by Fagan et al. [141, 142]. The resulting (5,4) material was exchanged into a sodium dodecylsulfate (SDS) environment to enable doping with 4-methoxybenzenediazonium tetrafluoroborate following an adapted protocol established by Piao et. al. [143]. After the doping process the reaction was quenched and the sample stabilized by changing the surfactant environment back to sodium deoxycholate (DOC) [123]. A PLE spectrum of the sample material used is presented in fig. A.6. To reduce blinking, the SWCNTs stock solution was embedded in Tetramethylorthosilicate [144, 145] (TMOS). The resulting gel was deposited between two borosilicate coverslides (BK7) for the optical measurements.

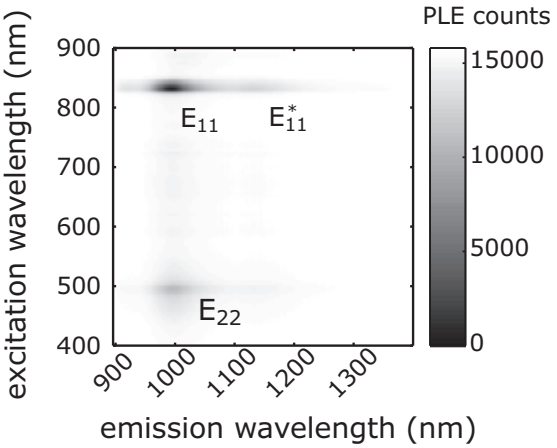

Figure A.6: Photoluminescence excitation (PLE) scan of the (5,4) SWCNT sample, dissolved in water. The spectra, taken with a Xenon lamp, reveal the transitions E_{11} and E_{22} as well as the defect band E_{11}^{*}. *By courtesy of N. F. Hartmann, Los Alamos National Laboratory, US.*

Appendix B

Collected formulas

B.1 Focal fields

The following equations are the solution to Maxwell's equations in case of a strongly focussed laser beam outside the paraxial approximation as they were used in sect. 2.1.4. They are copied from chpt. 3.6 of ref. 52 and they describe spherical waves with an angular spectrum representation originating from a Gaussian beam that was refracted at a lens and cut by a pupil filter (the back aperture). The electric and magnetic fields are given by:

$$\mathbf{E}(\rho,\varphi,z) = \frac{ikf}{2}\sqrt{\frac{n_1}{n_2}}E_0 e^{-ikf}\begin{bmatrix} I_{00} + I_{02}\cos 2\varphi \\ I_{02}\sin 2\varphi \\ -2iI_{01}\cos\varphi \end{bmatrix}, \tag{B.1}$$

$$\mathbf{H}(\rho,\varphi,z) = \frac{ikf}{2Z_{\mu\varepsilon}}\sqrt{\frac{n_1}{n_2}}E_0 e^{-ikf}\begin{bmatrix} I_{02}\sin 2\varphi \\ I_{00} - I_{02}\cos 2\varphi \\ -2iI_{01}\sin\varphi \end{bmatrix}, \tag{B.2}$$

where k is the wave vector inside the lens, f is the focal length of the lens, n_1 is the refractive index inside the lens, n_2 is the refractive index above the sample, E_0 is the electric field amplitude of the incoming Gaussian laser beam, and (ρ, φ, z) are the spherical coordinates. The integrals I_{0k} are given by:

$$I_{00} = \int_0^{\theta_{max}} f_w(\theta)\sqrt{\cos\theta}\sin\theta(1+\cos\theta)J_0(k\rho\sin\theta)e^{ikz\cos\theta}d\theta,$$

$$I_{01} = \int_0^{\theta_{max}} f_w(\theta)\sqrt{\cos\theta}\sin^2\theta J_1(k\rho\sin\theta)e^{ikz\cos\theta}d\theta,$$

$$I_{02} = \int_0^{\theta_{max}} f_w(\theta)\sqrt{\cos\theta}\sin\theta(1-\cos\theta)J_2(k\rho\sin\theta)e^{ikz\cos\theta}d\theta,$$

where θ is the angle of the k vector with the optical axis, and θ_{max} is the maximum angle, defined by the numerical aperture: $NA = n_1 \cdot \sin\theta_{max}$. $J_\nu(z)$ are Bessel functions of the first kind. $f_w(\theta)$ is the apodization function, defined by:

$$f_w(\theta) = \exp\left(-\frac{1}{f_0^2}\frac{\sin^2\theta}{\sin^2\theta_{max}}\right), \quad f_0 = \frac{w_0}{f\sin\theta_{max}}.$$

f_0 is the filling factor, defined by the amount of laser light filling the back aperture (pupil) of the objective lens, typically $f_0 \geq 1$.

B.2 Reflection of a focussed spot

If a strongly focussed laser beam is reflected at an interface, the effect of depolarization together with the different Fresnel reflection coefficients for parallel and perpendicular polarization leads to strongly position dependent reflection patterns if the numerical aperture is larger than 1. The electric field for that situation as used in sect. 2.1.4 is given in chpt. 3.10 of ref. 52:

$$\mathbf{E}(\rho,\varphi,z) = E_0\frac{k_0 f^2}{2if'}e^{-ik_0(z+f')}\left[(I_{0r} + I_{2r}\cos 2\varphi)\ \mathbf{n}_x - I_{2r}\sin 2\varphi\ \mathbf{n}_y\right]. \tag{B.3}$$

$\mathbf{n}_x$ and $\mathbf{n}_y$ are the carthesian unit vectors, k_0 is the wave vector in air, f' is the focal length of the refocussing lens and z is the defocus of the refocussing lens ($z = 0$ is focussed). All other quantities are identical to the previous section. The integrals I_{0r} and I_{2r} are given by:

$$\begin{aligned} I_{0r}(\rho,z) = &\int_0^{\theta_{max}} f_w(\theta)\cos\theta\sin\theta\left[r_p(\theta) - r_s(\theta)\right] J_0\left(k_0\rho\sin\theta\frac{f}{f'}\right) \\ &\times \exp\left[\frac{i}{2}k_0 z\left(\frac{f}{f'}\right)^2\sin^2\theta + 2ikz_0\cos\theta\right] d\theta, \end{aligned} \tag{B.4}$$

$$\begin{aligned} I_{2r}(\rho,z) = &\int_0^{\theta_{max}} f_w(\theta)\cos\theta\sin\theta\left[r_p(\theta) + r_s(\theta)\right] J_2\left(k_0\rho\sin\theta\frac{f}{f'}\right) \\ &\times \exp\left[\frac{i}{2}k_0 z\left(\frac{f}{f'}\right)^2\sin^2\theta + 2ikz_0\cos\theta\right] d\theta, \end{aligned} \tag{B.5}$$

where r_s and r_p are the Fresnel reflection coefficients and z_0 is the defocus of the objective lens ($z_0 = 0$ is focussed).

B.3 On the amplitude mask for two-pulse correlation experiments

A sinusoidal amplitude mask divides a laser pulse into two identical copies. Thereby, the temporal delay τ as well as the carrier envelope phase difference between the two pulses $\Delta\varphi_{CEP}$ can be chosen. Two-pulse correlation experiments are a key measurement method in this thesis and have been used in chpts. 2, 3, and 4. The situation is visualized in fig. B.1. The electric field of a laser pulse in the time domain can be calculated as the

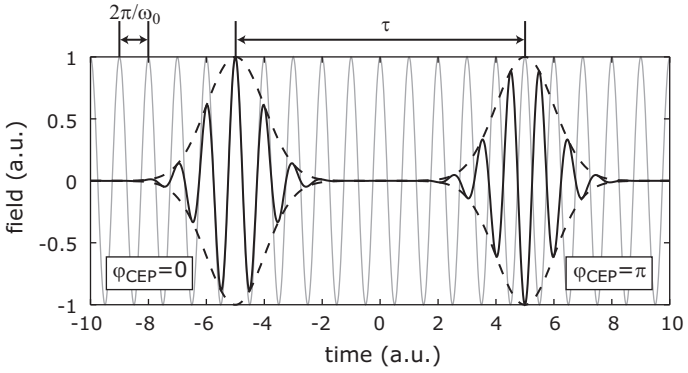

Figure B.1: Visualization of the carrier envelope phase (CEP). There is a CEP difference of $\Delta\varphi_{CEP} = \pi$ between the two pulses. If a pulse correlation scan keeps the CEP fixed, the envelope of the field is shifted in time (dashed line), while if the CEP is not fixed, the entire pulse is shifted.

Fourier transform of the frequency domain:

$$E(t) = \frac{1}{\sqrt{2\pi}} \int_{-\infty}^{\infty} E(\omega) \cdot M(\omega) \cdot e^{-i\omega t}\, d\omega,$$

where $M(\omega)$ is an amplitude mask, imposed by a pulse shaper. By using the mask:

$$M(\omega, \tau) = \cos\left(\frac{\tau}{2}(\omega - \omega_0) - \frac{\Delta\varphi_{CEP}}{2}\right),$$

and with the relation

$$\cos(x) = \frac{1}{2}\left(e^{ix} + e^{-ix}\right), \tag{B.6}$$

the time domain electric field for a two-pulse correlation (TPC) is expressed as:

$$\begin{aligned} E_{TPC}(t, \tau) = \frac{1}{2\sqrt{2\pi}} \int_{-\infty}^{\infty} \big(& E(\omega) \cdot e^{-i\tau\omega_0/2} \cdot e^{-i\Delta\varphi_{CEP}/2} \cdot e^{i(\tau/2 - t)\omega} \\ & + E(\omega) \cdot e^{i\tau\omega_0/2} \cdot e^{i\Delta\varphi_{CEP}/2} \cdot e^{-i(\tau/2 + t)\omega} \big)\, d\omega. \end{aligned} \tag{B.7}$$

Therefore, the pulse is split into two copies that only differ by their temporal position and their carrier envelope phase:

$$E_{TPC}(t,\tau) = E\left(t-\frac{\tau}{2}\right)\cdot e^{-i\tau\omega_0/2}\cdot e^{-i\Delta\varphi_{CEP}/2} + E\left(t+\frac{\tau}{2}\right)\cdot e^{i\tau\omega_0/2}\cdot e^{i\Delta\varphi_{CEP}/2}. \quad \text{(B.8)}$$

Here, the term $e^{\pm i\tau\omega_0/2}$ guarantees that the two-pulse correlation experiment is carried out with a shared carrier envelope phase (as in an intensity autocorrelation scan) and the term $e^{\pm i\Delta\varphi_{CEP}/2}$ determines the carrier phase difference of $\Delta\varphi_{CEP}$. A simpler amplitude mask can be used in order to perform interferometric pulse correlation scans:

$$M(\omega,\tau) = \cos\left(\frac{\tau\omega}{2}\right). \quad \text{(B.9)}$$

In this case, the entire pulse is translated and no shared CEP exists.

B.4 The two-temperature model for graphene

The following equations represent the two-temperature model(TTM) for graphene in combination with the four-wave mixing parts as it was used in sect. 3.3.3. Since the sum of the TTM and FWM depends on physical constants, all units used are stated here, too. As described in the main text, the emission spectrum of graphene is modelled using a constant third-order non-linear constant $\chi^{(3)}$ (in units of $\mathrm{m}^2/\mathrm{V}^2$) for the four-wave mixing (FWM) contribution [74, 75, 77] and the two temperature model for the non-linear photoluminescence (NLPL) [26]. As for the four-wave mixing, it has to be noted that the electric field amplitude $E(\omega)$ is measured in frequency domain units of V/m/Hz. The TTM which is used is almost identical to the model presented by Lui et al. [26]. It is based on the following two coupled ordinary differential equations:

$$\begin{aligned}\frac{dT_{el}(t)}{dt} &= \frac{I_{laser}(t)-\Gamma(T_{el},T_{op})}{c_{el}(T_{el})},\\ \frac{dT_{op}(t)}{dt} &= \frac{\Gamma(T_{el},T_{op})}{c_{op}(T_{op})} - \frac{T_{op}(t)-T_0}{\tau_{op}}.\end{aligned} \quad \text{(B.10)}$$

They describe the temporal evolution of the electronic temperature T_{el} and the temperature of strongly coupled optical phonons (SCOP) T_{op}. The absorbed, time dependent laser irradiance is $I_{laser}(t)$ and given by the incoming laser pulse profile and the fluence F. c_{el} and c_{op} are the specific heat capacities of the electrons and optical phonons, which both depend on the respective temperatures. τ_{op} is the decay time of the SCOPs which couple to a bath of other phonons. We used $\tau_{op} = 1.5\,\mathrm{ps}$ which is the same value used by Lui et al. [26]. Γ is the electron-SCOP energy exchange rate and depends on both temperatures (see below). The specific heat of the electrons per unit area comes from the linear band structure of graphene:

$$c_{el}(T_{el}) = \frac{18\cdot\zeta(3)}{\pi\cdot(\hbar v_F)^2}\cdot k_B^3\cdot T_{el}^2,$$

where $\zeta(3) = 1.202$ is the zeta function, $v_F = 1.1\,\mathrm{nm/fs}$ is the Fermi velocity of electrons in graphene, and k_B is Boltzman's constant. The phonon heat capacity of SCOPs in graphene at 200 meV in the range of $500\,\mathrm{K} < T_{op} < 2500\,\mathrm{K}$ can be estimated by the following heurisitic relation [26]:

$$c_{op} = -4.79 \times 10^9 + 1.82 \times 10^7 \times T_{op} + 1.34 \times 10^4 \times T_{op}^2 + 5.16 \times T_{op}^3$$

as given in $\mathrm{eV/cm^2/K}$. The exchange rate of electrons and SCOPs near the K-point is given by the following expression [26]:

$$\begin{aligned}\Gamma(T_{el}, T_{op}) = \\ \beta \cdot \Big(\big(1 + n(T_{op})\big) \int D(\varepsilon) \cdot D(\varepsilon - \hbar\Omega) \cdot f(\varepsilon, T_{el}) \cdot \big(1 - f(\varepsilon - \hbar\Omega, T_{el})\big) d\varepsilon \\ - n(T_{op}) \int D(\varepsilon) \cdot D(\varepsilon + \hbar\Omega) \cdot f(\varepsilon, T_{el}) \cdot \big(1 - f(\varepsilon + \hbar\Omega, T_{el})\big) d\varepsilon \Big).\end{aligned}$$

The value β (given in $\mathrm{eV^2cm^2/s}$) is an initially unknown scaling parameter that quantifies the overall SCOP-electron coupling strength and is one of the fitting parameters. $\hbar\Omega = 200\,\mathrm{meV}$ is the energy of the SCOPs which is the amount of energy lost in every scattering event. The first term of the equation describes the emission and the second the absorption of a phonon. The density of states of electrons in graphene is given by:

$$D(\varepsilon) = \begin{cases} \frac{2|\varepsilon|}{\pi\hbar^2 v_F^2} & \text{for } \varepsilon > 0, \\ 0 & \text{otherwise.} \end{cases}$$

The population of SCOPs at a temperature T_{op} is defined by the Bose-Einstein distribution $n(T_{op})$, and the population of electrons is given by the Fermi-Dirac distribution $f(\varepsilon, T_{el})$, including the chemical potential of the electrons μ:

$$\begin{aligned} n(T_{op}) &= \big[\exp\big(\hbar\Omega / kT_{op}\big) - 1\big]^{-1}, \\ f(\varepsilon, T_{el}) &= \big[\exp\big((\varepsilon - \mu)/kT_{el}\big) + 1\big]^{-1}. \end{aligned}$$

The solution of eq. B.10 yields the time dependent electronic and phononic temperatures. The assumption is that the observed photoluminescence can be described by black body radiation of the hot electrons. The associated radiative losses, on the other hand, are so small that they do not need to be considered as decay channel in the TTM. The NLPL is then given by [26]:

$$I_{NLPL}(\omega) = \hbar \cdot \frac{\omega^3}{2\pi^2 c^2} \int \Big[\exp\Big(\frac{\hbar\omega}{kT_{el}(t)}\Big) - 1\Big]^{-1} \, dt,$$

and the total emitted spectrum is the sum of FWM and NLPL:

$$I_{em}(\omega) = \eta_{FWM} \cdot I_{FWM}(\omega) + I_{NLPL}(\omega), \tag{B.11}$$

parameter	value
μ	$-0.18\,\mathrm{eV}$
β	$0.5449\,\mathrm{eV^2nm^2/fs}$
η_{FWM}	4.02×10^4
F	$1.07\,\mathrm{eV/nm^2}$

Table B.1: Fit paramters for the two temperature model of graphene.

with the dimensionless FWM emission efficiency η_{FWM}. Although the magnitude of $\chi^{(3)}$ has been measured (sect. 3.2) it is set to unity here. The theoretical autocorrelation scans from fig. 3.13 were calculated on basis of eqns. B.10,B.11 and with the corresponding temporal shape of $I_{laser}(t)$. The parameters μ, β, η_{FWM}, and F had to be fitted to the data, resulting in the numbers given in tab. B.1.

Bibliography

[1] U. Dürig, D. W. Pohl, and F. Rohner, "Nearfield optical scanning microscopy," *Journal of Applied Physics*, vol. 59, no. 10, pp. 3318–3327, 1986.

[2] E. Betzig and J. K. Trautman, "Near-field optics: Microscopy, spectroscopy, and surface modification beyond the diffraction limit," *Science*, vol. 257, no. 5067, pp. 189–195, 1992.

[3] A. M. Weiner, D. E. Leaird, J. S. Patel, and J. R. Wullert, "Programmable femtosecond pulse shaping by use of a multielement liquid-crystal phase modulator," *Optics Letters*, vol. 15, no. 6, pp. 326–328, 1990.

[4] M. M. Wefers and K. A. Nelson, "Generation of high-fidelity programmable ultrafast optical waveforms," *Optics Letters*, vol. 20, no. 9, 1995.

[5] T. Baumert, T. Brixner, V. Seyfried, M. Strehle, and G. Gerber, "Femtosecond pulse shaping by an evolutionary algorithm with feedback," *Applied Physics B*, vol. 65, no. 6, pp. 779–782, 1997.

[6] V. V. Lozovoy, I. Pastirk, and M. Dantus, "Multiphoton intrapulse interference. (iv). ultrashort laserpulse spectral phase characterization and compensation," *Optics Letters*, vol. 29, no. 7, pp. 775–777, 2004.

[7] A. Assion, T. Baumert, M. Bergt, T. Brixner, B. Kiefer, V. Seyfried, M. Strehle, and G. Gerber, "Control of Chemical Reactions by Feedback-Optimized Phase-Shaped Femtosecond Laser Pulses," *Science*, vol. 282, no. 5390, 1998.

[8] V. V. Lozovoy, T. C. Gunaratne, J. C. Shane, and M. Dantus, "Control of Molecular Fragmentation Using Binary Phase-Shaped Femtosecond Laser Pulses," *a European journal of chemical physics and physical chemistry*, vol. 7, no. 12, 2006.

[9] H. Petek, "Single-Molecule Femtochemistry: Molecular Imaging at the Space-Time Limit," *ACS Nano*, vol. 8, no. 1, 2014.

[10] M. Pawłowska, S. Goetz, C. Dreher, M. Wurdack, E. Krauss, G. Razinskas, P. Geisler, B. Hecht, and T. Brixner, "Shaping and spatiotemporal characterization of sub-10-fs pulses focused by a high-NA objective," *Optics Express*, vol. 22, no. 25, p. 31496, 2014.

[11] A. Comin, R. Ciesielski, G. Piredda, K. Donkers, and A. Hartschuh, "Compression of ultrashort laser pulses via gated multiphoton intrapulse interference phase scans," *Journal of the Optical Society of America B*, vol. 31, no. 5, p. 1118, 2014.

[12] A. Comin, R. Ciesielski, N. Coca-López, and A. Hartschuh, "Phase retrieval of ultrashort laser pulses using a MIIPS algorithm," *Optics Express*, vol. 24, no. 3, p. 2505, 2016.

[13] S. Berweger, J. M. Atkin, X. G. Xu, R. L. Olmon, and M. B. Raschke, "Femtosecond nanofocusing with full optical waveform control," *Nano Letters*, vol. 11, no. 10, pp. 4309–4313, 2011.

[14] B. Piglosiewicz, S. Schmidt, D. J. Park, J. Vogelsang, P. Groß, C. Manzoni, P. Farinello, G. Cerullo, and C. Lienau, "Carrier-envelope phase effects on the strong-field photoemission of electrons from metallic nanostructures," *Nature Photonics*, vol. 8, no. 1, pp. 37–42, 2014.

[15] V. Kravtsov, R. Ulbricht, J. M. Atkin, and M. B. Raschke, "Plasmonic nanofocused four-wave mixing for femtosecond near-field imaging," *Nature Nanotechnology*, vol. advance online publication, 2016.

[16] M. Aeschlimann, M. Bauer, D. Bayer, T. Brixner, S. Cunovic, Alexander Fischer, P. Melchior, W. Pfeiffer, M. Rohmer, C. Schneider, C. Strüber, Philip Tuchscherer, and D. V. Voronine, "Optimal open-loop near-field control of plasmonic nanostructures," *New Journal of Physics*, vol. 14, no. 3, p. 033030, 2012.

[17] N. Accanto, L. Piatkowski, J. Renger, and N. F. van Hulst, "Capturing the optical phase response of nanoantennas by coherent second-harmonic microscopy," *Nano Letters*, vol. 14, no. 7, pp. 4078–4082, 2014.

[18] N. Accanto, J. B. Nieder, L. Piatkowski, M. Castro-Lopez, F. Pastorelli, D. Brinks, and N. F. van Hulst, "Phase control of femtosecond pulses on the nanoscale using second harmonic nanoparticles," *Light: Science & Applications*, vol. 3, no. 1, p. e143, 2014.

[19] N. Accanto, L. Piatkowski, I. M. Hancu, J. Renger, and N. F. v. Hulst, "Resonant plasmonic nanoparticles for multicolor second harmonic imaging," *Applied Physics Letters*, vol. 108, no. 8, p. 083115, 2016.

[20] R. Mittal, R. Glenn, I. Saytashev, V. V. Lozovoy, and M. Dantus, "Femtosecond nanoplasmonic dephasing of individual silver nanoparticles and small clusters," *The Journal of Physical Chemistry Letters*, vol. 6, no. 9, pp. 1638–1644, 2016.

[21] D. Brinks, R. Hildner, E. M. H. P. van Dijk, F. D. Stefani, J. B. Nieder, J. Hernando, and N. F. van Hulst, "Ultrafast dynamics of single molecules," *Chemical Society Reviews*, vol. 43, no. 8, p. 2476, 2014.

[22] A. K. Geim and K. S. Novoselov, "The rise of graphene," *Nature Materials*, vol. 6, no. 3, pp. 183–191, 2007.

[23] F. Bonaccorso, Z. Sun, T. Hasan, and A. C. Ferrari, "Graphene photonics and optoelectronics," *Nature Photonics*, vol. 4, p. 611, 2010.

[24] A. C. Ferrari, J. C. Meyer, V. Scardaci, C. Casiraghi, M. Lazzeri, F. Mauri, S. Piscanec, D. Jiang, K. S. Novoselov, S. Roth, and A. K. Geim, "Raman spectrum of graphene and graphene layers," *Physical Review Letters*, vol. 97, no. 18, p. 187401, 2006.

[25] C. Casiraghi, A. Hartschuh, E. Lidorikis, H. Qian, H. Harutyunyan, T. Gokus, K. S. Novoselov, and A. C. Ferrari, "Rayleigh imaging of graphene and graphene layers," *Nano Letters*, vol. 7, no. 9, pp. 2711–2717, 2007.

[26] C. H. Lui, K. F. Mak, J. Shan, and T. F. Heinz, "Ultrafast photoluminescence from graphene," *Physical Review Letters*, vol. 105, no. 12, p. 127404, 2010.

[27] R. J. Stöhr, R. Kolesov, J. Pflaum, and J. Wrachtrup, "Fluorescence of laser-created electron-hole plasma in graphene," *Physical Review B*, vol. 82, no. 12, p. 121408, 2010.

[28] M. Breusing, S. Kuehn, T. Winzer, E. Malic, F. Milde, N. Severin, J. P. Rabe, C. Ropers, A. Knorr, and T. Elsaesser, "Ultrafast nonequilibrium carrier dynamics in a single graphene layer," *Physical Review B*, vol. 83, p. 153410, 2011.

[29] D. Brida, A. Tomadin, C. Manzoni, A. Kim, Y. J. andLombardo, S. Milana, R. R. Nair, K. S. Novoselov, A. C. Ferrari, G. Cerullo, and M. Polini, "Ultrafast collinear scattering and carrier multiplication in graphene," *Nature Communications*, vol. 4, p. 1, 2013.

[30] F. Xia, T. Mueller, Y.-M. Lin, A. Valdes-Garcia, and P. Avouris, "Ultrafast graphene photodetector," *Nature Nanotechnology*, vol. 4, pp. 839–843, 2009.

[31] L. Vicarelli, M. S. Vitiello, D. Coquillat, A. Lombardo, A. C. Ferrari, W. Knap, M. Polini, V. Pellegrini, and A. Tredicucci, "Graphene field-effect transistors as room-temperature terahertz detectors," *Nature Materials*, vol. 11, p. 865, 2012.

[32] F. H. L. Koppens, T. Mueller, P. Avouris, A. C. Ferrari, M. S. Vitiello, and M. Polini, "Photodetectors based on graphene, other two-dimensional materials and hybrid systems," *Nature Nanotechnology*, vol. 9, no. 10, pp. 780–793, 2014.

[33] A. C. Ferrari, F. Bonaccorso, V. Fal'ko, K. S. Novoselov, S. Roche, P. Bøggild, S. Borini, F. H. L. Koppens, V. Palermo, N. Pugno, J. A. Garrido, R. Sordan, A. Bianco, L. Ballerini, M. Prato, E. Lidorikis, J. Kivioja, C. Marinelli, T. Ryhänen, A. Morpurgo, J. N. Coleman, V. Nicolosi, L. Colombo, A. Fert, M. Garcia-Hernandez,

A. Bachtold, G. F. Schneider, F. Guinea, C. Dekker, M. Barbone, Z. Sun, C. Galiotis, A. N. Grigorenko, G. Konstantatos, A. Kis, M. Katsnelson, L. Vandersypen, A. Loiseau, V. Morandi, D. Neumaier, E. Treossi, V. Pellegrini, M. Polini, A. Tredicucci, G. M. Williams, B. H. Hong, J.-H. Ahn, J. M. Kim, H. Zirath, B. J. v. Wees, H. v. d. Zant, L. Occhipinti, A. D. Matteo, I. A. Kinloch, T. Seyller, E. Quesnel, X. Feng, K. Teo, N. Rupesinghe, P. Hakonen, S. R. T. Neil, Q. Tannock, T. Löfwander, and J. Kinaret, "Science and technology roadmap for graphene, related two-dimensional crystals, and hybrid systems," *Nanoscale*, vol. 7, no. 11, pp. 4598–4810, 2015.

[34] A. Jorio, G. Dresselhaus, and M. S. Dresselhaus, eds., *Carbon Nanotubes*, vol. 111 of *Topics in Applied Physics*. Springer Berlin Heidelberg, 2008.

[35] J. W. Mintmire and C. T. White, "Universal density of states for carbon nanotubes," *Physical Review Letters*, vol. 81, no. 12, pp. 2506–2509, 1998.

[36] F. Wang, G. Dukovic, L. E. Brus, and T. F. Heinz, "The optical resonances in carbon nanotubes arise from excitons," *Science*, vol. 308, pp. 838–841, 2005.

[37] X. Ma, N. F. Hartmann, J. K. S. Baldwin, S. K. Doorn, and H. Htoon, "Room-temperature single-photon generation from solitary dopants of carbon nanotubes," *Nature Nanotechnology*, vol. 10, pp. 671–675, 2015.

[38] A. Weiner, *Ultrafast Optics*. John Wiley & Sons, 2009.

[39] C. F. Bohren and D. R. Huffman, *Absorption and scattering of light by small particles*. John Wiley & Sons, 1998.

[40] "Metal-nanoparticle plasmonics," *Laser & Photonics Reviews*, vol. 2, no. 3.

[41] M. I. Stockman, "Nanoplasmonics: past, present, and glimpse into future," *Optics Express*, vol. 19, no. 22, pp. 22029–22106, 2011.

[42] W. T. Silfvast, *Laser fundamentals*. Cambridge University Press, 2nd ed., 2004.

[43] P. F. Moulton, "Spectroscopic and laser characteristics of ti:al$_2$o$_3$," *Journal of the Optical Society of America B*, vol. 3, no. 1, pp. 125–133, 1986.

[44] M. Renard, R. Chaux, B. Lavorel, and O. Faucher, "Pulse trains produced by phase-modulation of ultrashort optical pulses: tailoring and characterization," *Optics Express*, vol. 12, no. 3, p. 473, 2004.

[45] J. P. Heritage, R. N. Thurston, W. J. Tomlinson, A. M. Weiner, and R. H. Stolen, "Spectral windowing of frequency-modulated optical pulses in a grating compressor," *Applied Physics Letters*, vol. 47, no. 2, pp. 87–89, 1985.

[46] A. M. Weiner, "Femtosecond pulse shaping using spatial light modulators," *Review of Scientific Instruments*, vol. 71, p. 1929, 2000.

[47] A. Monmayrant, S. Weber, and B. Chatel, "A newcomer's guide to ultrashort pulse shaping and characterization," *Journal of Physics B: Atomic, Molecular and Optical Physics*, vol. 43, no. 10, p. 103001, 2010.

[48] E. G. van Putten, I. M. Vellekoop, and A. P. Mosk, "Spatial amplitude and phase modulation using commercial twisted nematic LCDs," *Applied Optics*, vol. 47, no. 12, pp. 2076–2081, 2008.

[49] V. Arrizón, "Complex modulation with a twisted-nematic liquid-crystal spatial light modulator: double-pixel approach," *Optics Letters*, vol. 28, no. 15, pp. 1359–1361, 2003.

[50] J. Vaughan, T. Feurer, K. Stone, and K. Nelson, "Analysis of replica pulses in femtosecond pulse shaping with pixelated devices," *Optics Express*, vol. 14, no. 3, p. 1314, 2006.

[51] L. Novotny, R. D. Grober, and K. Karrai, "Reflected image of a strongly focused spot," *Optics Letters*, vol. 26, no. 11, pp. 789–791, 2001.

[52] L. Novotny and B. Hecht, *Principles of Nano-Optics*. Cambridge University Press, 2006.

[53] L. G. Gouy, "Sur une propriete nouvelle des ondes lumineuses," *Comptes Rendus de l'Académie des Sciences*, vol. 110, p. 1251, 1890.

[54] E. H. Linfoot and E. Wolf, "Phase distribution near focus in an aberration-free diffraction image," *Proceedings of the Physical Society. Section B*, vol. 69, no. 8, p. 823, 1956.

[55] F. Lindner, G. G. Paulus, H. Walther, A. Baltuška, E. Goulielmakis, M. Lezius, and F. Krausz, "Gouy phase shift for few-cycle laser pulses," *Physical Review Letters*, vol. 92, no. 11, p. 113001, 2004.

[56] S. Akturk, X. Gu, M. Kimmel, and R. Trebino, "Extremely simple single-prism ultrashort-pulse compressor," *Optics Express*, vol. 14, no. 21, pp. 10101–10108, 2006.

[57] Newport Corporation, "The effect of dispersion on ultrashort pulses." [Online] `http://www.newport.com/The-Effect-of-Dispersion-on-Ultrashort-Pulses/602091/1033/content.aspx` (accessed on 2016-02-01).

[58] V. Chauhan, J. Cohen, P. Vaughan, P. Bowlan, and R. Trebino, "Distortion-free single-prism/grating ultrashort laser pulse compressor," *IEEE Journal of Quantum Electronics*, vol. 46, no. 12, pp. 1726–1731, 2010.

[59] R. Szipőcs and A. Kőházi-Kis, "Theory and design of chirped dielectric laser mirrors," *Applied Physics B*, vol. 65, no. 2, pp. 115–135, 1997.

[60] Thorlabs Incorporation, "Dispersion–compensating mirror set." [Online] `http://www.thorlabs.de/newgrouppage9.cfm?objectgroup_ID=3746` (accessed on 2016-03-02).

[61] R. Trebino, K. W. DeLong, D. N. Fittinghoff, J. N. Sweetser, M. A. Krumbügel, B. A. Richman, and D. J. Kane, "Measuring ultrashort laser pulses in the time-frequency domain using frequency-resolved optical gating," *Review of Scientific Instruments*, vol. 68, no. 9, pp. 3277–3295, 1997.

[62] C. Iaconis and I. A. Walmsley, "Spectral phase interferometry for direct electric-field reconstruction of ultrashort optical pulses," *Optics Letters*, vol. 23, no. 10, p. 792, 1998.

[63] G. S. He, *Nonlinear Optics and Photonics*. Oxford University Press, 2015.

[64] T. Tsang, M. A. Krumbügel, K. W. DeLong, D. N. Fittinghoff, and R. Trebino, "Frequency-resolved optical-gating measurements of ultrashort pulses using surface third-harmonic generation," *Optics Letters*, vol. 21, no. 17, p. 1381, 1996.

[65] R. Selm, G. Krauss, A. Leitenstorfer, and A. Zumbusch, "Non-iterative characterization of few-cycle laser pulses using flat-top gates," *Optics Express*, vol. 20, p. 5955, 2012.

[66] A. M. Turing, "Computing machinery and intelligence," *Mind LIX*, vol. 238, pp. 433–460, 1950.

[67] M. Aeschlimann, M. Bauer, D. Bayer, T. Brixner, F. J. García de Abajo, W. Pfeiffer, M. Rohmer, C. Spindler, and F. Steeb, "Adaptive subwavelength control of nano-optical fields," *Nature*, vol. 446, no. 7133, pp. 301–304, 2007.

[68] T.-w. Wu, J. Tang, B. Hajj, and M. Cui, "Phase resolved interferometric spectral modulation (PRISM) for ultrafast pulse measurement and compression," *Optics Express*, vol. 19, no. 14, pp. 12961–12968, 2011.

[69] V. V. Lozovoy, B. Xu, Y. Coello, and M. Dantus, "Direct measurement of spectral phase for ultrashort laser pulses," *Optics Express*, vol. 16, no. 2, p. 592, 2008.

[70] V. Loriot, G. Gitzinger, and N. Forget, "Self-referenced characterization of femtosecond laser pulses by chirp scan," *Optics Express*, vol. 21, no. 21, pp. 24879–24893, 2013.

[71] M. Miranda, C. L. Arnold, T. Fordell, F. Silva, B. Alonso, R. Weigand, A. L'Huillier, and H. Crespo, "Characterization of broadband few-cycle laser pulses with the d-scan technique," *Optics Express*, vol. 20, no. 17, pp. 18732–18743, 2012.

[72] Z. Sun, T. Hasan, F. Torrisi, G. Popa, D.and Privitera, F. Wang, F. Bonaccorso, D. M. Basko, and A. C. Ferrari, "Graphene mode-locked ultrafast laser," *ACS Nano*, vol. 4, pp. 803–810, 2010.

[73] C. H. Lui, K. F. Mak, J. Shan, and T. F. Heinz, "Ultrafast photoluminescence from graphene," *Physical Review Letters*, vol. 105, no. 12, p. 127404, 2010.

[74] S. A. Mikhailov, "Non-linear electromagnetic response of graphene," *EPL (Europhysics Letters)*, vol. 79, no. 2, p. 27002, 2007.

[75] E. Hendry, P. J. Hale, J. Moger, A. K. Savchenko, and S. A. Mikhailov, "Coherent nonlinear optical response of graphene," *Physical Review Letters*, vol. 105, no. 9, p. 097401, 2010.

[76] R. Wu, Y. Zhang, S. Yan, F. Bian, W. Wang, X. Bai, X. Lu, J. Zhao, and E. Wang, "Purely coherent nonlinear optical response in solution dispersions of graphene sheets," *Nano Letters*, vol. 11, no. 12, pp. 5159–5164, 2011.

[77] R. Ciesielski, A. Comin, M. Handloser, K. Donkers, G. Piredda, A. Lombardo, A. C. Ferrari, and A. Hartschuh, "Graphene near-degenerate four-wave mixing for phase characterization of broadband pulses in ultrafast microscopy," *Nano Letters*, vol. 15, pp. 4968–4972, 2015.

[78] E. Xenogiannopoulou, P. Aloukos, S. Couris, E. Kaminska, A. Piotrowska, and E. Dynowska, "Third-order nonlinear optical properties of thin sputtered gold films," *Optics Communications*, vol. 275, no. 1, pp. 217–222, 2007.

[79] S. A. Mikhailov, "Theory of the nonlinear optical frequency mixing effect in graphene," *Physica E: Low-dimensional Systems and Nanostructures*, vol. 44, no. 6, pp. 924–927, 2012.

[80] S. A. Mikhailov, "Quantum theory of third-harmonic generation in graphene," *Physical Review B*, vol. 90, no. 24, p. 241301, 2014.

[81] S. A. Mikhailov, "Quantum theory of the third-order nonlinear electrodynamic effects in graphene," *Physical Review B*, vol. 93, no. 8, 2016.

[82] R. W. Boyd, *Nonlinear Optics*. Academic Press, 2003.

[83] W. Min, S. Lu, M. Rueckel, G. R. Holtom, and X. S. Xie, "Near-degenerate four-wave-mixing microscopy.," *Nano Letters*, vol. 9, p. 2423, 2009.

[84] R. J. Stöhr, R. Kolesov, J. Pflaum, and J. Wrachtrup, "Fluorescence of laser-created electron-hole plasma in graphene," *Physical Review B*, vol. 82, no. 12, p. 121408, 2010.

[85] T. Winzer, R. Ciesielski, M. Handloser, A. Comin, A. Hartschuh, and E. Malic, "Microscopic view on the ultrafast photoluminescence from photoexcited graphene," *Nano Letters*, vol. 15, no. 2, pp. 1141–1145, 2015.

[86] Mathworks Inc., *Optimization Toolbox*, 2009.

[87] K. G. Petrillo, K.-Y. Wang, A. C. Foster, and M. A. Foster, "Highly sensitive ultrafast pulse characterization using hydrogenated amorphous silicon waveguides," *Optics Express*, vol. 21, no. 25, p. 31229, 2013.

[88] T. Winzer, A. Knorr, and E. Malic, "Carrier multiplication in graphene," *Nano Letters*, vol. 10, no. 12, pp. 4839–4843, 2010.

[89] J. C. Johannsen, S. Ulstrup, F. Cilento, A. Crepaldi, M. Zacchigna, C. Cacho, I. C. E. Turcu, E. Springate, F. Fromm, C. Raidel, T. Seyller, F. Parmigiani, M. Grioni, and P. Hofmann, "Direct view of hot carrier dynamics in graphene," *Physical Review Letters*, vol. 111, no. 2, p. 027403, 2013.

[90] W.-T. Liu, S. W. Wu, P. J. Schuck, M. Salmeron, Y. R. Shen, and F. Wang, "Nonlinear broadband photoluminescence of graphene induced by femtosecond laser irradiation," *Physical Review B*, vol. 82, p. 081408(R), 2010.

[91] E. Malic and A. Knorr, *Graphene and Carbon Nanotubes: Ultrafast Optics and Relaxation Dynamics*. John Wiley & Sons, 2013.

[92] R. Ciesielski, A. Comin, M. Handloser, A. Lombardo, A. C. Ferrari, and A. Hartschuh, "Ultrafast response and carrier dynamics in graphene probed by femtosecond pulse shaping microscopy," *in prep.*, 2016.

[93] L. D'Arsie, S. Esconjauregui, R. Weatherup, Y. Guo, S. Bhardwaj, A. Centeno, A. Zurutuza, C. Cepek, and J. Robertson, "Stability of graphene doping with MoO3 and I2," *Applied Physics Letters*, vol. 105, no. 10, p. 103103, 2014.

[94] N. Mauser and A. Hartschuh, "Tip-enhanced near-field optical microscopy," *Chemical Society Reviews*, vol. 43, no. 4, pp. 1248–1262, 2014.

[95] T. Brixner, F. J. García de Abajo, J. Schneider, C. Spindler, and W. Pfeiffer, "Ultrafast adaptive optical near-field control," *Physical Review B*, vol. 73, no. 12, p. 125437, 2006.

[96] P. B. Johnson and R. W. Christy, "Optical constants of the noble metals," *Physical Review B*, vol. 6, no. 12, p. 4370.

[97] J. Rudnick and E. A. Stern, "Second-harmonic radiation from metal surfaces," *Physical Review B*, vol. 4, no. 12, pp. 4274–4290, 1971.

[98] G. Bachelier, J. Butet, I. Russier-Antoine, C. Jonin, E. Benichou, and P.-F. Brevet, "Origin of optical second-harmonic generation in spherical gold nanoparticles: Local surface and nonlocal bulk contributions," *Physical Review B*, vol. 82, no. 23, p. 235403, 2010.

[99] U. Hohenester and A. Trögler, "MNPBEM – a matlab toolbox for the simulation of plasmonic nanoparticles," *Computer Physics Communications*, vol. 183, no. 2, pp. 370–381, 2012.

[100] C. Rewitz, T. Keitzl, P. Tuchscherer, J.-S. Huang, P. Geisler, G. Razinskas, B. Hecht, and T. Brixner, "Ultrafast Plasmon Propagation in Nanowires Characterized by Far-Field Spectral Interferometry," *Nano Letters*, vol. 12, no. 1, pp. 45–49, 2012.

[101] M. R. Beversluis, A. Bouhelier, and L. Novotny, "Continuum generation from single gold nanostructures through near-field mediated intraband transitions," *Physical Review B*, vol. 68, no. 11, p. 115433, 2003.

[102] H. Wang, T. B. Huff, D. A. Zweifel, W. He, P. S. Low, A. Wei, and J.-X. Cheng, "In vitro and in vivo two-photon luminescence imaging of single gold nanorods," *Proceedings of the National Academy of Sciences of the United States of America*, vol. 102, no. 44, pp. 15752–15756, 2005.

[103] P. Biagioni, M. Celebrano, M. Savoini, G. Grancini, D. Brida, S. Mátéfi-Tempfli, M. Mátéfi-Tempfli, L. Duó, B. Hecht, G. Cerullo, and M. Finazzi, "Dependence of the two-photon photoluminescence yield of gold nanostructures on the laser pulse duration," *Physical Review B*, vol. 80, no. 4, p. 045411, 2009.

[104] V. Knittel, M. P. Fischer, T. de Roo, S. Mecking, A. Leitenstorfer, and D. Brida, "Nonlinear photoluminescence spectrum of single gold nanostructures," *ACS Nano*, vol. 9, no. 1, pp. 894–900, 2015.

[105] W. Min, S. Lu, M. Rueckel, G. R. Holtom, and X. S. Xie, "Near-degenerate four-wave-mixing microscopy," *Nano Letters*, vol. 9, no. 6, pp. 2423–2426, 2009.

[106] Y. Wang, C.-Y. Lin, A. Nikolaenko, V. Raghunathan, and E. O. Potma, "Four-wave mixing microscopy of nanostructures," *Advances in Optics and Photonics*, vol. 3, no. 1, pp. 1–52, 2011.

[107] L. Bonacina, Y. Mugnier, F. Courvoisier, R. L. Dantec, J. Extermann, Y. Lambert, V. Boutou, and J. Galez, C.and Wolf, "Polar $Fe_2(IO_3)_3$ nanocrystals as local probes for nonlinear microscopy.," *Applied Physics B*, vol. 87, p. 399, 2007.

[108] L. Lepetit, G. Chériaux, and M. Joffre, "Linear techniques of phase measurement by femtosecond spectral interferometry for applications in spectroscopy," *Journal of the Optical Society of America B*, vol. 12, no. 12, p. 2467, 1995.

[109] R. Ciesielski, V. Giegold, N. F. Hartmann, E. H. Hároz, H. Budde, A. Comin, S. K. Doorn, and A. Hartschuh, "Electronic and vibrational coherences in single semiconducting carbon nanotubes probed by femtosecond pulse shaping microscopy at room temperature," *in prep.*, 2016.

[110] R. B. Capaz, C. D. Spataru, S. Ismail-Beigi, and S. G. Louie, "Diameter and chirality dependence of exciton properties in carbon nanotubes," *Physical Review B*, vol. 74, p. 121401(R), 2006.

[111] A. Högele, C. Galland, M. Winger, and A. Imamoğlu, "Photon antibunching in the photoluminescence spectra of a single carbon nanotube," *Physical Review Letters*, vol. 100, p. 217401, 2008.

[112] W. Walden-Newman, I. Sarpkaya, and S. Strauf, "Quantum light signatures and nanosecond spectral diffusion from cavity-embedded carbon nanotubes," *Nano Letters*, vol. 12, p. 1934, 2012.

[113] M. S. Hofmann, J. T. Glückert, J. Noé, C. Bourjau, R. Dehmel, and A. Högele, "Bright, long-lived and coherent excitons in carbon nanotube quantum dots," *Nature Nanotechnology*, vol. 8, p. 502, 2013.

[114] S. M. Bachilo, M. S. Strano, C. Kittrell, R. H. Hauge, R. E. Smalley, and R. B. Weisman, "Structure-assigned optical spectra of single-walled carbon nanotubes," *Science*, vol. 298, no. 5602, pp. 2361–2366, 2002.

[115] A. Gambetta, C. Manzoni, E. Menna, M. Meneghetti, G. Cerullo, G. Lanzani, S. Tretiak, A. Piryatinski, A. Saxena, R. L. Martin, and A. R. Bishop, "Real-time observation of nonlinear coherent phonon dynamics in single-walled carbon nanotubes," *Nature Physics*, vol. 2, p. 515, 2006.

[116] Y. S. Lim, K. J. Yee, . H. Kim, E. H. Haroz, J. Shaver, J. Kono, S. K. Doorn, R. H. Hauge, and R. E. Smalley, "Coherent lattice vibrations in single-walled carbon nanotubes," *Nano Letters*, vol. 6, pp. 2696–2700, 2006.

[117] G. D. Sanders, C. J. Stanton, J.-H. Kim, K.-J. Yee, Y.-S. Lim, E. H. Hároz, L. G. Booshehri, J. Kono, and R. Saito, "Resonant coherent phonon spectroscopy of single-walled carbon nanotubes," *Physical Review B*, vol. 79, p. 205434, 2009.

[118] L. Piatkowski, E. Gellings, and N. F. van Hulst, "Broadband single-molecule excitation spectroscopy," *Nature Communications*, vol. 7, p. 10411, 2016.

[119] R. Hildner, D. Brinks, and N. F. van Hulst, "Femtosecond coherence and quantum control of single molecules at room temperature," *Nature Physics*, vol. 7, pp. 172–177, 2010.

[120] D. Brinks, F. D. Stefani, F. Kulzer, R. Hildner, T. H. Taminiau, Y. Avlasevich, K. Müllen, and N. F. van Hulst, "Visualizing and controlling vibrational wave packets of single molecules," *Nature*, vol. 465, no. 7300, pp. 905–908, 2010.

[121] J. Holcman, A. A. Choueiry, A. Enderlin, S. Hameau, T. Barisien, and L. Legrand, "Coherent control of the optical emission in a single organic quantum wire," *Nano Letters*, vol. 11, pp. 4496–4502, 2011.

[122] S. Mukamel, *Principles of Nonlinear Optical Spectroscopy*. New York: Oxford University Press, 1995.

[123] N. F. Hartmann, S. E. Yalcin, L. Adamska, E. H. Hároz, X. Ma, S. Tretiak, H. Htoon, and S. K. Doorn, "Photoluminescence imaging of solitary dopant sites in covalently doped single-wall carbon nanotubes," *Nanoscale*, vol. 7, pp. 20521–20530, 2015.

[124] X. Ma, L. Adamska, H. Yamaguchi, S. E. Yalcin, S. Tretia, S. K. Doorn, and H. Htoon, "Electronic structure and chemical nature of oxygen dopant states in carbon nanotubes," *ACS Nano*, vol. 8, p. 10782, 2014.

[125] Y. Miyauchi, M. Iwamura, S. Mouri, T. Kawazoe, M. Ohtsu, and K. Matsuda, "Brightening of excitons in carbon nanotubes on dimensionality modification," *Nature Photon*, vol. 7, p. 715, 2013.

[126] P. R. Griffiths and J. A. D. Haseth, *Fourier Transform Infrared Spectrometry*. John Wiley & Sons, 2007.

[127] J. J. Crochet, J. G. Duque, J. H. Werner, B. Lounis, L. Cognet, and S. K. Doorn, "Disorder limited exciton transport in colloidal single-wall carbon nanotubes," *Nano Letters*, vol. 12, no. 10, pp. 5091–5096, 2012.

[128] M. W. Graham, Y.-Z. Ma, A. A. Green, M. C. Hersam, and G. R. Fleming, "Pure optical dephasing dynamics in semiconducting single-walled carbon nanotubes," *The Journal of Chemical Physics*, vol. 134, p. 034504, 2011.

[129] I. Eom, S. Park, H.-S. Han, K.-J. Yee, S.-H. Baik, D. Y. Jeong, T. Joo, and Y.-S. Lim, "Coherent electronic and phononic oscillations in single-walled carbon nanotubes," *Nano Letters*, vol. 12, pp. 769–773, 2012.

[130] I. Sarpkaya, Z. Zhang, W. Walden-Newman, X. Wang, J. Hone, C. W. Wong, and S. Strauf, "Prolonged spontaneous emission and dephasing of localized excitons in air-bridged carbon nanotubes," *Nature Commun.*, vol. 4, p. 2152, 2013.

[131] A. Weigel, A. Sebesta, and P. Kukura, "Shaped and feedback-controlled excitation of single molecules in the weak-field limit," *The Journal of Physical Chemistry Letters*, vol. 6, no. 20, pp. 4032–4037, 2015.

[132] J. Mayer, K. Khairy, and J. Howard, "Drawing an elephant with four complex parameters," *American Journal of Physics*, vol. 78, no. 6, pp. 648–649, 2010.

[133] S. V. Goupalov, B. C. Satishkumar, and S. K. Doorn, "Excitation and chirality dependence of the exciton-phonon coupling in carbon nanotubes," *Physical Review B*, vol. 73, p. 115401, 2006.

[134] A. T. N. Kumar, F. Rosca, A. Widom, and P. M. Champion, "Investigations of amplitude and phase excitation profiles in femtosecond coherence spectroscopy," *The Journal of Chemical Physics*, vol. 114, pp. 701–724, 2001.

[135] N. F. Scherer, R. J. Carlson, A. Matro, A. J. Du, M. Ruggiero, V. Romero-Rochin, J. A. Cina, G. R. Fleming, and S. A. Rice, "Fluorescence-detected wave packet interferometry: Time resolved molecular spectroscopy with sequences of femtosecond phase-locked pulses," *The Journal of Chemical Physics*, vol. 95, p. 1487, 1991.

[136] N. Mauser, N. Hartmann, M. S. Hofmann, J. Janik, A. Högele, and A. Hartschuh, "Antenna-enhanced optoelectronic probing of carbon nanotubes," *Nano Letters*, vol. 14, no. 7, pp. 3773–3778, 2014.

[137] K. S. Novoselov, A. K. Geim, S. V. Morozov, D. Jiang, Y. Zhang, S. V. Dubonos, I. V. Grigorieva, and A. A. Firsov, "Electric field effect in atomically thin carbon films," *Science*, vol. 306, no. 5696, pp. 666–669, 2004.

[138] A. C. Ferrari and D. M. Basko, "Raman spectroscopy as a versatile tool for studying the properties of graphene," *Nature Nanotechnology*, vol. 8, no. 4, pp. 235–246, 2013.

[139] A. C. Ferrari, "Raman spectroscopy of graphene and graphite: Disorder, electron-phonon coupling, doping and nonadiabatic effects," *Solid State Communications*, vol. 143, no. 1, pp. 47–57, 2007.

[140] M. Olejnik, A. Agarwal, W. Zaleszczyk, N. A. Kotov, and S. Mackowski, "Gold nanoparticles with elongated shapes: synthesis and optical properties," *Acta Physica Polonica A*, no. 122, pp. 346–349, 2012.

[141] J. A. Fagan, C. Y. Khripin, C. A. Silvera Batista, J. R. Simpson, E. H. Hároz, A. R. Hight Walker, and M. Zheng, "Isolation of specific small diameter single-wall carbon nanotube species via aqueous two-phase extraction," *Advanced Materials*, vol. 26, p. 2800, 2014.

[142] J. A. Fagan, E. H. Hároz, R. Ihly, H. Gui, J. L. Blackburn, J. R. Simpson, S. Lam, A. R. Hight Walker, and M. Doorn, S. K. Zheng, "Isolation of $\geq$ 1 nm diameter single-wall carbon nanotubes species using aqueous two-phase extraction," *ACS Nano*, vol. 9, pp. 5377–5390, 2015.

[143] Y. Piao, B. Meany, L. R. Powell, N. Valley, H. Kwon, G. C. Schatz, and Y. H. Wang, "Brightening of carbon nanotube photoluminescence through the incorporation of sp3 defects," *Nature Chemistry*, vol. 5, p. 840, 2013.

[144] J. G. Duque, C. E. Hamilton, G. Gupta, S. A. Crooker, J. J. Crochet, A. Mohite, H. Htoon, K. A. DeFriend Obrey, A. M. Dattelbaum, and S. K. Doorn, "Fluorescent single-walled carbon nanotube aerogels in surfactant-free environments," *ACS Nano*, vol. 5, no. 8, pp. 6686–6694, 2011.

[145] J. G. Duque, G. Gupta, L. Cognet, B. Lounis, S. K. Doorn, and A. M. Dattelbaum, "New route to fluorescent single-walled carbon nanotube/silica nanocomposites: Balancing fluorescence intensity and environmental sensitivity," *The Journal of Physical Chemistry C*, vol. 115, no. 31, pp. 15147–15153, 2011.

List of Publications

- N. F. Hartmann, D. Piatkowski, R. Ciesielski, S. Mackowski, and A. Hartschuh, "Radiation Channels Close to a Plasmonic Nanowire Visualized by Back Focal Plane Imaging," *ACS Nano*, vol. 7, no. 11., pp. 10257–10262, **2013**.

- A. Comin, R. Ciesielski, G. Piredda, K. Donkers, and A. Hartschuh, "Compression of ultrashort laser pulses via gated multiphoton intrapulse interference phase scans," *J. Opt. Soc. Am. B*, vol. 31, no. 5, p. 1118, **2014**.

- T. Winzer, R. Ciesielski, M. Handloser, A. Comin, A. Hartschuh, and E. Malic, "Microscopic view on the ultrafast photoluminescence from photoexcited graphene," *Nano Letters*, vol. 15, no. 2, pp. 1141–1145, **2015**.

- R. Ciesielski, A. Comin, M. Handloser, K. Donkers, G. Piredda, A. Lombardo, A. C. Ferrari, and A. Hartschuh, "Graphene near-degenerate four-wave mixing for phase characterization of broadband pulses in ultrafast microscopy," *Nano Letters*, vol. 15, pp. 4968–4972, **2015**.

- H. Budde, N. Coca-López, X. Shi, R. Ciesielski, A. Lombardo, D. Yoon, A. C. Ferrari, and A. Hartschuh, "Raman Radiation Patterns of Graphene," *ACS Nano*, vol. 10, no. 2, pp. 1756–1763, **2016**.

- A. Comin, R. Ciesielski, N. Coca-López, and A. Hartschuh, "Phase retrieval of ultrashort laser pulses using a MIIPS algorithm," *Optics Express*, vol. 24, no. 3, p. 2505, **2016**.

- R. Ciesielski et al., V. Giegold, N. F. Hartmann, E. H. Hároz, H. Budde, A. Comin, S. K. Doorn, and A. Hartschuh, "Electronic and vibrational coherences in single semiconducting carbon nanotubes probed by femtosecond pulse shaping microscopy at room temperature," *in prep.*, **2016**.

- R. Ciesielski, A. Comin, M. Handloser, A. Lombardo, A. C. Ferrari, and A. Hartschuh, "Ultrafast response and carrier dynamics in graphene probed by femtosecond pulse shaping microscopy," *in prep.*, **2016**.

List of Conference Contributions

- CeNS Workshop 2012
  Venice, Italy, September 17–21, 2012
  Poster Presentation: *"Active pulse-shaping as a tool in ultrafast optics"*

- NIM Winter School 2013
  Kirchberg (Tirol), Austria, March 3–9, 2013
  Poster Presentation: *"Experimental investigation of SWCNTs, interacting with propagating surface plasmons on gold"*

- 3rd International Workshop on Ultrafast Nanooptics (UNO-3)
  Bad Dürkheim, Germany, June 16–19, 2013
  Oral presentation: *"Controlling the charge carrier relaxation and photoluminescence in graphene using chirped laser pulses"*

- Workshop on Nanocarbon Optics (WNCO)
  Knottenried, Germany, October 7–10, 2013
  Oral presentation: *"Ultrafast Nonlinear Photoluminescence (NL-PL) measurements on graphene"*

- Frühjahrstagung der Deutschen Physikalischen Gesellschaft
  Dresden, Germany, March 30–April 4, 2014
  Oral presentation: *"Controlling and understanding the non-linear photoluminescence in graphene on a femtosecond time scale"*

- 13th International Conference on Near-Field Optics, Nanophotonics, and Related Techniques (NFO-13)
  Salt Lake City, Utah, USA, August 31–September 4, 2014
  Poster presentation: *"Photoluminescence of nano-carbons probed on a femtosecond timescale"*

- XXIXth International Winterschool on Electronic Properties of Novel Materials (IWEPNM 2015)
  Kirchberg (Tirol), Austria, March 7–14, 2015
  Poster presentation: *"Non-linear luminescence and four-wave mixing from graphene, probed by femtosecond pulse shaping"*

- Frühjahrstagung der Deutschen Physikalischen Gesellschaft
  Berlin, Germany, March 15–29, 2015
  Oral presentation: *"Non-linear luminescence and four-wave mixing from graphene, probed by femtosecond pulse shaping"*

- 6$^{\text{th}}$ Workshop on Nanotube Optics and Nanospectroscopy (WONTON 2015)
  Kloster Banz, Germany, June 1–4, 2015
  Poster presentation: *"Ultrafast luminescence and four-wave mixing from graphene probed by femtosecond pulse shaping"*

- Kolloquium Physikalische Chemie der LMU
  München, Großhadern, Germany, February 3, 2016
  Oral presentation: *"Ultrafast dynamics in single nanostructures, investigated by femtosecond laser pulse shaping microscopy"*

- XXX$^{\text{th}}$ International Winterschool on Electronic Properties of Novel Materials (IWEPNM 2016)
  Kirchberg (Tirol), Austria, February 13–20, 2016
  Poster presentation: *"Probing and Controlling Electronic and Vibrational Coherences in Single Carbon Nanotubes"*

- 7$^{\text{th}}$ International Conference on Metamaterials, Photonic Crystals and Plasmonics (META 2016)
  Malaga, Spain, July 25–28, 2016
  Poster presentation: *"The Spectral Phase and Temporal Shape of Femtosecond Laser Pulses in the Nearfield of Plasmonic Nanostructures"*

Danksagung

In den letzten vier Jahren habe ich viele Dinge gelernt, vor allem aber, wie wertvoll und wichtig Zusammenarbeit und Hilfe von Kollegen, Freunden und Projektpartnern sind. Daher möchte ich mich hier bei allen bedanken, mit denen ich in dieser Zeit in Kontakt war und die auf die eine oder andere Art und Weise Einfluss auf diese Arbeit genommen haben.

Zuerst möchte ich herzlich meinem Betreuer **Achim Hartschuh** dafür danken, dass er mich in seinen Arbeitskreis aufgenommen hat. Von ihm habe ich persönlich und wissenschaftlich sehr viel gelernt, ohne ihn wäre ich jetzt kein Experimentalphysiker. **Markus Lippitz** gilt mein besonderer Dank für die Übernahme des Zweitgutachtens.

I wish to thank **Andrea Ferrari**, **David Piatkowski**, **Steven Doorn** and their teams for all the excellent samples they provided and for the collaboration on projects about exciting new materials.

I am grateful for the time working with **Alberto Comin** and **Giovanni Piredda**. Together we learned so much about femtosecond laser pulses.

Vielen Dank an **Ermin Malic** und **Torben Winzer** für die Einblicke in die Photophysik von Graphen und die interessanten Diskussionen.

Weiterhin gilt mein herzlicher Dank meinen Kollegen und Freunden **Harry**, **Tobia**, **Xian**, **Nico**, **Julia**, **Veit**, **Irene** und **Kathi**, ich habe die Zeit mit euch sehr genossen! Außerdem allen ehemaligen Kollegen, von denen ich sehr viel lernen durfte und die mich in die Arbeitsgruppe eingeführt haben, darunter **Matze**, **Nina**, **Nic** und **Miriam**. Vielen Dank an alle Studenten, mit denen ich zusammenarbeiten durfte, insbesondere **Kevin**, **Alex**, **Markus**, **Christina** und **Andrew**.

Weiterhin haben die Veranstaltungen von CeNS und NIM eine große Bereicherung dargestellt, stellvertretend möchte ich daher **Susanne Hennig** und **Peter Sonntag** danken.

Zu guter Letzt möchte ich meiner Familie für die großartige Unterstützung in den letzten Jahren danken, die mir immer eine wichtige Hilfe gewesen ist und vor allem natürlich: **Anna**.